Atomically resolved dynamics of correlated quantum systems

Dissertation with the aim of achieving a doctoral degree
at the Faculty of Mathematic, Informatics and Natural Sciences
Department of Physics
of Universität Hamburg

submitted by Steffen Rolf-Pissarczyk

2017 in Hamburg

Gutachter/innen der Dissertation:	Prof. Dr. Sebastian Loth
	Prof. Dr. Franz X. Kärtner
Zusammensetzung	Prof. Dr. Daniela Pfankuche
der Prüfungskommission:	Prof. Dr. Roland Wiesendanger
	Prof. Dr. Martin Eckstein
	Prof. Dr. Sebastian Loth
	Prof. Dr. Franz X. Kärtner
Vorsitzende/r	Prof. Dr. Daniela Pfankuche
der Prüfungskommission:	
Datum der Disputation:	30.05.2018
Vorsitzender	Prof. Dr. Wolfgang Hansen
Fach-Promotionsausschusses	
PHYSIK:	
Leiter des Fachbereichs PHYSIK:	Prof. Dr. Michael Potthoff
Dekan der Fakultät MIN:	Prof. Dr. Heinrich Graener

Abstract

In this thesis ultra-fast phenomena are investigated with a scanning tunneling microscope (STM). The real space influence of atomic sized defects on ultra-fast dynamics in correlated systems is one of the great mysteries in experimental research of solid states and is investigated in this thesis using two different approaches.

In the first part an artificially built few atom magnet is investigated whose dynamic properties are slowed down by placing it on a decoupling layer. The dynamic properties have a direct impact on spin-dependent transport and lead to the appearance of negative differential resistance. The effects can be astonishingly well described by a rate equation model which allows a deep insight into the processes occurring.

The dynamics investigated in the first part are in the microsecond to nanosecond regime, as much faster processes cannot be measured by a conventional STM. To break this barrier, in the second part of the thesis the development of a new unconventional STM is presented. By coupling picosecond free-space terahertz (THz) laser pulses into the tunnel junction and inducing ultra-fast voltage pulses this new instrument enables pump-probe experiments with femtosecond time resolution on the atomic scale.

In the last part of the thesis the dynamics of the charge density wave (CDW) system 2H-$NbSe_2$ are investigated with the new THz-STM. A complex dynamic response is thereby observed consisting of a 600 fs decay and oscillating features with THz frequencies. The data can be explained by the excitation of the electronic system by a strong screening current which leads to the launch of collective modes of the CDW system. Further spatial resolved measurements indicate a clear link of the dynamic response with atomic defects.

Zusammenfassung

In dieser Arbeit werden ultra-schnelle Phänomene mit einem Rastertunnelmikroskop (STM) untersucht. Der lokale Einfluss von atomaren Defekten auf ultra-schnelle Phänomene in korrelierten Systemen ist eines der großen Mysterien der experimentellen Erforschung von Festkörpern. Diesem Thema wird sich in Rahmen dieser Arbeit aus zwei unterschiedlichen Richtungen angenähert.

Im ersten Teil wird ein aus wenigen Atomen künstlich gebauter Magnet untersucht, dessen dynamische Eigenschaften durch das Platzieren auf einer Entkopplungsschicht verlangsamt wurden. Die dynamischen Eigenschaften haben einen direkten Einfluss auf die elektrischen Transport Eigenschaften und führen zu einem negativen differentiellen Wiederstand. Die auftretenden Effekte können außergewöhnlich präzise mit einem Model basierend auf einer Raten-Gleichung beschrieben werden, das einen tiefen Einblick in die auftretenden Prozesse erlaubt.

Während die dynamischen Prozesse des ersten Teils sich im Mikrosekunden bis in das Nanosekunden Regime abspielen, lassen sich schnellere Prozesse nicht mehr mit konventionellen STM messen. Um diese Barriere zu durchbrechen, wird im zweiten Teil die Entwicklung eines neuen unkonventionellen STM vorgestellt. Durch die Kopplung von Pikosekunden Freiraum Terahertz Pulsen in den Tunnel Kontakt und dem induzieren von ultra-schnellen Spannungspulsen erlaubt das neue Instrument auf der atomaren Skala stroboskopische Messungen mit einer Zeitauflösung kleiner als Pikosekunden.

Mit dem neuen Instrument wird im letzten Kapitel das Ladungsträgerdichtewellen-(CDW)-system 2H-$NbSe_2$ untersucht. Dabei wird eine dynamische Antwort bestehend aus einem 600 fs Abklingen und Schwingung mit THz Frequenzen beobachtet. Die Messungen können durch eine elektronische Anregung erklärt werden, die durch einen starken Schirmungsstrom hervorgerufen wird, und zur Anregung von kollektiven Moden der

CDW führt. Die Verbindung zwischen der dynamischen Antwort und atomaren Defekten wird in weiteren räumlich aufgelösten Messungen deutlich gezeigt.

Acknowledgements

First and foremost I want to sincerely thank my supervisor Prof. Dr. Sebastian Loth for his support, guidance, expertise, and funding. I have to especially thank him for his trust in my abilities and for encouraging me to explore my ideas. The continuous and honest exchange with him played a key role for my (or better our) success.

Second, I want to thank my co-supervisor Prof. Dr. Martin Eckstein for his support and his continuous kindness to explain fundamental theoretical concepts to an experimentalist like me.

Experimental science is hard to achieve alone and I therefore have to thank all the present and past members of the *Loth* group: Jacob Burgess, Shichao Yan, Deung-Jang Choi, Luigi Malavolti, Max Hänze, Gregory McMurtrie, Mohamad Abdo and Björn Schlie. The group has been an amazing melting pot of ideas, support, and discussions (not only scientifically).

I have to thank Shichao for rescuing the Unisoku once in a while, for his constructive feedback, his open mind and for the recording of the Fe on Cu_2N data. I have to thank Jacob not only for is optics introduction during my first year but also for the support during the Pb-island project. I have to thank Luigi letting me being part of the sensing project and all the discussion we had. Greg and Max thank you for your advices and questions letting me reconsider my conclusions and results. Luigi and Greg were also very important during the writing and the proof-read of my thesis, thank you for your support. Exceptional thanks to Björn for his amazing engineering work, without him the THz-STM would be still just an idea. Last but not least I also have to thank Mohamad for being a great colleague in the THz lab who built the optical THz setup and spent night and day-shifts with me to take the remarkable data shown in this thesis.

Furthermore I like to thanks Prof. Dr. Andreas Heinrich letting me work in his lab at the IBM Research Almaden in California during the summer 2015.

Apart from the scientific environment I have to thank my family and here in particular my brother and my parents for supporting me during the past years, for their understanding when I was stuck in work or when I forgot to call back. Mum, the group appreciated your care packages filled with bakery products a lot. Finally, I would like to thank Janica for being by my side and for her love that strengthens me on my path.

Nach neuen Meeren

Dorthin - will ich; und ich traue
Mir fortan und meinem Griff.
Offen liegt das Meer, ins Blaue
Treibt mein Genueser Schiff.

Alles glänzt mir neu und neuer,
Mittag schläft auf Raum und Zeit -:
Nur dein Auge - ungeheuer
Blickt mich's an, Unendlichkeit!

Friedrich Nietzsche, 1887

Table of Content

Abstract ..... **iii**

Zusammenfassung ..... **v**

Acknowledgements ..... **vii**

Table of Content **9**

Chapter 1 Introduction **13**

Chapter 2 Fundamentals of scanning tunneling microscopy **17**

2.1 Scanning tunneling microscope principle 18

2.2 Current spectroscopy 21

Chapter 3 Non-equilibrium transport through few-atom spin-chains **25**

3.1 Negative differential resistance 26

3.2 The iron trimer and basic concepts 28

3.3 The discovery of NDR 30

3.4 Rate equation and effective spin Hamiltonian 34

3.5 Numerical *I(V)* 38

3.6 Spin states 41

3.7 Two-step excitation process 45

3.8 Tip interaction 48

3.9 NDR conclusion 50

3.10 An atomic-scale magnetic sensor 52

Chapter 4 En route to femtosecond scanning tunneling microscopy **57**

4.1 STM in the time domain 57

4.2 The THz-STM concept 62

4.3 Optical setup for THz-Generation 66

4.3.1 THz-Generation 68

4.3.2 The THz-pulse shape 73

4.3.3 Pulse train generation and modulations 75

4.4 The wedged scanning tunneling microscope 79

4.4.1 The coarse movement motor 82

4.4.2 Sample- and tip-stage 85

4.4.3 STM-Head 87

4.4.4 Final STM 88

4.5 THz coupling 91

4.5.1 The THz signal 94

4.6 Summary 99

Chapter 5 Charge density wave dynamics in 2H-$NbSe_2$ 100

5.1 Basic concepts 101

5.2 About the CDW formation mechanism 103

5.3 CDW modes 106

5.4 CDW topography 108

5.5 Femtosecond pump-probe spectroscopy 111

5.5.1 Junction setpoint dependence 117

5.5.2 Pump amplitude dependence 119

5.6 Interpretation of femtosecond spectroscopy 122

5.6.1 Separation of the static and dynamic contributions 122

5.6.2 Excitation mechanism 126
5.6.3 Nature of the dynamic signal 129
5.6.4 Additional contributions to the dynamic signal 131
5.7 Spatial variation 131
5.7.1 Topography of THz pump-probe signal 131
5.7.2 High quality spectra at two different position 134
5.8 Conclusion 136
Chapter 6 Supplement 138
6.1 Chapter 3 - Fitting routine 138
6.2 Chapter 4 139
6.2.1 Mechanical stability and vibration analysis of THz-STM 139
6.2.2 Cryostat and radiation shields 143
6.2.3 Clamping mechanism for tip and sample exchange 146
6.3 Chapter 5 - Simple Landau model of CDW dynamics 147
References 150
Publication list 170

Chapter 1 Introduction

The properties of electrons in matter fundamentally govern everyday life. In the information age integrated circuits, microchips and other electronic devices have become indispensable. With quantum mechanics these technologies can be understood within the framework of single electrons and by treating the interaction thereof in an effective fashion or on a perturbative level [Ful12]. However, these models break down for complex matter, which exhibits fascinating properties such as superconductivity, charge order or anti-ferromagnetism [And72, Dag05, BAvdM+11]. The interaction between electrons as well as other degrees of freedom plays a crucial role in these systems and cannot be neglected. These dynamics of these effects reach timescales in the femtosecond regime [BAvdM+11, ZA14]. Furthermore, they are inseparably connected to the specific local structure of their environment, perturbed by defects, boundaries and inhomogeneity down to the atomic level. Linking ultra-fast phenomena with local structures and properties will lead to a more fundamental understanding of these systems.

Many different experiments have shown that in complex mater the picosecond time scale is crucial for emergent phenomena and their fluctuations [GCF+16, HRK+12]. Just recently, studies were published which indicate the possibility of inducing superconducting properties well above the static superconducting transition temperature, on the picosecond timescale [FTD+11, MCN+16]. Not only superconductivity, but also other collective phenomena such as charge density waves exhibit collective modes in this time regime [YMK+10, TMB+13]. While the dynamics are typically well investigated on the macroscopic scale, their microscopic connections to specific atomic scale defects are not. Nevertheless, the general significance of spatial inhomogeneity is doubtless and already manifests itself in the static properties of complex systems, such as in phase transitions caused by doping [ZA14], the granular structure of the superconducting gap in BSCCO [LMH+02] or the pinning of charge density waves [ACR+14].

Conventional time resolved experimental methods are spatially averaging probes, and the connection between structure and dynamics, if explored, is conventionally performed using scattering techniques. Those techniques have been successfully used to track the internal motion of molecules [Zew00] or the formation of charge density waves [ESK+10]. Nevertheless these techniques can only investigate reciprocal space, the direct impact of a specific defect is hidden and not reliably accessible. The scanning tunneling microscope (STM), on the other hand, is a local probe with inherent atomic resolution. It is particularly useful for characterizing electronic properties due to its sensitivity at the Fermi energy. From this perspective STM is a well suited tool for the investigation of dynamics on the atomic scale. However, its bandwidth typically limits the observation to timescales slower than the millisecond to microsecond range.

An established approach to making dynamic correlation effects visible to the STM is to slow them down. Coupled spin systems with lifetimes reaching many milliseconds can be constructed by placing single transitions metal atoms on a decoupling layer which suppresses the interaction with the electronic bath [LEL+10, YCB+15a, PYB+17]. Based on this modular principle, different model systems with varied phenomena such as negative differential conductance [RPYM+17], spin waves [SBD+14], antiferromagnetism [LBL+12], Kondo-screening [CRY+17] or the emergence of quantum phenomena [DLZFR15] can be artificially built and investigated. Their dynamics play an important role in the development of molecular spintronic devices, which have the potential to surpass conventional approaches in speed, energy-consumption and functionality. Furthermore, in recent years the coherent control of the spin properties of these objects has attracted more attention from the perspective of quantum computation [BPC+15, CPRP+17]. The reduced speeds of the spin system dynamics combined with measurement advances allowed different STM methods to investigate them with nanosecond resolution. While all-electronic pump-probe spectroscopy allows the direct study of relaxation processes, transport measurements also exhibit indirect information about other dynamic processes of these spin systems [LvBT+10].

These elaborate techniques start to fail if the dynamics cannot be slowed down, as is the case when investigating complex materials with intrinsic timescales on the order of pico-

seconds. For over 25 years scientists have tried to overcome this limit, searching for approaches which allow comprehensive studies that combine STM technology with sophisticated time resolution. The natural route in the past was the combination of STM with ultra-fast laser technology. Among other difficulties, the main drawback of this combination is induced heating due to the laser, which has a severe impact on the performance of the STM [GKP+00]. Despite proof-of-principle experiments, the large technical effort necessary to circumvent these influences usually prohibited the detailed study of complex matter. With the development of terahertz (THz) laser pulse technology in the last decade a new promising idea was born. In contrast to optical pulses, with photon energies on the order of electron volts, THz radiation carries only a few millielectronvolts. This difference results in drastically different coupling schemes for THz-pulses compared to optical pulses. While optical pulses create photo-excited carriers and thereby also induce heat, THz coupling exhibits more similarities to radio waves generating pure AC voltages in ordinary antennas. Free-space THz-pulses coupled into a STM tip will induce ultra-fast voltage pulses, which can be used to pump and probe arbitrarily complex materials down to the femtosecond regime. Although this appears to be a promising avenue, many important aspects have to be considered if the THz-STM idea is to be implemented in a working instrument. Most importantly, THz-pulses have to be generated with a high repetition rate, in order to achieve a sufficient signal-to-noise ratio in a STM measurement. Unfortunately the state-of-the-art effective THz generation schemes have so far relied on low repetition rate systems.

In this thesis a new THz-STM is developed. It has low temperature capabilities (down to 15 K), a high mechanical stability on the picometer scale, and can perform pump-probe experiments with a time resolution of 400 fs at repetition rates of 41 MHz, thereby reaching signal sensitivities of 0.002 electrons per pulse. First results from the instrument are obtained on the charge density wave system 2H-$NbSe_2$. Here, femtosecond electron dynamics and collective charge density wave modes can be resolved. The spatial dependency of the signal indicates that dynamics do indeed change on the nanometer scale and are highly sensitive to atomic defects. This study represents the first investigation of a complex system with femtosecond time and atomic real-space resolution. The high quality of

the data acquired allowed for the identification of the dynamic signal and its separation from other measurement artefacts.

This work begins with a general introduction to STM. Following this, in the second chapter a well understood dynamic system is investigated, using conventional STM. The effect of few atom magnet spin dynamics on electronic transport is investigated on the nanosecond timescale. The interaction of the magnet with its local environment drastically alters its behavior. The transport can be described by a rate equation model which includes the back action on the magnet by the tunneled electrons. This model can reproduce the transport measurement obtained by conventional STM techniques that drive the system far from equilibrium astonishingly well. Then the thesis ventures into unexplored territory. The development and characterization of the THz-STM is presented in the third chapter, followed by the first results obtained with the instrument in the fourth chapter.

Chapter 2 Fundamentals of scanning tunneling microscopy

The scanning tunneling microscope (STM) is the experimental basis of this thesis. Since its invention in 1982 by Binning and Rohrer [BRGW82, BRGW] STM has become a broadly applied technique for the study of condensed matter surfaces. Today, STM's can be found in many varieties, from simple tabletop students-experiments to state-of-the-art research instruments encapsulated in room-filling installations, which achieve environments quieter, colder, and emptier than space. Not only do the instrumentational efforts vary, the kinds of explorations differ as well. In some laboratories measurements are made on one single atom for months while in other facilities the STM is used as a quick surface characterization tool.

Despite its many-fold applications, the basic operational principles are always the same. In this chapter these principles will be briefly introduced. In addition, the standard measurement methods applied in this thesis and their terminology will be presented. For the illustration of these explanations experimental measurements will be used which were performed on nano-sized superconducting islands.

Further information and more detailed descriptions of scanning tunneling microscopy or scanning probe techniques in general can be found in common textbooks [Che08, Voi15].

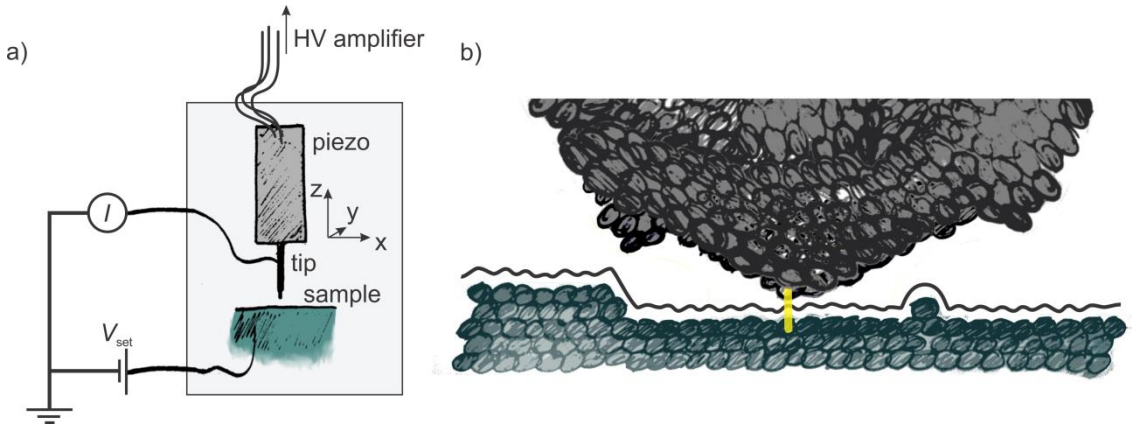

Figure 2.1 (a) A sketch of the fundamental parts of a scanning tunneling microscope. A metallic tip is placed above a conducting sample surface. Tip and sample are electronically contacted. Typically the tip can be positioned using piezoelectric elements. These parts are installed in a low noise environment (surrounding box), which is isolated from vibrations, electromagnetic waves as well as dust, gas, or other particles. A tunnel current can be detected if a small voltage is applied between tip and sample with the tip brought very close to the surface (< 1 nm). (b) Sketch of the STM tunnel junction with a feedback loop controlling the tip-sample distance. The tunnel current (yellow line) is kept constant and the tip can be scanned along a constant current topography (black line).

2.1 Scanning tunneling microscope principle

In condensed matter the fundamental length scale is the distance between two lattice sites of a solid crystal, which is commonly in the range of a few ångstom (1 Å = 10^{-10} m). In order to "see" this distance in an optical microscope the wavelength of the light used needs to be of the same order or less. This greatly exceeds the diffraction limit for visible light. Since even near-field optical instruments cannot yet achieve this resolution, one is effectively optically blind on these length scales. In analogy to a white cane that allows blind people to explore their environment, the scanning tunneling microscope is a fascinating tool for overcoming this blindness to the atomic world.

The "white cane" of the STM is a sharp metallic needle i.e. the STM tip. By almost touching the surface of a conducting material the tip can sense the density of electronic states (DOS) that surround the atom cores. By scanning the tip above the surface a picture of the local density of states (LDOS) can be obtained.

While a white cane has to be tapped to feel the surface, the sensing mechanism in a STM is a small tunnel current. Interestingly, in an atomic force microscope (AFM), a technique complementary to the STM, a tapping-like sensing mechanism is used. The origin of the current in the STM is quantum mechanical tunneling. This effect allows electrons to penetrate classically insurmountable barriers such as the insulating vacuum between tip and surface. This effect leads to a net current between tip and surface if a voltage of the order of 1 V or less is applied between them and if they are less than one nanometer (1 nm) apart. Typically the tunnel currents employed in STM experiments have a magnitude on the order of nanoamperes (1 nA). The current decays exponentially with tip sample distance (Δz),

$$I(z) \propto e^{-2\kappa z} \text{ with } \kappa = \sqrt{\frac{2m\phi}{\hbar}}, \qquad 2.1$$

with barrier height ϕ, electron mass m, and the reduced Planck constant $\hbar$. For a typical metal ϕ is of the order of 4 eV and the current decreases by one order of magnitude when the distance is increased by 1 Å.

The exponential distance dependence of the tunnel current is essential for STM operation and enables precise control of the tip-sample distance. However, perturbations such as vibrations, heat expansion or simply sample height variations that may arise if the tip is moved over the sample surface make continues re-adjusting of the tip-sample distance necessary. This process is typically performed by a feedback loop that controls the tip-sample distance (Δz) such that the measured tunnel current I corresponds to a given current I_{set} at a given bias voltage V_{set}. The pair of current I_{set} and voltage V_{set} is called setpoint, sometimes the setpoint is given equivalently in conductance $\sigma_{set} = I_{set}/V_{set}$ and voltage V_{set}.

The continuous three-dimensional (x,y,z) movement between tip and surface is typically provided by piezo-electric elements. The linear response of these elements allows picometer resolution, which is mostly limited by the quality of the applied voltage. Under normal

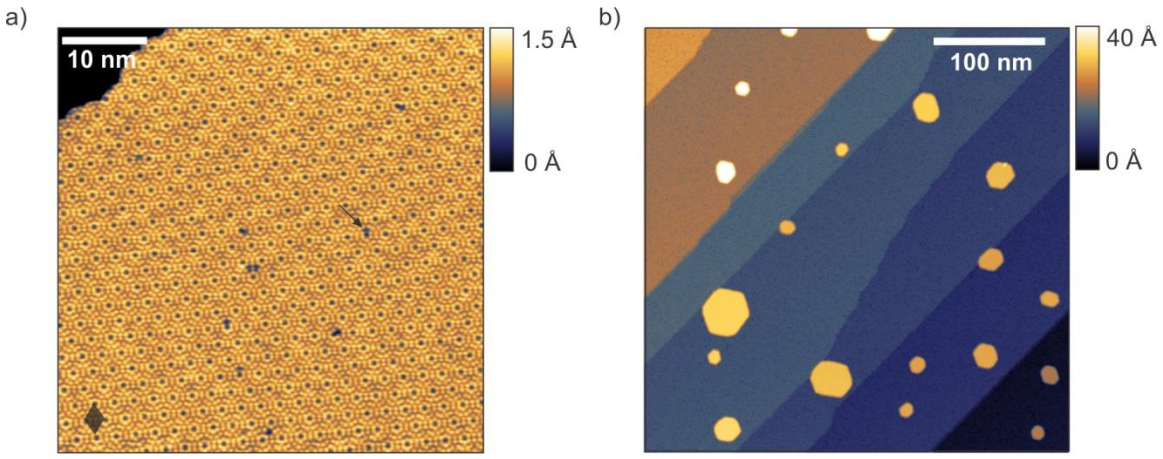

Figure 2.2 Constant current STM topographies recorded in a commercial ultra-high-vacuum (<1 e-11 mbar) and low temperature (0.6 K) STM system. a) Si(111) 7×7 surface with atomic resolution recorded at a tunnel setpoint 160 pA at 2 V. The grey diamond (lower left corner) indicates the unit cell of the 7×7 reconstruction. The black arrow indicates one of the atomic defects visible in this map. b) A larger scale topography of Pb-islands grown on a Si(111) 7×7 recorded at a tunnel setpoint 70 pA at 100 mV.

condition an approximate estimate yields a 1 Å displacement if the voltage changes by 6 mV. The basic setup and working principle is pictured in **Figure 2.1**.

Historically, the main purpose of STM was the imaging of surfaces. Here two different modes exist, constant-height and constant-current mode. In the constant-height mode the z coordinate is kept constant while the tunnel current is recorded as function of the in-plane position *(x,y)*. In constant-current mode the feedback loop is on and the current is kept constant, while the *z*-position, the apparent tip height, is recorded as a function of the in-plane position *(x,y)*. Two STM topographies recorded in constant-current mode are shown in **Figure 2.2**.

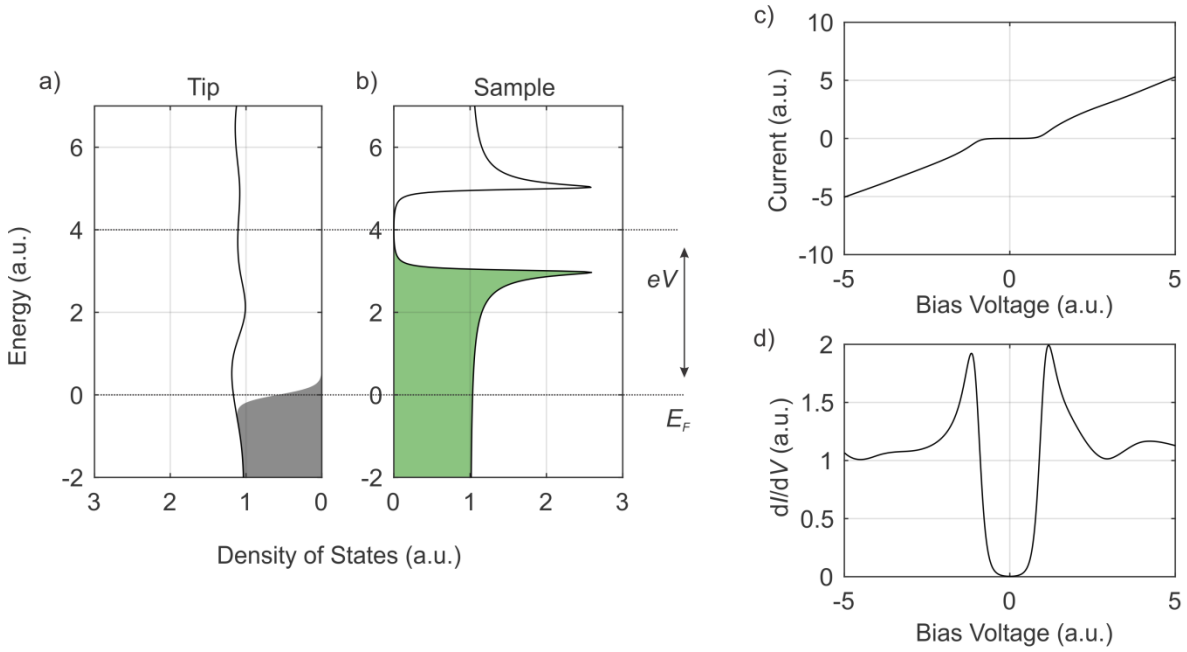

Figure 2.3 Illustration of the origin of the tunnel current. (a-b) Applying a voltage V between tip and sample leads to a relative energy shift of their density of states (DOS). In this example the sample DOS has a gap feature (typical for superconductors) and the tip DOS exhibits some small variations. The states are occupied according to the Fermi distribution (filled areas). b) The resulting tunnel current I (from equation 2.2) with a constant tunnel matrix element (M = const). c) From the current I the numerical derivative dI/dV was calculated. The dI/dV is dominated by the gap feature of the sample DOS. However, compared to the sample DOS the gap is widened due to the finite broadening of the state occupation in the tip. In addition the impact of the non-flat tip DOS is visible.

2.2 Current spectroscopy

Today, the advantage of STM is not simply the possibility of imaging surfaces with atomic resolution but rather the high sensitivity of the tunnel current to electron states near the Fermi energy. These states dictate most of the electronic properties like conductivity or reflectivity of the material surface and are therefore of general interest. The connection between the DOS at the Fermi energy $\rho_S(E_F)$ and the tunnel current becomes clear in a formal description of it.

Although the tunnel current can be treated in various fashions, in most STM textbooks the tunnel current is described in the Bardeen picture in which the tunnel current stems from the finite overlap of the wave functions of the two electrodes (tip and surface). The tunnel rate of electrons is then given by Fermi's golden rule which yields the tunnel current by summing over all possible states considering the Pauli Exclusion Principle [Che08, Voi15]:

$$I = \frac{4\pi\, e}{\hbar}\int_{-\infty}^{+\infty} d\epsilon\, [f(E_F - eV + \epsilon) - f(E_F + \epsilon)] \times\ \rho_S(E_F - eV + \epsilon)\, \rho_T(E_F + \epsilon)\, |M|^2. \qquad 2.2$$

Here e is the electron charge, $f(\epsilon')$ is the Fermi distribution, E_F is the Fermi energy, V is the applied voltage between tip and sample, ρ_S is the density of states (DOS) of the sample, ρ_T is the DOS of the tip and M is the tunneling matrix element. The meaning of this equation is illustrated in **Figure 2.3** where as an example spectroscopy of an electronic gap is used as it appears in the DOS of a superconducting system [BK08].

The equation 2.2 shows that by tuning the applied voltage, the density of states of the sample ρ_S near the Fermi energy can be explored. This exploration is called scanning tunneling spectroscopy (STS). For STS the matrix element M and the density of states of the tip ρ_T are commonly approximated as constant. In this case and for sufficiently low temperatures, the differential conductance dI/dV is directly proportional to the DOS at the Fermi energy $\rho_S(E_F)$:

$$\frac{\mathrm{d}I}{\mathrm{d}V} \propto \rho_S(E_F - eV). \qquad 2.3$$

For this reason, not only the tunnel current but also the differential conductance dI/dV is of great interest. In reality the dI/dV features are smeared out by temperature, featuring a width increase of approximately $\Delta E \propto 4k_BT$ [Che08] (k_B is the Boltzmann constant) that arises from the broadened Fermi distribution. Additionally, the tip DOS ρ_T is often not completely flat, which may further distort dI/dV features. The impact of these effects on the dI/dV and *I(V)* is illustrated in **Figure 2.3**.

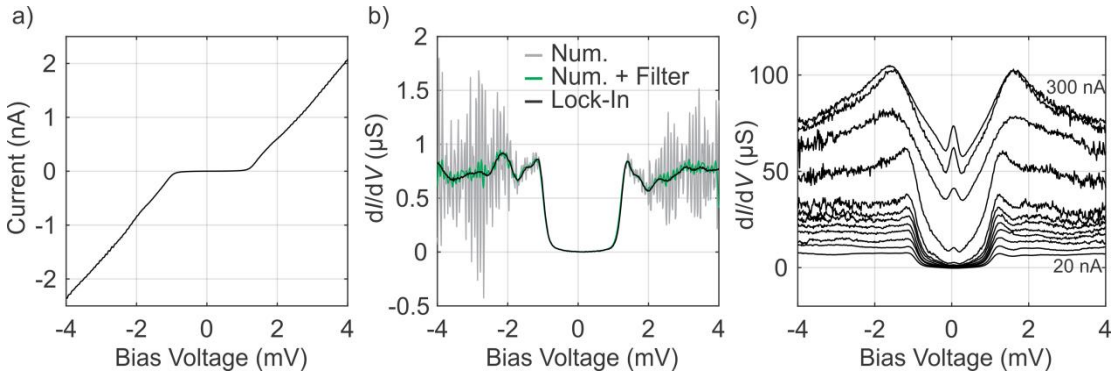

Figure 2.4 a) $I(V)$ spectrum recorded on a superconducting Pb-island at 0.6 K with a tunnel junction setpoint of 2 nA at 4 mV. b) The corresponding differential conductance (dI/dV) spectrum obtained by direct numerical differentiation of the $I(V)$ (grey line), including a Gaussian filter (green line) and obtained from a simultaneously recorded Lock-In signal (black line). For the Lock-In detection an AC modulation voltage of 72 μeV_{rms} at 730.5 Hz was added to the bias voltage line. c) Setpoint current dependent dI/dV spectra ranging from 20 nA to 360 nA at 4 mV.

Whereas in **Figure 2.3** the dI/dV and $I(V)$ were numerical examples, in **Figure 2.4** a) and b) a real measurement is shown. The dI/dV spectrum is recorded on a superconducting Pb-island grown on Si(111) 7x7, see **Figure 2.2**, and is dominated by the aforementioned superconducting gap. For voltages exceeding the superconducting gap width ($|V| > 1.2$ mV), other features -humps and peaks- can be observed.

Practically, the differential conductance is not usually obtained by taking the numerical derivative of the current but rather by direct measurement with a Lock-In amplifier (Lock-In method). In this approach an oscillatory voltage $\Delta v = \Delta v_0 \sin \omega t$ with frequency ω and amplitude Δv_0 is added to the bias voltage. If Δv is sufficiently small the tunnel current can be expressed as:

$$I(V + \Delta v) = I(V) + \frac{\mathrm{d}I}{\mathrm{d}V}\Delta v = I(V) + \frac{\mathrm{d}I}{\mathrm{d}V}\Delta v_0 \sin \omega t. \qquad 2.4$$

A Lock-In amplifier with reference frequency ω is sensitive to the second term of the right hand side and will output a signal proportional to it:

$$LI(V) \propto \frac{\mathrm{d}I}{\mathrm{d}V}\Delta v_0. \qquad 2.5$$

The missing proportionality factor can be determined by various means, for example by numerically integrating the obtained Lock-In signal $LI(V)$ and adjusting it to equal the simultaneously recorded *I(V)*.

Typically the Lock-In method leads to a better Signal-Noise-Ratio in the dI/dV than the simple numerical derivative of the *I(V)*, see **Figure 2.4**b), because a STM generally has a lower spectral noise density (PSD) at larger frequencies. A more detailed explanation of the Lock-In methods and under which circumstances it enhances the Signal-to-Noise ratio can be found in the textbook by B. Voigtländer [Voi15].

It is worth noting, that the gap itself varies only slightly on each island, the other features vary significantly [RPBYL16]. Although these features will not be further investigated in the scope of this thesis, they still highlight the important fact that not all features measured by the dI/dV are directly related to the density of states. In contrast to the superconducting gap, which stems from the density of states, these features most likely originate from phonon excitation by inelastic tunnel processes occurring because of the STM measurement itself [SMJ+15]. Similar inelastic processes caused by spin-excitation will be discussed in the next chapter.

There are further effects which alter the dI/dV which cannot be explained by the one electron density of states. One fascinating example of this is the appearances of a dominant peak at zero bias, when the metallic STM tip is very close to the superconducting substrate, see **Figure 2.4**c), which in literature is attributed to a second-order proximity-induced Josephson effect [ARV92]. Importantly, such setpoint dependent spectra allow the identification of dynamic processes, since for increasing rates of electrons tunneling, correlation effects become correspondingly more important. In other words, if a tunneled electron is causing a 1 ns long dynamic effect, which could be probed by a subsequent second electron, then this effect should have an impact on the transport for tunnel currents larger than $I > {}^{e}/_{1\,\mathrm{ns}} \approx 160\,\mathrm{pA}$. Indeed, the next chapter is not just about spin-excitation but also how such excited dynamics strongly alter transport.

Chapter 3 Non-equilibrium transport through few-atom spin-chains

In this chapter the dynamics of few-atom spin-chains will be discussed, as well as how these dynamics manifest in electronic transport measurements. Here, the few atom spin-chains are artificially built with atom manipulation on a decoupling layer in a scanning tunnel microscope. In this way interacting magnetic atoms can be arranged in complex correlated spin structures which exhibit fascinating new properties.

The chapter will focus in particular on the phenomenon of negative differential resistance (NDR) occurring in spin-dependent transport through an antiferromagnetically coupled spin-chain. Here, electrons tunneling between tip and sample scatter inelastically with the structure and thereby exchange angular momentum and energy. The excitation by inelastic tunnel processes causes dynamics which leads to a non-equilibrium configuration of the spin-chains that is accompanied by a change of magnetoresistance. Beside the dynamic impact of the tunneled electrons the spin-polarized tip also influences the states of the magnetic structure directly via a static magnetic interaction. The dynamics and the reconfiguration can be understood in detail using an effective spin Hamiltonian picture and a rate equation approach. The results of this chapter are pending for publication [RPYM+17].

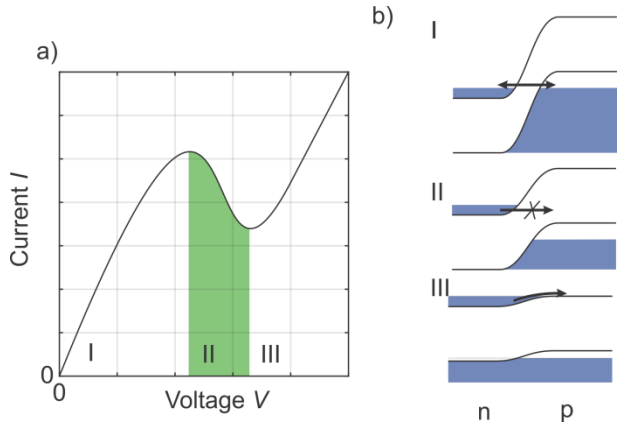

Figure 3.1 (a) Schematic of a *I(V)* curve exhibiting negative differential residence (NDR). (b) The working principle of a tunnel diode is illustrated. For small voltage magnitudes electrons can tunnel through the p-n junction (I). Tunneling becomes suppressed for forward voltages at which electrons have to tunnel into the band gap (II). By increasing the voltage even further the bands flatten out and the current increases again (III).

3.1 Negative differential resistance

Electronic devices are characterized by their *I(V)* curves. Usually, these curves are monotonic and for larger voltages, larger currents flow. Special, non-linear devices can have voltage regions at which the current decreases while the voltage increases. Since in this range the equation $\frac{dV}{dI} < 0$ holds, this phenomenon is called negative differential resistance (NDR), and is shown schematically in Figure 3.1.

NDR is widely used in modern electronic devices and, for example, is an essential part of electronic oscillators [Rid93]. Manifold approaches exist to realize NDR, a prominent example are tunnel diodes [Esa74, Gru06]. Here the non-linearity of the density of states of a p-n-semiconductor junction leads to NDR, as shown in **Figure 3.1**. The p-n-junction is designed such that at low bias voltages electrons can tunnel through the p-n-junction between the valence and conduction bands resulting in a finite current. Applying larger voltages in the forward direction breaks the alignment of the conduction band and the valence band. This suppresses tunneling since electrons would have to tunnel into the band gap, resulting in the appearance of NDR. Only for sufficiently large voltages will the bands start flatten to out, allowing electrons to flow directly through the conduction band,

with a corresponding increase in current. This principle was first explained and demonstrated by Esaki in 1958 [Esa58].

Modern NDR concepts are based on resonant tunneling through sharp electronic states [Esa74, CET74], which are beneficial since they allow stronger NDR and faster operation [SMSG92, SHMS98]. This situation can be achieved in electronic transport through quantum wells and dots, single molecules, single atoms or molecular monolayers [CRRT99, PFK+14, XD15, GLH00, Tao06]. Since the position of the electronic states can be effected by external perturbations these devices can operate as sensors [DMK+01, CHZ+07]. For example, a Zeeman-energy-induced shift of NDR was found in transport through single magnetic molecules [WEHP+15]. Additionally, an electron-spin-dependent NDR occurs in transport geometries including a double quantum dot [OATT02]. In this geometry the interplay of Coulomb interaction and the Pauli exclusion principle can lead to the case in which the occupation of one quantum dot is blocking transport and suppressing the electric current [WHK95, OATT02, PLCL+03]. This mechanism is also known as Pauli-blockade. Although the details of the NDR mechanisms for the different devices differ, they are all based on the alignment of electronic states and their participation in electronic transport.

By contrast, this chapter presents the discovery of a NDR mechanism which does not rely on the position of specific electronic states, but rather on the dynamic equilibrium occupation of spin states of a few-atom spin-chain. Since the presented NDR is purely spin-based, the findings may help the development of new spintronic devices. In spintronic technology the spin degree of freedom is exploited for sensing, data storage or computing applications. One advantage over conventional electronics is that spintronic devices in general exhibit easier manipulation schemes and consume less power. For these reasons, it is of great interest to transfer functionalities such as NDR to a pure spin based footing.

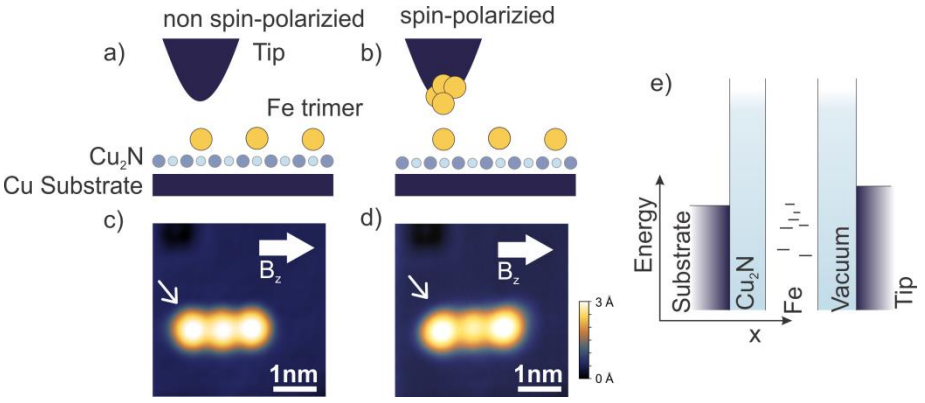

Figure 3.2 (a-b) Schematic of the experimental setup. The STM tip is positioned above a side atom of a Fe trimer built on a Cu2N layer. The measurements are performed without (a) and with (b) a spin-polarized tip. (c-d) Constant current topographies of the Fe trimer with normal metal (c) and with spin-polarized tip (d) (2 nS at 5 mV). (e) The setup can be pictured as a double-barrier geometry in which the Fe trimer is sandwiched between the tip and Cu substrate and decoupled from both electrodes a by tunneling barrier consisting of vacuum on one side and Cu_2N on the other.

3.2 The iron trimer and basic concepts

The spin-based negative differential resistance is found in the *I(V)* curve of a scanning tunneling microscope experiment with the geometry illustrated in **Figure 3.2**a) and b). The investigated system is a chain of three magnetic Fe atoms (Fe-trimer) located on a single layer of copper nitride (Cu_2N). The Cu_2N layer decouples the atoms from the electronic bath of the Cu substrate and thereby perseveres some of their single atom properties. In particular their spin momentum remains unquenched and can be well described in an effective spin Hamiltonian picture [GSV11]. Located in close vicinity to each other, the atoms start to interact and interesting new properties arise. Sample systems based on the coupling of single transition metal atoms such as Fe positioned via atom manipulation on Cu_2N [ES90, SE91] were extensively investigated with STM's. This technique allow the exploration of different artificially built model systems exhibiting fascinating effects such as spin waves [SBD+14], entangled Kondo systems [CRY+17], or stable magnetism [LBL+12].

The measurements presented in this chapter were performed in a commercial Ultra-High Vacuum (UHV) STM (Unisoku USM-1300) instrument at a base temperature of 0.5 K. The instrument is equipped with a vector magnet capable of applying 2 T in any space direction. The Cu_2N decoupling layer is grown on a single Cu(100) crystal which was cleaned beforehand by several cycles of Ar-sputtering and annealing at 850 K. The subsequent monatomic Cu_2N layer growth was performed by sputtering with N_2 at 1 kV and annealing to 600 K. The single Fe atoms were then deposited on the precooled sample with a low flux of Fe vapor from a Knudsen cell. The Fe-trimer was built on the prepared surface by atom manipulation inside the STM. In this structure, the three Fe atoms are positioned along a Cu-N chain on Cu binding sites with a two lattice site spacing which corresponds to 0.72 nm. This positioning leads to a pronounced antiferromagnetic coupling between their spin moments [LvBT+10, LBL+12, YCB+15a, YCB+15b].

By applying a magnetic field and picking up several Fe atoms on the tip apex a spin-polarized tip is formed [Bod03, Wie09]. The spin-polarized tip allows for imaging of the magnetization direction of individual Fe atoms and indeed constant current maps of the trimer performed with this spin-polarized STM reveal a strong spin contrast, see **Figure 3.2**c) and d). When a field of 1 T is applied along the chain direction, the side atoms appear taller than the center atom. The spin contrast verifies that under this measurement condition the Fe atoms of the trimer interact antiferromagnetically with each other and form a stable Néel-like magnetic ground state [NR09]. This means that in the ground state each Fe atom carries a defined magnetic moment, which is parallel and antiparallel to the external magnetic field for the side atoms and the central atom respectively.

The origin of the spin contrast can be explained by treating the problem as a magneto tunnel junction [TP01, ZP06]. The picked up Fe atoms form a magnetic cluster at the tip apex with a magnetization parallel to the applied magnetic field. The magnetoresistance depends on the relative orientation of the atom moment and the magnetization of the tip. If they are parallel the resistance is low and the atom appears taller, in the opposite case the atom appears smaller because of the larger resistance. A more in depth explanation is given in section 3.6 starting on page 41.

In the following the current voltage curves *I(V)* and conductance spectra d*I*/d*V* recorded with the STM tip positioned above one side atom are discussed. The given geometry can be pictured as a double barrier geometry in which the Fe-trimer is embedded in, see **Figure 3.2**e). On one side the Fe-trimer is coupled through the Cu_2N barrier to the electronic bath of the Cu substrate. On the other side the Fe-trimer is coupled at the side atom to the electronic bath of the STM tip through the vacuum barrier. While the coupling through the Cu_2N layer is fixed, the strength of the coupling through the vacuum is tunable by altering the tip sample distance. Additionally, the setup allows the electronic bath of the STM tip to be made spin polarized.

3.3 The discovery of NDR

In the this section the current voltage *I*(*V*) curves featuring NDR behavior are presented, see **Figure 3.3**. The *I*(*V*) curves show an *ohmic* trend for small bias voltage amplitudes. For larger bias voltage magnitudes non-linear effects set in and different behav-

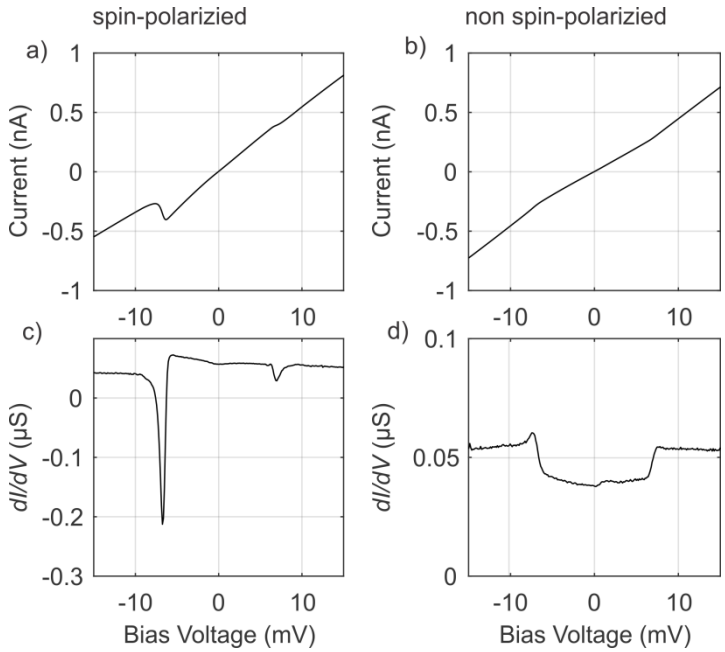

Figure 3.3 (a-b) current voltage curves *I(V)* recorded with a spin-polarized and a non-spin-polarized tip on the side atom of the Fe trimer (small arrow in **Figure 3.2** (c-d)) (setpoint 54 nS at +15 mV). (c-d) Differential conductance spectra d*I*/d*V* recorded simultaneously with the *I(V)* curves.

ior for tips with and without spin polarization is observable.

In the $I(V)$ recorded with a SP-tip, in the voltage range between –6 mV and –7.5 mV the tunnel current drops with further increasing voltage, i.e. NDR occurs, see **Figure 3.3**a). In the simultaneously recorded differential conductance spectra dI/dV the NDR appears as a pronounced dip at which the differential conductance becomes negative, see **Figure 3.3**b). For positive bias voltages a similar, but much weaker, dip is found at +6.7mV.

The $I(V)$ recorded without a spin-polarized tip shows quite different behavior. The non-SP $I(V)$ does not feature a NDR but, instead, two kinks. The kinks are at a bias voltage magnitude of 6.8 mV symmetric around zero and related to steps in the dI/dV. These kinds of features have been reported previously, and are due to the onset of inelastic tunneling processes [HGLE04, HLH06]. At such voltage magnitudes the tunneling electrons are able to promote the spin system into an excited state, which leads to the opening of inelastic tunneling channels.

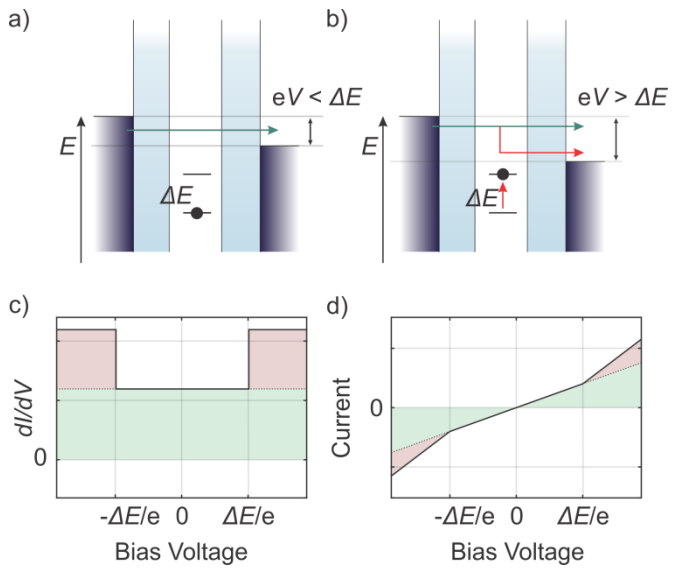

Figure 3.4 Principle of inelastic tunneling spectroscopy (IETS). (a) Only elastic current (green) flows for small bias voltages V. (b) An inelastic current channel (red) opens for larger voltages when tunneled electrons can exchange their energy to an excitation and still tunnel into unoccupied states. The additional channel will appear as steps in the dI/dV (c) and as kinks in the $I(V)$ (d). If there is no other selection rule the steps appear symmetric around zero bias and at the voltage corresponding to the energy of the excitation.

The concept of inelastic tunneling spectroscopy (IETS) is widely used to investigate non electronic excitation such as phonons [HLH00] or spin excitations [HGLE04] which are typically not involved in the electronic density of states of the sample. The idea of IETS is that at sufficiently large voltages electrons can transfer their energy by exciting the investigated system and still tunnel into unoccupied states. This possibility increases the tunnel rate, and results in a step appearing in the dI/dV when the voltage threshold which provides sufficient energy is surpassed, see **Figure 3.4**.

The comparison of spectra recorded with and without spin polarization gives a strong indication for the origin of the observed NDR:

- The NDR is spin-dependent, since it only occurs in the presence of a spin-polarized tip.
- The NDR is related to the spin excitation of the Fe-trimer because the observed IETS steps in the non-SP configuration appear at the same voltage amplitude as the dips in the spin-polarized case.
- The NDR is not caused by resonant tunneling into sharp electronic states as found in molecules [RMS+05], non-magnetic clusters or dopants [RTO+16], since no of such states were detected in the dI/dV. In addition, a NDR caused by resonant tunneling should also appear for non-SP tips.

Starting from these considerations, the NDR behavior can be explained by considering the dynamics induced by the inelastic tunneling electrons. It can be presumed that the triggered dynamics effectively alter the magnetic state of the trimer which will have a severe impact on the current flow, as the tip is spin-polarized and the tunnel current is strongly affected by the magnetization of the trimer. Such a mechanism could then lead to the observed NDR. An important indication of such a process is the requirement of tunnel rates which are on the same order as the inherent dynamics of the system. Indeed it was found that at temperatures of 0.5 K spin-excitation of the trimer can reach lifetimes of microseconds [YCB+15a]. This suggests that tunnel currents larger than hundreds of femtoampere can lead to non-equilibrium transport effects. The dynamic nature of the NDR mechanism

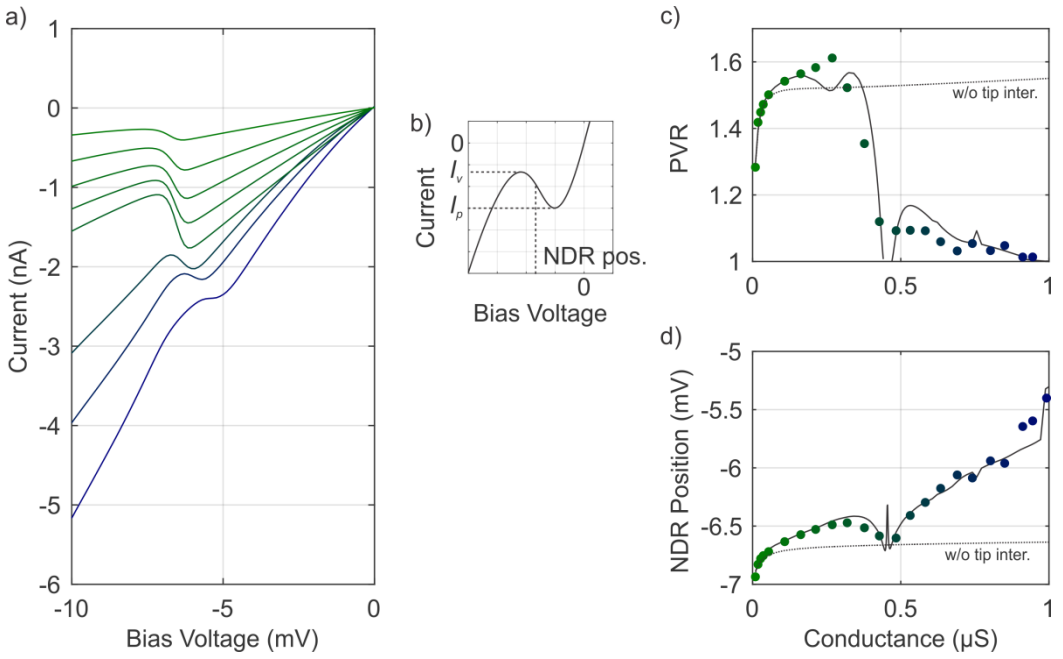

Figure 3.5 (a) *I(V)* curves recorded on the side atom of the Fe trimer using a spin-polarized tip with different junction conductance from 0.01μS to 1.06μS junction conductance. (b) The NDR position as well as the peak-to-valley ratio (PVR= I_p/I_v) is calculated for all the *I(V)* curves. (c,d) The NDR position and PVR plotted as function of conductance (colored points: experimental data). In addition to the data, the PVR-values and NDR positions from the numerical model are also shown (solid line: with tip interaction, dotted line: without tip interaction).

should be affected by an altered the tunneling rate, and conductance dependent measurements were therefore performed.

The $I(V)$ curves recorded with increasing conductance show strong variations of NDR, see **Figure 3.5**. The variation can be quantified with two observables: the magnitude of the NDR and its voltage position. The strength of the NDR is given by the peak-to-valley ratio (PVR) [Gru06] and the position is defined by the voltage position with the strongest negative slope (corresponding to the dip position in the dI/dV).

For small setpoint conductances between 10 nS and 270 nS (referenced at +15 mV) the PVR increases with increasing conductance until it reaches its maximum of about 1.61 at 270 nS. Between 270 nS and 420 nS the PVR breaks down and at a conductance of 950 nS it vanishes completely. In this range, the position of the NDR also changes significantly starting at −6.9 mV and reaching −5.4 mV. These observations support the conclusion that

the NDR mechanism is due to the dynamics triggered by tunneling electrons interacting

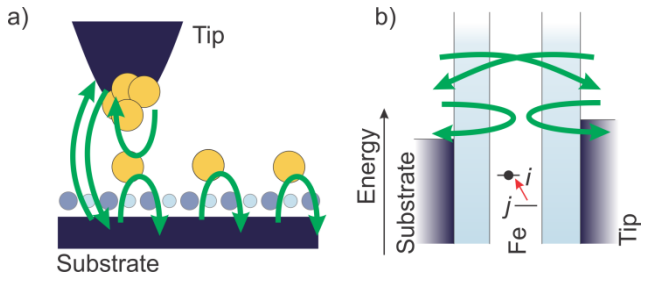

Figure 3.6 Graphical representation of the possible electron transition paths (blue arrows) leading to the net spin state transition rates (red arrow).

with the Fe-trimer.

3.4 Rate equation and effective spin Hamiltonian

The experiment shows that the observed NDR results from non-equilibrium transport properties. Inelastic tunnel electrons are inducing dynamics which possibly lead to a change in the magnetization of the Fe-trimer and therefore to the observed NDR. A more quantitative picture of the NDR is necessary to achieve a deeper understanding of the underlying physics which have so far only been hinted at.

The problem was modeled using a rate equation approach. In this model the state of the Fe-trimer is represented by the statistical probabilities to find the Fe-trimer in one of its spin states and its evolution which is given by the following differential equation:

$$\frac{\mathrm{d}n_i(t)}{\mathrm{d}t} = \sum_{j=1}^{N}\left[r_{ij}n_j(t) - r_{ji}n_i(t)\right], \qquad 3.1$$

here $n_i(t)$ is the statistical probability to find the Fe-trimer in spin state i, r_{ij} is the transition rate from state j to state i and N is the total number of spin states taken into account. Since $n_i(t)$ are statistical probabilities an important boundary condition is the imposition of $\sum_{j=1}^{N} n_i(t) = 1$ for all times. The transition rates r_{ij} of the trimer are directly linked to the rates of all electrons interacting with the Fe-trimer and causing the transitions, which are in particular the electron tunneling between tip and substrate [LvBT+10, LLH10,

Ter15]. In the case of the tip being positioned above the side atom (1) the following electron rates occur:

- Electrons tunnel from the tip (t) into the Cu substrate (s) and interact with the side atom (1) ($s \leftarrow 1 \leftarrow t$) and vice versa ($t \leftarrow 1 \leftarrow s$) .
- Electron backscatter from the side atom back into the tip ($t \leftarrow 1 \leftarrow t$).
- Electron backscatter from one of the three atoms ($a = 1, 2, 3$) into the substrate ($s \leftarrow a \leftarrow s$).

All of these possibilities are illustrated in **Figure 3.6** and their sum comprises to the net transition rate r_{ij}:

$$r_{ij} = r_{ij}^{s \leftarrow 1 \leftarrow t} + r_{ij}^{t \leftarrow 1 \leftarrow s} + r_{ij}^{t \leftarrow 1 \leftarrow t} + \sum_{a=1}^{3} r_{ij}^{s \leftarrow a \leftarrow s} , \qquad 3.2$$

where $r_{ij}^{k \leftarrow a \leftarrow m}$ represents the rate of electrons transmitted from electrode m to electrode k through atom a of the trimer, causing the transition of the spin state from j to i.

The demonstrated link between the spin state transition and electron transmission rates results from the interaction of the electrons with the trimer. The nature of this interaction is electron-spin scattering and can, analogous to a Kondo-type scattering [App67, DPFR10, Ter15], be described with a Hamiltonian of the form:

$$\widehat{H}_i = \hat{\vec{S}}\,\hat{\vec{\sigma}} + u\,\hat{I} , \qquad 3.3$$

where $\hat{\vec{S}}$ is the quantum mechanical spin vector operator evaluated at the atom at which the electron scatters and $\hat{\vec{\sigma}}$ is the corresponding spin vector operator of the scattered electron. The second term accounts for spin-independent electron scattering where $\hat{I}$ is the identity operator is and u gives the scattering strength. The interaction Hamiltonian connects the Hamiltonian of the two electron baths of tip and sample with the Hamiltonian of the trimer. The transition rates are derived from the scattering Hamiltonian by perturbation theory that, to first order, results in *Fermi's Golden rule* [Sak94]. In the framework of elastic and inelastic tunneling the successful use of a scattering Hamiltonian $\widehat{H}_i$ has been

reported for the study of magnetic atoms and molecules [KK04, FR09, LvBT+10, Ter15]. By treating the perturbation to higher order terms, transport phenomena like Kondo resonances (in a weakly coupled regime) can also be explained [Ter15]. The transmission rates are given by:

$$r_{ij}^{k\leftarrow a\leftarrow m} = \frac{G^{k\leftarrow m}}{e} \sum_{\{\sigma,\sigma'\}=\{+\frac{1}{2},-\frac{1}{2}\}} \iint \mathrm{d}\epsilon\, \mathrm{d}\epsilon'\; f(\epsilon)\left(1 - f\left(\epsilon' - eV^{k\leftarrow m}\right)\right) \times$$
$$\left(\frac{1}{2} + \sigma\eta_k\right)\left(\frac{1}{2} + \sigma'\eta_m\right) \times \left|\left\langle i,\sigma\middle|\hat{\vec{S}}_a\,\hat{\vec{\sigma}} + u\,\hat{I}\middle|j,\sigma'\right\rangle\right|^2 \delta\left(\epsilon - \epsilon' - \Delta\epsilon_{ij}\right), \qquad 3.4$$

where $r_{ij}^{k\leftarrow a\leftarrow m}$ is the rate leading to a transition from spin state j to i caused by electrons that are transmitted from electrode m (tip or sample) to electrode k (tip or sample) and thereby interact with atom a. The right hand side of the equation can be split up into four parts. The constant $G^{k\leftarrow m}$ is the strength of the conductance between the electrodes k and m, and has units of [A/V]. For example, $G^{t\leftarrow s}$ or $G^{s\leftarrow t}$, the conductance between tip (t) and sample (s), are on the order of the tunnel conductance ($I_{\mathrm{set}}/V_{\mathrm{set}}$). This term is followed by a summation of the possible spin state of the electron before and after the scattering process, σ and σ', and a double energy integral over the electron energy before and after the scattering, ϵ and ϵ'. The integral is evaluated at occupied states in the electrode m given by $f(\epsilon)$ and the unoccupied states in electrode k, $1 - f\left(\epsilon' - eV^{k\leftarrow m}\right)$, which are shifted by the voltage $\mathrm{V}^{k\leftarrow m}$. Although a flat density of states is assumed for the electrodes, their spin polarization $\eta = [-1,1]$ is taken into account. This results in a different density of states for spin up d_+ or spin down d_- electrons and is given by:

$$d_+ = \frac{d_0}{2}(1+\eta) \text{ and } d_- = \frac{d_0}{2}(1-\eta)\,. \qquad 3.5$$

Here d_0 is the density of states of the un-polarized electrode which is included in $G^{k\leftarrow m}$. The last part of equation (3.4) results from *Fermi's Golden* rule and includes a matrix scattering element and a delta function which ensures energy conservation. Here $\Delta\epsilon_{ij} = \epsilon_i - \epsilon_j$ is the energy difference between the spin state i and j.

The calculation of the matrix scattering element requires knowledge of the eigenfunction of the unperturbed system. For the problem treated here, the spatial part of the wave function is neglected and the remaining spin part is written as a product state of the spin of the electron $|\sigma\rangle_e$ and an effective spin wave function of the trimer $|j\rangle$:

$$|j,\sigma\rangle = |j\rangle \otimes |\sigma\rangle_e. \tag{3.6}$$

Based on the tip polarization the eigenfunction $|\sigma\rangle_e$ of the electronic part can be assumed to be the eigenvectors of the $\hat{\sigma}_z$ operator which are $|+1/2\rangle_e$ or $|-1/2\rangle_e$, since the magnetic field is applied along the z-direction, and the electrodes are treated as ordinary metals without intrinsic anisotropies. The spin wave function of the trimer $|j\rangle$ is more complicated and can found by describing the trimer with an effective spin Hamiltonian [BLF13, GSV11]:

$$\hat{H}_{\text{trimer}} = \sum_{i=1}^{3}\left[D_i\,\hat{S}_{z,i}^2 + E_i\,(\hat{S}_{x,i}^2 - \hat{S}_{y,i}^2) + g_i\,\mu_B\,\vec{B}\,\hat{\vec{S}}_i\right] + \sum_{i=1}^{2} J_{i(i+1)}\,\hat{\vec{S}}_i\,\hat{\vec{S}}_{i+1} + \hat{H}_{\text{tip}}\,. \tag{3.7}$$

The spin Hamiltonian includes magneto-crystalline anisotropy considering the C_{2v} symmetry of the Fe binding site and Zeeman splitting with D_i, E_i, g_i being the anisotropy energies and the g-factor of the i-th atom [HLO+07, YCB+15b]. The second term is a Heisenberg interaction which couples the spin of next neighbor atoms with strength $J_{i(i+1)}$. The last term accounts for an interaction of the trimer with the magnetization of the spin-polarized tip. Usually this term can be neglected but it will play an important role later. The magnitude of the effective spin of the Fe-atoms on Cu_2N was found to be $S = 2$ [NR09, YCB+15a] and is reflected in the matrix representation of the spin operators.

Numerical direct diagonalization of the trimer Hamiltonian (3.7) leads to 125 eigenstates $|j\rangle$ with eigenenergy ϵ_j, see **Figure 3.8**. Beginning with the extracted spin eigenstates all transition rates can be calculated and the rate equation (3.1) is completely defined.

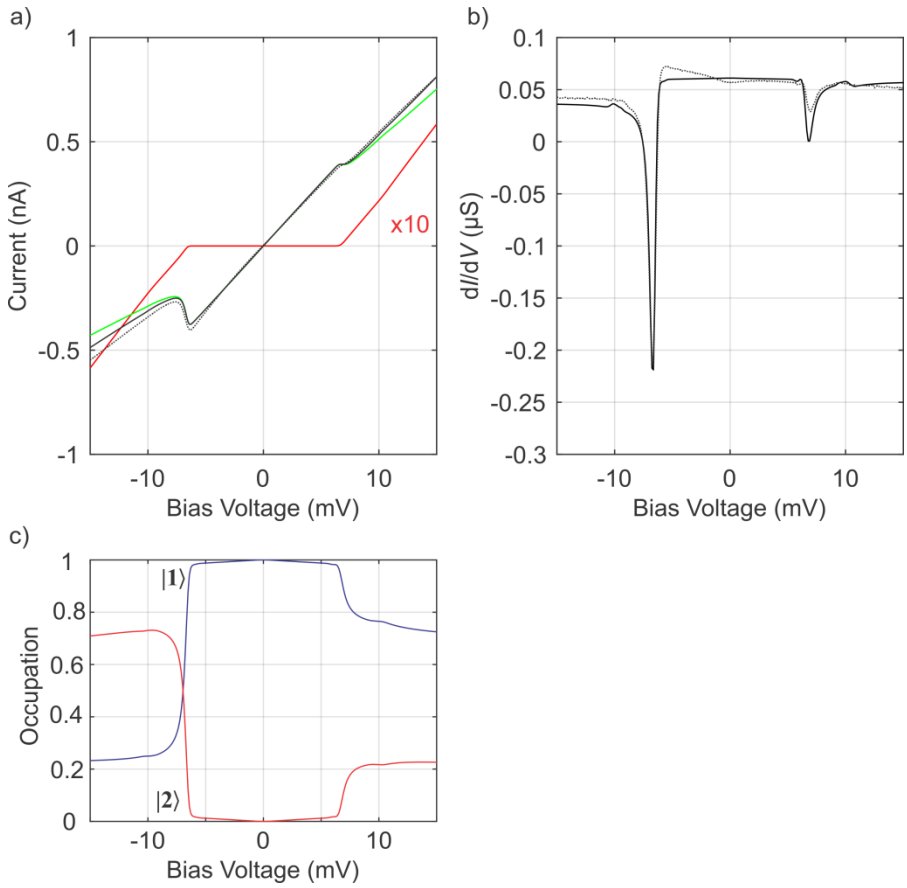

Figure 3.7 (a) Calculated (black line) and recorded (black dotted line) $I(V)$ curves for a spin-polarized tip positioned above the side atom of the Fe trimer. The contribution of the elastic (green) and inelastic (red, x10 magnified) are additionally shown. (b) The calculated (black line) and recorded (black dotted line) differential conductance spectra dI/dV corresponding to the $I(V)$ in (a). (c) Occupation of the two low lying spin states ($|1\rangle, |2\rangle$) as function of bias voltage.

3.5 Numerical *I(V)*

The goal of the rate equation approach is to model the dynamics of the Fe-trimer and to connect them to the observed negative differential conductance. This is achieved by calculating a numerical *I(V)* curve using the model and comparing it to the measurements.

For given model parameters, certain rates between the electrodes $r_{ij}^{k\leftarrow a\leftarrow m}(V)$ result. These rates depend in particular on the applied voltage between tip and sample $V = V^{t\leftarrow s} = -V^{s\leftarrow t}$. The average contribution of each rate to the electron flow depends on the mean occupation $n_j(t,V)$ of the initial state. The net electron flow between the tip and

the sample is therefore given by the weighted average of the rate difference $r_{ij}^{s\leftarrow 1\leftarrow t}(V) - r_{ij}^{t\leftarrow 1\leftarrow s}(V)$, which gives the tunnel current:

$$I(V,t) = e\sum_{i,j}\left[r_{ij}^{s\leftarrow 1\leftarrow t}(V) - r_{ij}^{t\leftarrow 1\leftarrow s}(V)\right] n_j(t,V). \qquad 3.8$$

Since the mean occupation $n_j(t,V)$ varies with time, so does the resulting current *I(V,t)* and does not necessarily correspond to the static current measured in a typical *I(V)* measurement. The static current is computed with the steady state solution $\tilde{n}_j(V)$ of the rate equation:

$$\left.\frac{\mathrm{d}n_i(t)}{\mathrm{d}t}\right|_{\tilde{n}_i} = \sum_{j=1}^{N}\left[r_{ij}\,\tilde{n}_j - r_{ji}\,\tilde{n}_i\right] = 0. \qquad 3.9$$

This leads to the numerical $I(V)$ curve. The parameters of the model can be adjusted to fit the numerical solution to the experimental data. The fitting procedure is explained in detail in the supplemental section 6.1 and leads to a remarkable match between recorded measurement and numerical solution, shown in **Figure 3.7**a) and b). The model is capable of reproducing the asymmetry in the I(V) and, in particular, the NDR with the observed strength and at the right position. Some smaller features in the dI/dV also match between measurement and calculation, such as a step at +10.3 mV as well as a small indention at -8.7 mV. Other features like the kink in the dI/dV around zero bias are not captured by the model. This kink most likely has its origin in higher order scattering terms [Ter15] or in residual features of the density of states of the tip or sample.

Despite the small features which are not captured, the recorded $I(V)$ is well described by the model. The mechanisms leading to the NDR in the model therefore also reflect the mechanisms in the real system to a very good approximation, allowing these mechanisms to be understood in great detail. To understand this mechanisms, the modeled $I(V)$ current is first separated into its elastic and inelastic part. The inelastic tunnel current has a fast onset at voltages $|V| > 6.4$ mV and increases monotonically with larger voltage magnitudes, as shown in **Figure 3.7**a). Simultaneously to the onset of the inelastic current at

negative voltage polarity, the elastic current drops leading to the observed NDR. Similar to the observation of inelastic tunneling steps with a non SP-tip at the same voltage position as the NDR with a SP-tip, this finding also points to the strong connection between inelastic tunnel processes and the appearance of NDR.

Furthermore, the calculation allows the examination of the steady state spin state occupation, see **Figure 3.7**c). The steady solution of the average spin state occupation as a function of the applied voltage shows that in the relevant voltage regime the trimer is mainly occupying two states, $|1\rangle$ and $|2\rangle$. In fact, the probability of finding the trimer in one of these two states is always larger than 94%. As such, the transition rates involving these states will dominate the tunnel current. The relative occupation of these states changes suddenly at the onset of the inelastic currents. For negative biases the change is even more drastic and the occupation of the two low-lying states reverses. In the next section this is shown to be a key ingredient for the manifestation of the spin-based NDR.

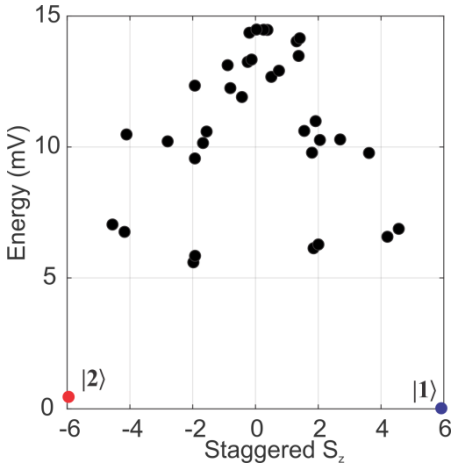

Figure 3.8 Level diagram of the lowest spin-eigenstates of the Fe trimer (corresponding to the tunnel conductance used in **Figure 3.7**). The eigenstates $|j\rangle$ are plotted as function of their eigenenergy ϵ_j and their mean staggered magnetization $\langle S_z\rangle_{j,\text{staggered}}$. The two low lying states $|1\rangle$ and $|2\rangle$ are marked in blue and red respectively.

3.6 Spin states

A good starting point to understand the role of the spin states $|j\rangle$ of the trimer is the energy diagram of the states, plotted as a function of their mean staggered magnetization $\langle S_z\rangle_{j,\text{staggered}}$, see **Figure 3.8**. The mean staggered magnetization is defined here as follows:

$$\langle S_z\rangle_{j,\text{staggered}} = \langle j|\sum_{i=1}^{3}(-1)^{i+1}\,\hat{S}_{z,i}\,|j\rangle = \langle j|+\hat{S}_{z,1}-\hat{S}_{z,2}+\hat{S}_{z,3}|j\rangle \qquad 3.10$$

The energy diagram reveals that the trimer features two low lying spin states which are separated from the higher excited states by a gap of 5.1 meV between highest low lying state and the lowest higher excited state. The two low lying spin states are the two most occupied states ($|1\rangle, |2\rangle$) identified in the last section. The staggered magnetization magnitude of both states is almost six, while all the excited states have smaller staggered magnetization magnitudes.

The Fe-trimer spin states can be described by writing them as a superposition of product states of the z-component of the spin m_s of each Fe atom:

$$|j\rangle = \sum_{m_{s,1},m_{s,2},m_{s,3}} A_{m_{s,1},m_{s,2},m_{s,3}} \; |m_{s,1}, m_{s,2}, m_{s,3}\rangle$$
$$|m_{s,1}, m_{s,2}, m_{s,3}\rangle = |m_{s,1}\rangle \otimes |m_{s,2}\rangle \otimes |m_{s,3}\rangle \,, \qquad 3.11$$

with $m_s = \{-S, -S+1, \ldots\ldots, S-1, S\}$.

In this formalism the two low lying state are represented by:

$$|1\rangle = \quad 0.985\,|2,-2,2\rangle \quad - 0.089\,|1,-1,2\rangle - 0.087\,|0,-2,2\rangle \quad + \cdots$$
$$|2\rangle = -0.985\,|-2,2,-2\rangle + 0.091\,|0,2,-2\rangle + 0.089\,|-1,1,-2\rangle + \cdots \qquad 3.12$$

To good approximation the two states $|1\rangle$ and $|2\rangle$ are of Néel-character, which also explains their large staggered magnetization. The ground state is $|1\rangle \approx |2,-2,2\rangle$, and the first excited state is $|2\rangle \approx |-2,2,-2\rangle$.

In the ground state $|1\rangle$ the magnetic moments of the side atoms are parallel to the applied magnetic field and the magnetic moment of the center atom is antiparallel. This is directly observed in the constant-current topography recorded with a SP-tip and has been already discussed with respect to the different topographic heights of the atoms, see **Figure 3.2**. For the first excited state $|2\rangle$ the magnetic moments are flipped. Since the two states are indistinguishable for the anisotropy as well as for the interaction term of the Spin Hamiltonian, the energy splitting between them is caused exclusively by the difference of the net magnetic moment and the applied magnetic field, which yields a Zeeman-splitting of 0.46 meV/T.

The identification of the two dominant states ($|1\rangle, |2\rangle$) as the two Néel like states $|2,-2,2\rangle$ and $|-2,2,-2\rangle$ directly leads to the conclusion that the occupation of these two states will result in different magnetoresistance s. As mentioned earlier, the spin-polarized tip is located above the side atom ($a = 1$) during the measurement and will, therefore, sense its spin configuration. If the trimer is in state $|1\rangle$ the side atom is in the spin-configuration of +2 which corresponds to a magnetic moment parallel to the tip, resulting in a low magnetoresistance . On the other hand, a large magnetoresistance is observed if the trimer is in state $|2\rangle$ and the side atom is in the –2 spin configuration. This connection can be seen

more formally in the transition matrix elements $M_{ii,1}$ responsible for the elastic current, which are evaluated at the side atom ($a = 1$), given in equation (3.4):

$$M_{ii,1} = \left|\left\langle i,\sigma\left|\hat{\vec{S}}_1\,\hat{\vec{\sigma}} + u\,\hat{I}\right|i,\sigma\right\rangle\right|^2. \qquad 3.13$$

For negative bias voltages, electrons with $\sigma = +\frac{1}{2}$ tunnel most dominantly in the tip because of its spin polarization which hinders the tunneling of electrons with $\sigma = -\frac{1}{2}$. The elastic matrix elements for $\sigma = +\frac{1}{2}$ electrons resulting for the two states $|1\rangle$ and $|2\rangle$ are:

$$\begin{aligned} M_{11,1} &= \left|\left\langle(+\mathbf{2},-2,+2),+\frac{1}{2}\left|\,\hat{\vec{S}}_1\,\hat{\vec{\sigma}} + u\,\hat{I}\,\right|(+\mathbf{2},-2,+2),+\frac{1}{2}\right\rangle\right|^2 = \left|(+2)\left(+\frac{1}{2}\right)+u\right|^2 \\ &= |u+1|^2\,, \text{and} \\ M_{22,1} &= \left|\left\langle(-\mathbf{2},+2,-2),+\frac{1}{2}\left|\,\hat{\vec{S}}_1\,\hat{\vec{\sigma}} + u\,\hat{I}\,\right|(-\mathbf{2},+2,-2),+\frac{1}{2}\right\rangle\right|^2 = \left|(-2)\left(+\frac{1}{2}\right)+u\right|^2 \\ &= |u-1|^2. \end{aligned} \qquad 3.14$$

Hence for $u = (1.1 \pm 0.3)$ (see **Table 6.1**), occupying state $|1\rangle$ will result in a large elastic transition matrix element which will lead to a lower magnetoresistance R_1 and vice versa

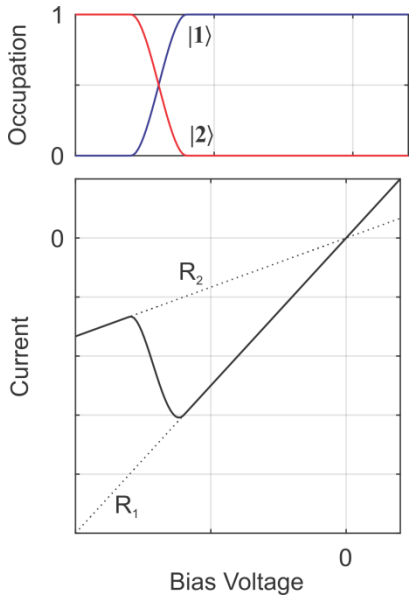

Figure 3.9 When state $|1\rangle$ is occupied the resistance is R_1 and when state $|2\rangle$ is occupied the resistance is R_2. By changing the occupation (top) the resulting *I(V)* (bottom, line) switches between the two ohmic trends which can result in NDR.

for occupying state $|2\rangle$. Based on this, the $I(V)$ can be simplified by $I(V) = \frac{V}{R_1} n_1 + \frac{V}{R_1} n_2$ with $R_1 < R_2$ and $n_1 + n_2 = 1$. In this case, if the occupation changes from $n_1 = 1$ to $n_2 = 1$ NDR occur if the voltage interval necessary for the change is sufficiently small, see Figure 3.9. As anticipated in the previous section, the occupation reversal of the two states $|1\rangle$ and $|2\rangle$ in a small voltage window causes a drastic change of the magnetoresistance which leads to the observed NDR.

The process which causes the reversal of the states and its connection to the inelastic current onset is the last ingredient required to fully understand the NDR. In the next section it will be shown that the reconfiguration is based on a two-step excitation process triggered by inelastic electrons and that the long lifetime of the high resistance state is responsible for the effectiveness of the reconfiguration.

3.7 Two-step excitation process

According to rate equation 3.1, changes of the state occupation $n_i(t)$ are related to inelastic electron scattering events by the transition rates r_{ij} with $i \neq j$. During each inelastic scattering event the electron exchanges energy and spin angular momentum with the Fe-trimer. It is important to recognize that in such an event the electron can only transfer momentum of ±1ħ depending on its own initial spin-state since electrons are spin ½ particles. This selection rule will suppress transitions between spin states exhibiting a spin

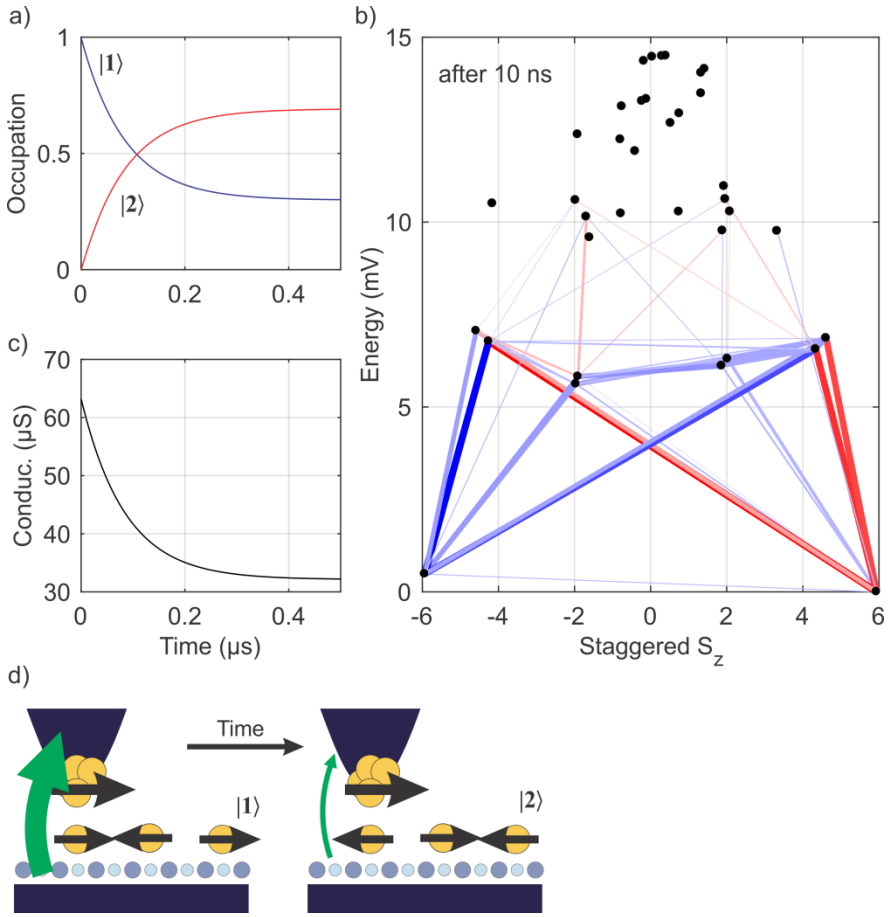

Figure 3.10 (a) Time evolution of the two low lying states |1⟩ and |2⟩ of the Fe trimer by applying a -8 mV voltage and starting from a Boltzmann-distributed occupation. (b) A detailed picture of the ongoing redistribution after 10 ns. Lines indicate the most dominant occupation change rates. Red lines are net excitations and blue lines net de-excitations. (c) The conductance of the elastic tunneling channel as a function of time. (d) Graphical representation of the time evolution of the population and the elastic tunnel conductance (size of green arrow).

on the side atom that differ by more than ±1ħ.

At zero voltage the occupation is exclusively thermally driven and at our measurement conditions this leads to a negligible occupation of the excited states. Although $|1\rangle$ and $|2\rangle$ are separated by only 460 μeV, due to momentum conservation the direct transition from $|1\rangle \approx |2,-2,2\rangle$ into $|2\rangle \approx |-2,2,-2\rangle$ (and vice versa) is essentially forbidden. However a residual admixture of $|-1,2,-2\rangle$ and $|1,-2,2\rangle$ states leads to a slow change of the occupation for bias voltages below the inelastic excitation threshold, see **Figure 3.7**c). The situation changes for larger voltages if tunneling electrons have enough energy to excite into higher spin states $\{|e\rangle\}$ which exhibit a significant contribution of $|1,-2,2\rangle$.

Once the trimer has been excited, depending on all the evolving rates, different paths can follow, for example:

- The trimer can relax quickly from $|e\rangle$ to $|2\rangle$ and slowly decay back into $|1\rangle$.
- The trimer can relax quickly from $|e\rangle$ to $|2\rangle$ and then re-excite into $|e'\rangle$.
- The trimer can be further excited from $|e\rangle$ to $|e'\rangle$ and then relax into $|1\rangle$ or $|2\rangle$.

These three examples and all other possibilities will be taken into account by the complete rate equation model. To have a complete picture of the overall effect of these processes, the time evolution of the state occupation is calculated, see **Figure 3.10**. This calculation reveals that two step excitations such as $|1\rangle \rightarrow |e\rangle \rightarrow |2\rangle$ or vice versa (similar to the second example) lead to a non-thermal occupation of the two lowest spin states. The non-thermal occupation is possible because the relaxation rate from $|2\rangle \rightarrow |1\rangle$ ($\approx 0.6\ 10^6 \mathrm{s}^{-1}\ \widehat{=}\ 0.1$ pA) is small and an inelastic tunnel current with this amplitude can be achieved by a small increment of the bias voltage window after the inelastic threshold, see **Figure 3.7**. The fact that state $|2\rangle$ becomes more occupied than state $|1\rangle$ is caused by an imbalance of the transition rates resulting from the spin polarization of the tip.

As mentioned, for the excitation of the low lying states $|1\rangle$ and $|2\rangle$, the momentum selection rule has to be considered. For the excitation process $|1\rangle \approx |2,-2,2\rangle \rightarrow |e\rangle \approx |1,-2,2\rangle$ the spin state has to be decreased by 1ħ and correspondingly increased to excite from state $|2\rangle$. In order to allow this change of the spin state the spin of scattered electron has to

change accordantly. In the first case the electron spin state has to flip from $|-1/2\rangle_e$ to $|+1/2\rangle_e$ and in the second case from $|+1/2\rangle_e$ to $|-1/2\rangle_e$. For negative bias voltages electrons tunnel into unoccupied states of the tip and the tunnel probability to tunnel into a $|+1/2\rangle_e$ spin state is larger because of the tip's spin polarization. Hence, inelastic processes flipping $|-1/2\rangle_e \rightarrow |+1/2\rangle_e$ will occur with higher likelihood, such as the excitation of state $|1\rangle$. State $|2\rangle$ will become more populated since the Fe-trimer is excited out of $|1\rangle$ more easily.

In fact, for positive bias polarities, electrons tunnel out of the tip and the scattering events flipping $|+1/2\rangle_e \rightarrow |-1/2\rangle_e$ become more likely because of the spin polarization of the tip favoring $|+1/2\rangle_e$ electrons. In light of this consideration, the asymmetry between positive and negative bias voltages in the spectra can be explained.

In conclusion, the NDR results from a dynamic switch of the trimer into the first excited state, caused by inelastic electron tunneling. This switch accompanies a change of the magnetoresistance form low to high, which is sensed by the elastic tunnel current resulting in the observed NDR. This description of the NDR also explains the observed increase of the peak-to-valley ratio with increasing tunnel junction conductance since the spin state reconfiguration will become more efficient for larger tunnel rates. On the other hand, the upper bound of the PVR, and its breakdown along with the voltage shift of the NDR position cannot yet be explained, see **Figure 3.5**. The explanation of these effects lies in the magnetic interaction between tip and the trimer and is described in the next section.

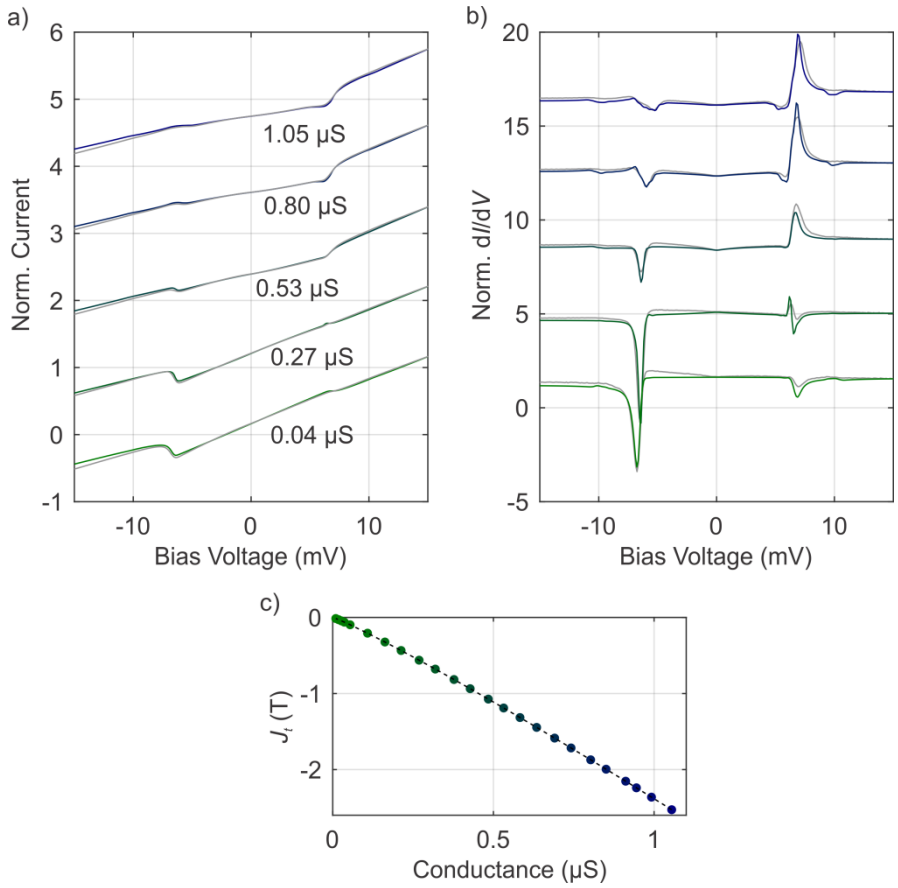

Figure 3.11 (a) normalized $I(V)$ curves for increasing tunnel junction conductance. (Colored lines: calculation, grey lines: recorded data). The lines are shifted for better visibility. (b) The corresponding differential conductance spectra dI/dV. (c) The strength of the tip interaction counteracting the applied magentic field in Tesla [T] as function of conductance.

3.8 Tip interaction

Although the model has so far succeeded in describing many aspects of the spectra and the NDR behavior, the variation observed for large junction conductances has not yet been captured, see **Figure 3.5**. These variations indicate an increasing magnetic interaction of the Fe-trimer with the spin-polarized tip. The shift of the NDR position is an especially strong hint that the tip influences the spin states of the trimer and modifies their eigenenergies. Similar shifting is not observed in spectra recorded with a non-spin-polarized tip.

In the effective spin Hamiltonian the tip interaction is accounted for by an effective magnetic field acting only on the side atom above which the tip is positioned [YCB+15a]:

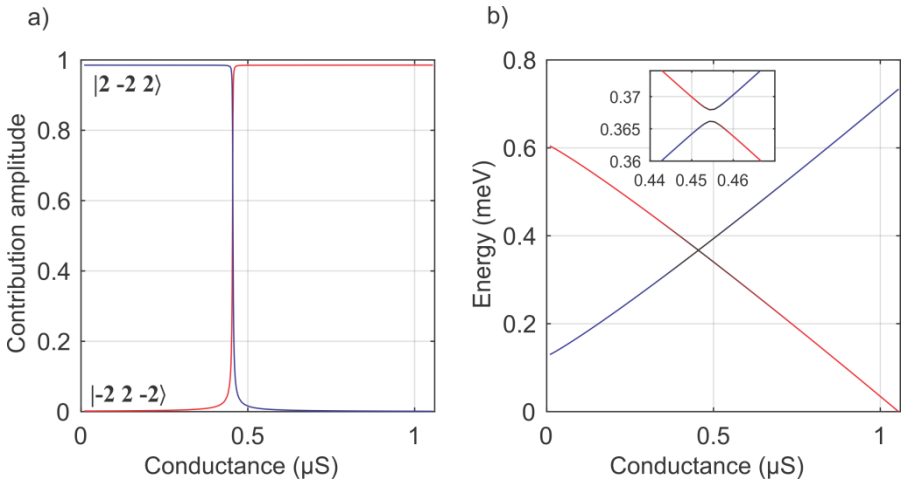

Figure 3.12 (a) magnitude of the contribution of the two Néel states $|2,-2,2\rangle$ and $|-2,2,-2\rangle$ to the ground state as a function of junction conductance. (b) Energy of the ground state and the first excited state as a function of conductance. At 0.455 μS there is an avoided level crossing (inset). At the avoided level crossing the two states interchange their character as indicated by their color. (blue: $|2,-2,2\rangle$ character, red: $|-2,2,-2\rangle$ character).

$$\hat{H}_{\text{tip}} = J_t(z)\frac{\langle\vec{M}_t\rangle}{|\langle\vec{M}_t\rangle|}\hat{\vec{S}}_1\,, \tag{3.15}$$

where $\frac{\langle\vec{M}_t\rangle}{|\langle\vec{M}_t\rangle|}$ is the direction of the mean magnetic moment of the spin-polarized tip, which is assumed to point parallel to the applied field $\vec{B}$. $J_t(z)$ is the coupling strength of the tip interaction which depends on the tip-sample distance z.

The numerical dI/dV spectra were calculated, including the tip interaction, for the investigated junction conductance regime and were fit (see supplement 6.1) to the recorded data, see **Figure 3.11**. An almost linear power law dependence between the setpoint conductance and the coupling strength J_t yields an excellent agreement between the calculated spectra and the experimental data. In agreement with the tunnel conductance tip-sample distance behavior, this dependency corresponds to an exponential increase of the interaction when decreasing the tip-sample distance. The interaction is therefore most likely due to a direct exchange interaction across the gap rather than a magnetic dipole interaction.

The tip interaction counteracts the applied magnetic field and directly affects the two low energy states $|1\rangle$ and $|2\rangle$ in two different ways. First, for stronger interaction the energy

splitting between them is reduced. Second, the two states start to mix. At a junction conductance of 0.445 μS the interaction becomes stronger than the applied field and the two states will go through an avoided level crossing. Beyond the level crossing the state $|2\rangle \approx |-2,2,-2\rangle$ is the ground state and $|1\rangle \approx |2,-2,2\rangle$ the first excited state. Directly at the avoided crossing the two low energy states have similar contributions of $|-2,2,-2\rangle$ and $|2,-2,2\rangle$, see **Figure 3.12**.

The transition through the avoided level crossing leads to an interesting effect: All dynamic processes reverse compared to low setpoint conductance. Beyond the avoided level crossing and for small voltage magnitudes the magneto resistance of the elastic current is large. Here, exceeding the inelastic tunneling threshold for negative voltages will not result in a drastic reconfiguration since the trimer is already in the high resistance state. For that reason, the NDR breaks down at the avoided level crossing and vanishes completely for even larger conductances. On the other hand, when exceeding the threshold for positive voltages, inelastic electrons will dominantly transfer -1ħ of momentum to the trimer and the two step excitation process will populate the low resistance state $|1\rangle$. In contrast to the dip at negative voltages for low conductance, at higher conductances a strong peak appears at +7.1mV.

Furthermore, the shift of the energy levels of both the low lying states and higher lying states will lead to the observed shift of the NDR position from -6.8 mV to -5.3 mV, which is also well reproduced by the model.

3.9 NDR conclusion

In this chapter the occurrence of NDR in electronic transport through a few atom spin-chain embedded in double barrier geometry has been investigated. In contrast to conventional concepts, it is not the shift of electronic states but rather the dynamic occupation of the spin states which causes NDR. Spin-polarized inelastic current induces dynamics in the spin-chain via a two-step process between the two Néel states and effectively populates a high magnetoresistance state. This process has been described in detail with a rate equation approach. The complex transport characteristics over a large con-

ductance regime (from 0.01 μS to 1.06 μS junction conductance) were reproduced with astonishing agreement, by implementing the interaction between the spin-chain and the spin-polarized tip in this model.

The dynamic process leading to NDR appears to be a general phenomenon. Indeed, the model used is not specific to the presented sample and can be adapted to describe other systems, such as magnetic molecules [ET06] and different surfaces. Moreover, the strong influence of magnetic perturbations on the NDR, such as the interaction with a spin-polarized tip, can be exploited for atomic-scale sensing, as is briefly reported in the following section of this chapter.

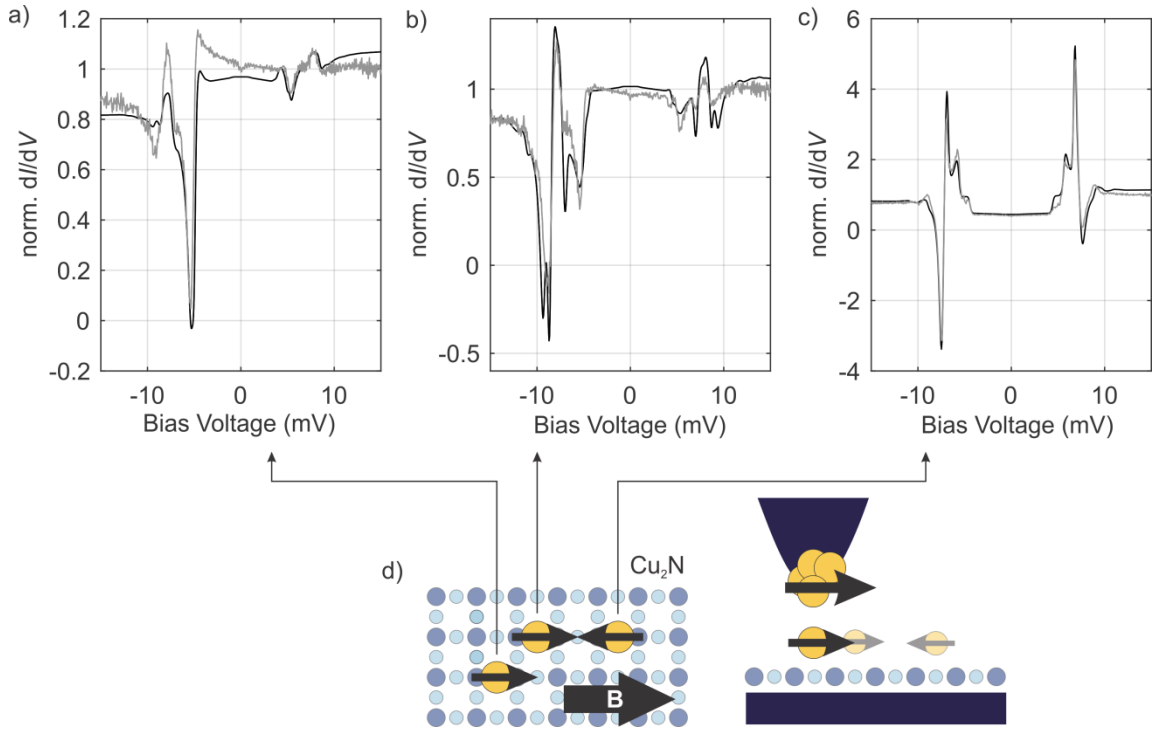

Figure 3.13 (a-c) Spin-polarized dI/dV spectra (grey lines) recorded on the three atoms of the sensor (tunnel setpoint 1 nA at 15 mV). A magnetic field of 2 T is applied along the easy axis. dI/dV curves were calculated based on the rate equation model (black lines). (d) Sketch of the experimental geometry. Black arrows indicate the direction of the magnetic moment of each Fe atom (yellow) in the ground state of the sensor trimer.

3.10 An atomic-scale magnetic sensor

In the last section of this chapter the application of the mechanisms leading to NDR as a sensor mechanism for magnetic interactions is briefly presented. The sensing mechanism is based on the modification of NDR related features in the presence of external magnetic interactions. In the previous part the interaction was caused by the spin-polarized tip, while here the interaction with a magnetic object in close vicinity to the sensor will be considered. The quantification of these changes in the spin-polarized dI/dV spectra provides a tool for investigating the magnetic object without placing the STM tip above it. This approach has the advantage that the magnetic object is much less affected by the STM tip and exhibits behavior closer to its intrinsic properties.

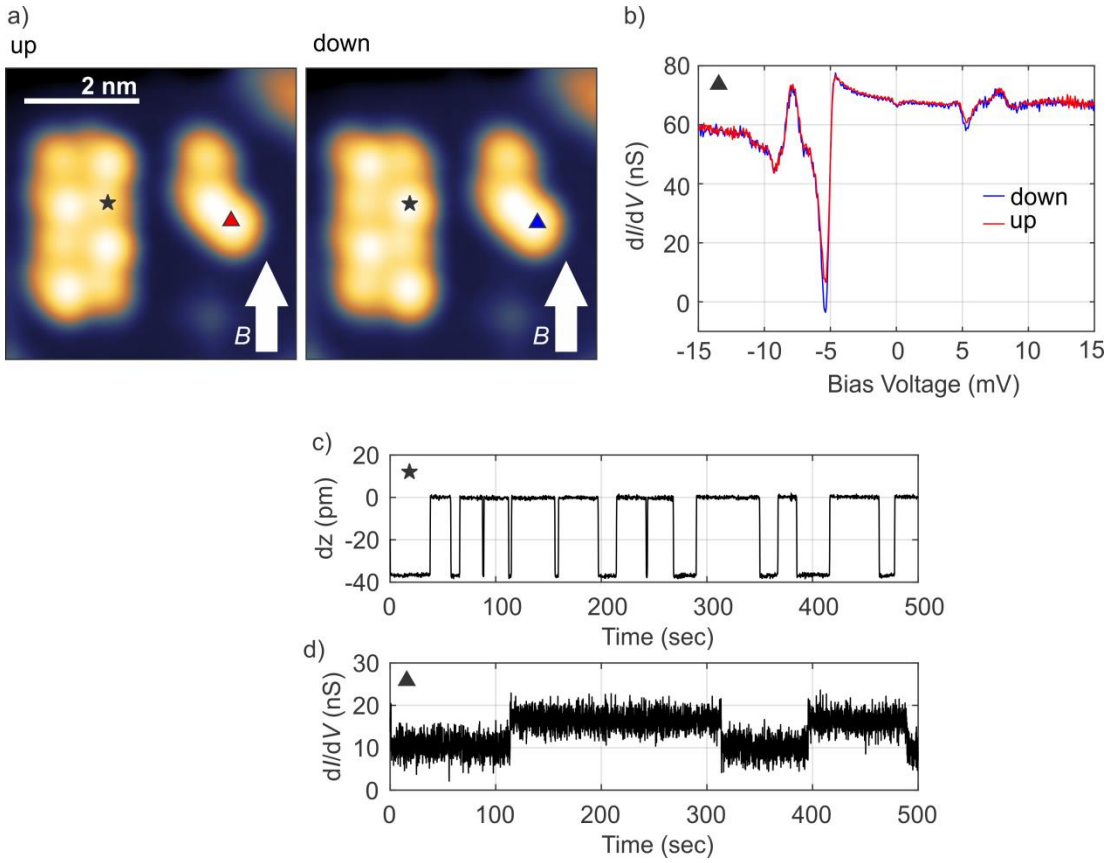

Figure 3.14 (a) Spin-polarized constant current topographies of the 2*x4* antiferromagnet and the nearby three atom sensor (tunnel setpoint 5 pA at 5 mV, magnetic field $B = 2$ T). Spin contrast reveal the two Néel states configuration (*up* and *down*) of the *2×4* magnet. (b) Spin polarized dI/dV spectra recorded on the sensor at the location marked by the triangle. The spectra exhibit two different shapes (red and blue) which are linked to the up and down configuration of the *2×4*. (c) Time trace of the apparent tip height recorded on the *2×4* at the position marked with a star. (b) Time trace of the dI/dV signal of the sensor at the dip position at -5.2 mV. Both time traces show a characteristic two state switching.

This idea was realized with a modified Fe-trimer exhibiting both antiferromagnetic and ferromagnetic coupling, and is prepared to be published by Malavolti *et al.* [MRPY+]. The ferromagnetic coupling is realized by placing one Fe atom of a trimer off the line, the resulting structure is the *sensor*, see **Figure 3.13**. Spin-polarized dI/dV spectra recorded above each atom of the sensor exhibit a complex shape with peaks and dips which originate from processes similar to those previously discussed, see **Figure 3.13**. By applying the rate equation model the numerical dI/dV spectra of each atom are calculated with a

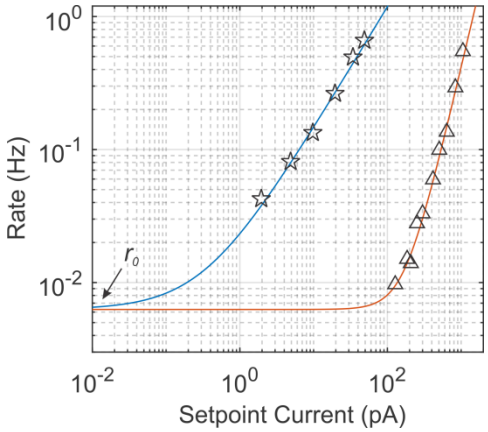

Figure 3.15 observed switching rate of the *2×4* magnet as function of setpoint current measured with the tip directly above the *2×4* magnet (stars) using a bias voltage of 3 mV and with tip over the sensor using a tunnel junction voltage of −5.2 mV (triangle). Colored lines are fitting curves, which were simultaneously fitted with the same intrinsic switching rate r_0.

single adjusted parameter set. The calculated dI/dV spectra match with the recorded ones remarkably well, showing that the rate equation model captures all relevant processes.

The magnetic object being sensed by the *sensor* is a larger few-atom antiferromagnet built nearby, see **Figure 3.14**a). It consists of eight Fe atoms in a 2×4 arrangement, referred to as the *2×4* magnet. In contrast to the Fe-trimer the two Néel like states (*up* and *down*) of the *2×4* magnet are completely spin compensated. The two states do not have any residual magnetization and do not split under application of an external field. Both Néel states can be distinguished in topographic images recorded in a few seconds; see **Figure 3.14**a). If the SP-tip is parked above an atom in the *2×4* magnet a random switching between the two states can be observed, see **Figure 3.14**d).

Typically, the switching rate is in on the order of tens of seconds and depends strongly on the chosen setpoint current. The larger the current, the faster the switching, see **Figure 3.15**. This observation indicates that switching between the two Néel states is induced by scattering of tunneling electrons. In fact, even for the lowest detectable currents the switching rate does not saturate, and the *2×4* is still strongly perturbed by the tunnel current. This perturbation is strongly reduced if, instead of directly inspecting the *2×4*, the nearby *sensor* is used.

On the *2×4* magnet the switching was observed directly via apparent tip height variations, while on the *sensor* the switching is detected via the dI/dV signal. By carefully recording multiple dI/dV spectra on the protruding atom, the presence of two different spectra is revealed. The most significant difference between the two is the dip strength at −5.2 mV, see **Figure 3.14**b). By recording the dI/dV signal at the dip over a long period of time, the switching events can be recorded. The observed rate is on the order of hundreds of seconds and the two different dI/dV states can be correlated with the two Néel states of the *2×4* magnet. The switching rate measured by the *sensor* is ten to a hundred times lower than the rate measured using direct measurement on the *2×4*. With the use of the sensor at the detection limit a switching rate of 0.008 s^{-1} is observed, see **Figure 3.15**. By comparison, the lowest rate measured directly with the tip over the *2×4* magnet was 0.05 s^{-1}. This reveals that the *2×4* magnet is much less perturbed when the *sensor* is used to detect its magnetic state.

The rate equation model in combination with the recorded dI/dV switching amplitude's allows the strength of the interaction between *sensor* and *2×4* magnet to be estimated. Here, an interaction strength of 0.1 T is found (corresponding to an interaction energy on the order of 100 μeV). This value is in agreement with interaction strengths found by different means [YMB+17] and also similar to the tip interaction strength found in the previous sections. The observed strength suggests that the interaction does not originate from dipole-dipole interaction, which would be on the order of 100 neV for a distance of 1.5 nm [CPRP+17]. In fact, Density-Functional-Theory (DFT) calculation shows that the interaction is caused by a confinement effect of the σ and π orbitals of the Cu_2N substrate [YMB+17].

Another interesting aspect arises from the dependency of the switching rate on setpoint current, see **Figure 3.15**. By fitting the switching rates with a function $r(I) = r_0 + \gamma\, I^{\chi}$ with individual parameters γ and χ and forcing them to the same intrinsic switching rate r_0 an intrinsic rate of $r_0 = (7 \pm 2)\ 10^{-3}\ s^{-1}$ can be extrapolated. Whereas an almost linear dependency is found ($\chi = (0.9 \pm 0.2)$) for the rates measured directly on the *2x4* magnet, an almost quadratic dependency on the setpoint current is found ($\chi = (2.3 \pm 0.2)$) for the rates obtained via the *sensor*. The linear dependence of the direct measurement over the *2×4* mag-

net can be explained in the picture of the rate equation model. The additional switching is dominated by the inelastic tunnel rates between the two Néel states, which are proportional to the tunnel current.

On the other hand, the origin of the quadratic dependence for the senor mediated measurement is not obvious. It is reasonable to assume that the carriers injected through the *sensor*, which diffuse through the substrate are responsible for the induced switching. However, in this case a linear dependence is expected, in absence of other phenomena. A possible explanation for the quadratic behavior could reside in an alteration of the energy distribution of the injected carriers due to inelastic tunnel processes at the *sensor*. This could indeed lead to a switching of the *2×4* magnet induced by multiple electron processes and to the non-linear dependence of the switching rates observed in the experiment.

Chapter 4 En route to femtosecond scanning tunneling microscopy

In the previous chapter the dynamics of few atom magnets were investigated with direct transport measurements. As outlined in the introduction, the dynamics could only be observed because the magnets were located on a decoupling layer which slowed the dynamic to the nanosecond scale. Without being slowed down, the intrinsic dynamics of correlated systems are much faster, even reaching the femtosecond scale. This chapter shows the realization of a new STM instrument which allows pump-probe measures on the femtosecond timescale to be performed. The basis of the new instrument is the coupling of STM with THz laser pulse technology (THz-STM). Before this main part, first a brief overview of the development, motivation and problems of time resolved STM is given.

4.1 STM in the time domain

In complex solid state systems emerging collective behavior leads to a rich variety of phenomena such as high temperature superconductivity, Mott insulator phases and charge density waves [Dag05, ZA14]. These fascinating effects have been the subject of great research interest for decades, but their underlying mechanisms are still not completely understood. The dynamic properties of these systems are often investigated in the time domain by probing the reaction of the collective state when excited by an external perturbation [Dem15]. The time scale associated with the relaxation of the excitation is on the order of picoseconds [Ave02]. In the last few years it was realized that these phenomena are inhomogeneous on the nanometer scale and that atomic defects play a major role

in their formation [Dag05, BAvdM+11]. Nevertheless, the correlation of dynamics with inhomogeneity and atomic defects is experimentally difficult, due to the need to connect high spatial and temporal resolution. The spatial resolution of optical techniques allowing ultra-fast measurements is conventionally limited to the wavelength used which is typically on the order of hundreds of nanometers. A possible way to overcome this problem is to implement time resolution in the STM which already provides atomic spatial resolution in real space.

However, a real time investigation with the STM is limited by the very small tunnel current used and its stochastic nature i.e. the current is generated by individual electrons and shot noise therefore plays a significant role. Exploring the real time noise for dynamic content is a difficult instrumentational task because of the finite bandwidth of the current amplifiers used in an STM. State-of-the-art investigation of shot noise in STM reaches frequencies up to hundreds of kilohertz (kHz) [BWBB15, BSWB16].

The detection of faster processes can be achieved by giving up real time investigations and using techniques that transfer the temporal information into low frequency components of the tunnel current, such as pump-probe methods. These pump-probe methods are commonly used in optical laser experiments [Dem15, BAvdM+11] and use the following principle. The dynamics of the inspected system are first initialized by a laser pulse (pump) and probed with a second pulse (probe), which arrives at the sample after a tunable delay time t. The mean dynamical response of the system can be extracted by averaging the probe signal over a large number of repetitions. A stroboscopic picture of the sample dynamics is thus obtained by recording the probe signal as function of the delay time t.

Indeed, optical pump-probe techniques have also been realized in connection with an STM by shining laser pulses into the tunnel junction. Prominent examples are the studies of charge carrier dynamics in semiconductors [TYTS10a, YYT+13, YAW+14, TYTS10b]. In these studies the wavelength of the laser pulses is tuned to lie above the band gap, in order to photo-excite charge carriers. By simultaneously applying a small DC voltage a tunnel current that is sensitive to the total number of photo carriers has been recorded as a

function of the delay time between the two laser pulses [TYTS10a, YYT+13, YAW+14, TYTS10b]. However, in order to investigate the dynamics of a system with such a technique, various issues have to be overcome. The main problem of using laser pulses in combination with STM is the heat generated at the tip due to the laser pulses. The induced increase in temperature leads to an expansion of the tip and thus to an increase of the tunnel current, which is already significant at the picosecond timescale [Gra02, GKP+00, GTP00]. To circumvent this effect, modulation schemes that keep the induced heat constant during the entire measurement must be implemented [TYTS10a, TYTS10b].

Moreover, the use of laser pulses for ultrafast STM is usually limited to photo excitations in the optical range. By replacing the laser pulses with pure voltage pulses, which pump the system via an inelastic process and probe via elastic current, more general pump-probe schemes can be realized. Early attempts in this direction were based on photo-switches, which quickly turn voltages on and off at the tunnel junction via laser pulses [WOB+93, NF93, SEF98]. However, the practical implementation of optical switches is problematic because of the huge technical effort required such as the attachment of the switches to the sample or tip. Additionally the unavoidable heat input has a severe impact on low temperature measurements.

These disadvantages can be avoided by using an all-electronic pump-probe approach. Here, short rectangular voltage pulses are generated outside of the experiment and sent through internal wiring to the tunnel junction [LEL+10, PYB+17]. This technique was successfully used for the characterization of dynamic processes in few atom magnets in combination with low temperature spin-polarized STM. The principle of this method is illustrated in **Figure 4.1.** This technique was also used to investigate the lifetime of the first excited state of the Fe-trimer shown in the last chapter [YCB+15a]. The all-electronic pump-probe method is not limited to the investigation of magnetic states and has a more general application. Indeed, it was exploited to characterize the charging dynamics of dopants in semiconductors [RTO+16].

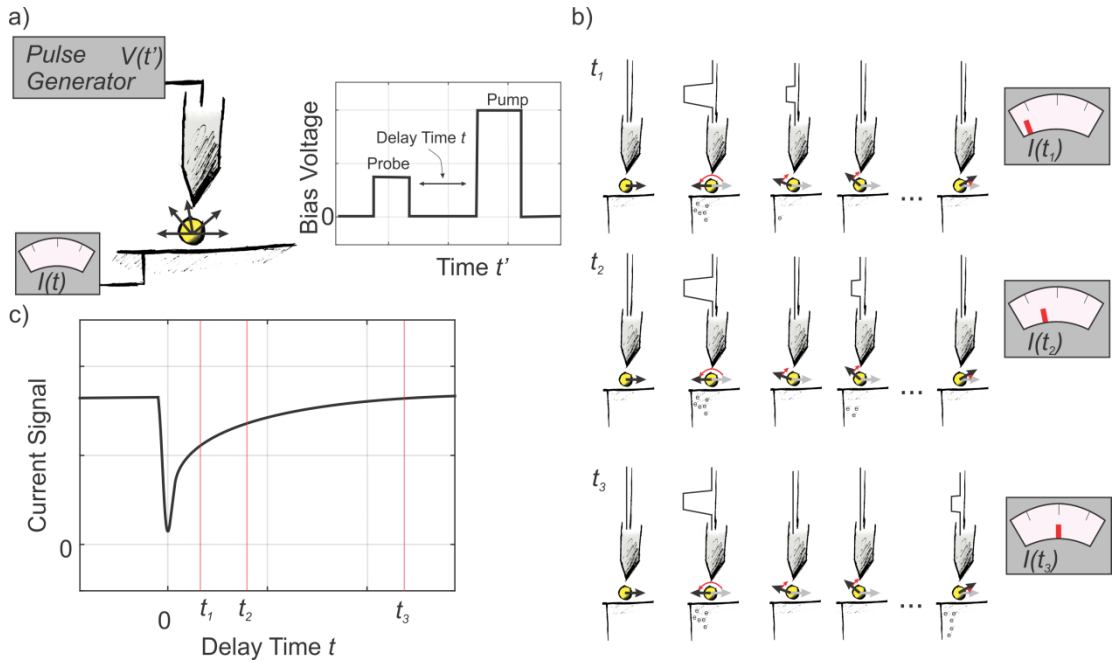

Figure 4.1 Principle of an all-electronic pump-probe measurement with STM. (a) Sketch of the experimental setup. A pulse generator transmits voltage pump-probe pulse pairs to the STM tip. The resulting average tunnel current is recorded as function of the delay t between the pulses. (b) The effect of the voltage pulses pairs is shown for the example of a magnetic atom. The pump pulse flips the magnetization via inelastic scattering. After the excitation the system evolves freely without being disturbed by a tunnel current. When the probe pulse is applied a current flows again. Since the conductance is dependent on the magnetic state, the probe current changes for different pump-probe delays. In total a current is recorded which is the sum of pump current as well as delay-dependent probe current. (c) Sketch of the recorded net current as a function of pump-probe delay which reflects the dynamics of the probed system.

One of the main limitations of this approach is related to the quality of the cables used to transmit the voltage pulses. During the transmission, phenomena like attenuation, reflections and resonances disturb the voltage pulses. These effects can be described in a transfer function that maps the input voltage signal to the output signal at the tip. A time resolution of around one to ten nanoseconds can be achieved by equipping a commercial low temperature STM with high quality radio frequency (RF) cabling. Any further improvement of the transfer function obtained by designing a specific high-frequency transmission line exhibits a diminishing enhancement of the time resolution of this technique [SBPM13]. Instead of improving the cabling, another promising avenue is to apply shaped

voltage pulses, based on the transfer function of the specific instrument, that transform to rectangular pulses at the junction [GEKK13]. This technique can in principle be applied to an existing instrument without the necessity of rebuilding it. Taking the full transfer function, i.e. amplitude attenuation and phase variations, into consideration the all-electronic pump-probe technique can be tuned to investigate dynamics in the 100 ps regime [McM17]. Considering that the most modern high frequency electronic devices are already limited to bandwidths corresponding to tens of picoseconds, it seems to be a long way from achieving temporal resolutions in the intrinsic time scale of electronic excitation in correlated systems (hundreds of femtoseconds) with an STM.

These obstacles can be overcome with an innovative approach based on using free space THz-pulses to generate picosecond voltage pulses in the tunnel junction. The first successful realization of this idea was reported by the research group of Freeman/Hegmann using an ambient condition STM [CJG+13]. Recently, by using an ultra-high vacuum and low temperature STM the oscillation of a single molecule in the tunnel junction was observed [CPYR16]. Other groups focused on tuning the shape of THz-pulses coupled into the STM by changing their carrier-envelope phase [YKM+16]. Further studies on this subject show that the *I(V)* characteristic probed by the induced THz-voltage can be quite different from the one observed with a static voltage [JIN+17]. Starting from these findings, in the next section the realization of a new STM is presented that will allow the study of correlated systems with sub-picosecond time resolution.

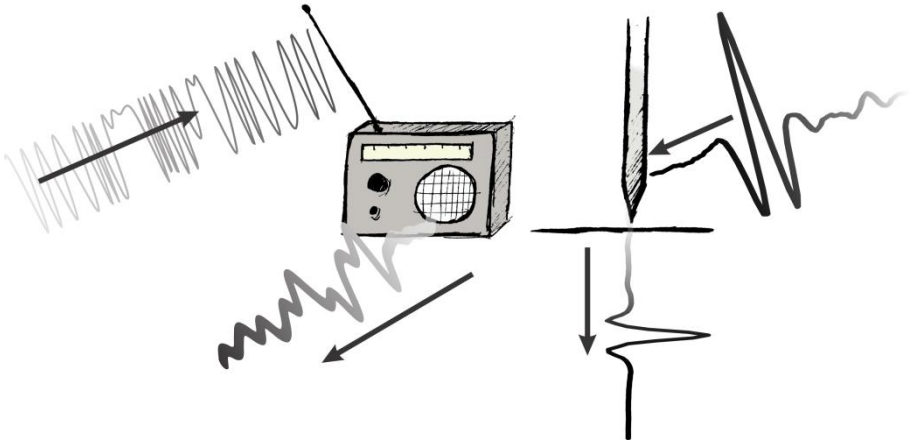

Figure 4.2 A sketch of the THz-STM idea. Like a radio which receives radio-frequency radiation and transforms it to an audio wave the idea is to use the STM tip as a receiver for pulsed THz radiation which becomes rectified in the tunnel junction and is output as a low-frequency current signal.

4.2 The THz-STM concept

In the last decade, boosted by developments in the field of THz light pulses a new approach to ultra-fast pump-probe measurements with the STM became accessible. This idea has similarities to the working principle of an ordinary radio in which an antenna receives a signal from free space MHz radiation, which is rectified by a non-linear device, see **Figure 4.2**. In the new approach, free space THz-pulses induce fast voltage pulses in the STM tip which are rectified in the tunnel junction. A typical THz-pulse in the framework of this thesis consists of a single cycle of an electromagnetic wave pulse with a center frequency between 0.5 THz - 1 THz. The central feature therefore has a width of less than one picosecond. The wavelength of 1 THz is 300 μm and the photon energy is 4 meV. The induced voltage evolution corresponds to the electric field shape of the THz-pulse [JIN+17]. In contrast to the all-electronic pump-probe technique this new method does not require the transmission of high frequency signals through the cabling since the voltage is generated directly at the tip apex.

The mechanism of free space THz-pulses coupling into an STM tip and the voltage they induce at the tunnel junction can be approached from different perspectives. One starting point is the coupling of THz laser pulses to thin metallic wires. This coupling and the

propagation of the pulses in the wire were the subject of various studies [WCL+05, JZG05]. It was found that the problem can be treated with Maxwell-equations in a classical picture. In this picture the coupled THz-pulse launches a surface plasmon polariton (SPP) which propagates almost without dispersion and loss along the wire and therefore retains its shape.

The effective coupling requires a THz polarization parallel to the wire and an *input coupler* at which the initial free space THz-pulse can scatter. Such an input coupler can be realized in different ways, for example by an extra wire or a grating or grooves engraved in the wire surface [DWEM06, CN05]. In contrast to a bare wire, in the case of coupling to a sharp tip an input coupler for the THz radiation is naturally provided by the apex itself. Another important implication of the tip geometry is the field enhancement of the coupled THz-pulse at the apex [WHS+14]. In STM experiments the enhanced electric field will be further altered in the junction by the close vicinity of the metallic sample surface [BR08]. The complex interplay of geometry, material and electromagnetics is not completely resolved yet and is still, to date, being investigated (theoretically as well as experimentally). Nevertheless, it is essential to note that in the tunnel junction geometry the free space THz field will be enhanced by four to five orders of magnitude and will create tunnel voltages of up to several volts [CJG+13, JIN+17, YKM+16].

The coupling properties imply that voltage pulses generated by the THz laser pulses have no DC component, since the mean electric field of the free space THz-pulse is zero. If the tunnel junction has an *ohmic* character this means that the induced voltage can only generate pure AC currents with THz frequencies. Unfortunately AC currents of this high frequency are not experimentally detectable, because of the limited electronic bandwidth of the instrument. However, most of the systems which are of interest do not behave *ohmically*, they have a non-linear *I(V)*, which leads to rectification of the voltage. The rectified current has low frequency components which are detectable in a conventional STM setup.

The properties of the coupling of THz radiation in the STM tip can be summarized as follows:

- Polarization of the THz field $\vec{E}(t')$ needs to be parallel to the tip.
- The THz field generates a localized surface plasmon polariton (SPP) at the tip apex.
- This results in a transient voltage *V(t')* across the tunnel junction, which in good approximation is proportional to the electric field: $V(t') = \alpha\, E(t')$
- The enhancement factor α can reach magnitudes corresponding to a field enhancement of 10.000-100.000 in the tunnel junction.
- The sensed signal is the rectified current resulting from the non-linear tunnel junction.

The first experiments based on the THz-STM idea were already achieved in the last few years, and showed fascinating results [CJG+13, CPYR16, JIN+17, YKM+16]. However, in all of these attempts the very small duty-cycle of the THz pulse train was a disadvantage due to the low repetition rate of the laser source. If a 1 ps wide voltage pulse with 100 mV is applied at a 1 MΩ tunnel junction, none or only one electron is transferred during most of the pulses, resulting in an average electron rectification per pulse smaller than one. In order to detect this small charge flow many pulses have to be averaged. In these first attempts, on the order of 100.000 pulses per second (100 kHz) were typically averaged resulting in a current on the order of 10 fA. This value is at the edge of the detection limit of state-of-the-art STM experiments. Moreover, the dynamic information is encoded in small variations of this tiny current, which results in some restrictions that have to be carefully taken into account during the design of the experiment. These limitations can be overcome, in a general manner, by designing a new THz-pulse source with a drastically increased number of pulses per second.

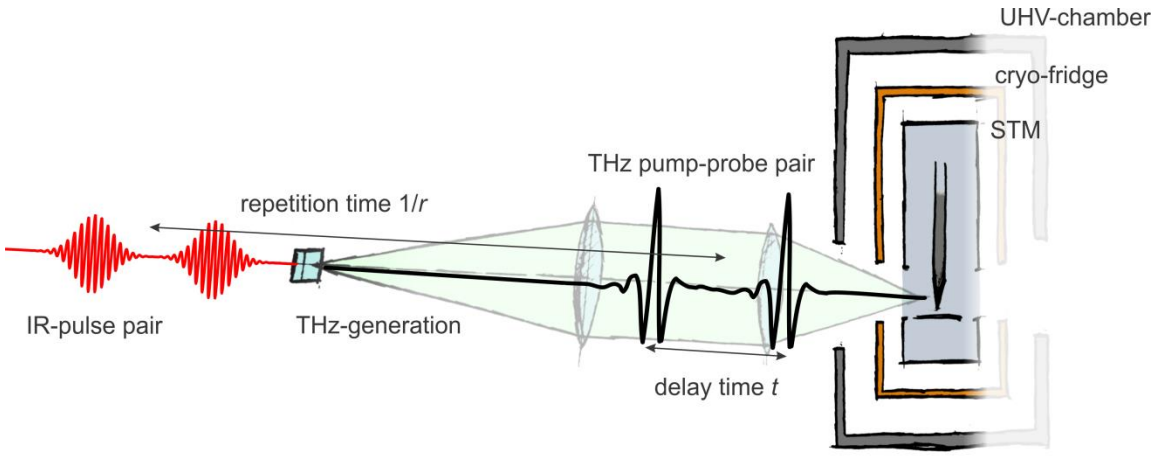

Figure 4.3 Schematic of the new THz-STM design. Two time-delayed infrared (IR) laser pulse pairs generate two delayed THz-pulses via optical rectification with a high repetition rate, which are focused into the STM. The STM is placed in a UHV-chamber inside a low temperature environment. The THz-pulses have access to the tunnel junction via viewports in the chamber and holes in the radiation shielding as well as the STM body itself.

On this basis, a novel THz-STM was developed from the ground up. It allows the characterization of complex matter with femtosecond time and atomic real space resolution and the comprehensive exploration of parameters such as pump-amplitude or tunnel setpoint. The envisioned measurements demand fast pulse repetition rates as well as a high mechanical stability of the STM. The new THz-STM has been designed to perform pump-probe spectroscopy with a repetition rate of 40 MHz and to detect rectified currents on the order of tens of femtoamperes. These properties in combination with ultra-high vacuum (UHV) and low temperature (15 K) conditions are the key to being able to investigate the femtosecond dynamics of complex materials at the atomic scale.

The design of the new THz-STM is based on two concepts:

- A stable STM design that provides such good optical access that focusing with a relative aperture of $N_r = 1$ at the STM tip is possible with all optics placed *ex-situ* (outside of the UHV chamber).
- A versatile and efficient THz source. The source should allow for the generation of THz-pulses with a large repetition rate for pump-probe measurements but also powerful enough that the generated THz-pulses can induce field emission at the tip and are therefore much easier to detect.

These two concepts are realized by a home built STM located in a slim UHV chamber and a THz generation scheme based on optical rectification, see **Figure 4.3**. After explaining the optical part of the THz-STM, the home built STM itself is shown. At the end of this chapter the recorded THz-pulse-pulse correlation function in the new THz-STM is presented.

4.3 Optical setup for THz-Generation

The purpose of the optical setup is the generation of free space THz-laser pulse trains and the focusing thereof on the STM tip. The source was especially designed for highly efficient generation of THz pulses with a variable repetition rate ranging from 500 kHz to 40 MHz. The THz-pulses will be produced via optical rectification of a short near-infra-red (NIR) laser pulse with the tilted pulse front method [HSA+04]. The scheme

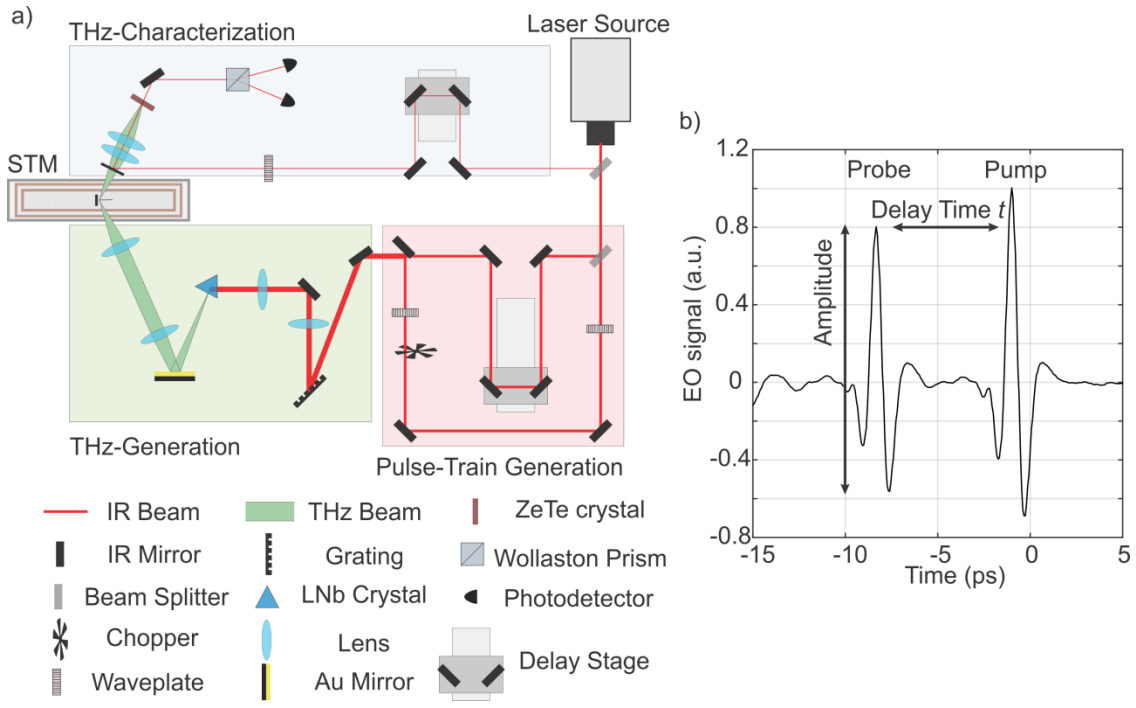

Figure 4.4. (a) Schematic representation of the optical path for the generation of THz pump-probe trains and the focusing thereof into the THz-STM. The optical path is divided into four sections: Laser source, pulse-train generation, THz-generation and THz-characterization. (b) Sketch of the THz pump-probe trains achieved with the setup. The delay between the two pulses and their amplitudes can both be tuned.

of the developed optical setup is shown in Figure 4.4 and can be divided into four different sections. After a short introduction of the different sections, the generation of THz pump-probe trains will be explained in further detail.

The setup starts with a commercial laser system from *Amplitude Systems.* This laser system is capable of producing short near-infra-red (NIR) pulses with a central wavelength of 1030 µm and variable pulse durations between 250 fs and a few picoseconds. An important characteristic of the laser system is the output of NIR-pulses with different repetition rates ranging from 500 kHz to 40 MHz, with a constant mean optical power of 20 W. This feature proves to be crucial in order to place the tip at the THz focus.

The beam is steered from the laser into the *pulse-train-generation* section. Here, the single NIR-pulses are transformed into pump-probe pulse trains. Such trains consist of two NIR-pulses separated by a defined delay time t. In addition to the delay, the pulse modulation is also implemented in this section, which is necessary for Lock-In detection of the pump-probe signal.

After the *pulse-train-generation* section the NIR beam is guided into the *THz-generation* section. In the *THz-generation* section the NIR beam pulse front is tilted with an optical grating and projected into a Lithium Niobate (LNb) crystal. Inside the crystal the NIR-pulses generate the THz-pulses via optical rectification. The THz-pulses leaving the crystal are deflected by a gold mirror and finally focused into the STM with a Polymethylpentene (*TPX)* lens pair.

At the sample the THz-pulses are reflected and leave the STM on the opposite side. Then, in the *THz-characterization* section they are recollected and analyzed by different methods. One common method is electro optical-(EO)-sampling [Sae13]. With this technique the time trace of the electrical field of the THz-pulses can be measured directly. Another characterization method is the average THz power measurement using a custom built thermopile detector.

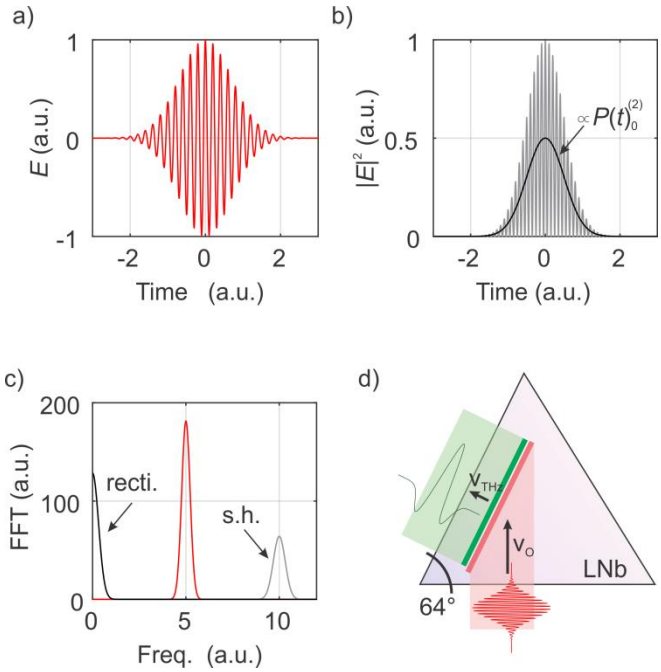

Figure 4.5 Illustration of the working principle of optical rectification with a *tilted pulse front* method in a LNb crystal. The electric field *E(t')* of a laser pulse (red line in a) induces a polarization in the non-linear crystal proportional to $|E(t')|^2$ (grey curve in b). (c) This induced polarization will have frequency components at double the frequency of the laser pulse (second harmonic) and at zero frequency (rectification). The rectified part of the polarization (black curve in b) is the source of THz radiation. To make this process efficient, the generated THz and the IR-pulse should propagate with the same velocity through the non-linear crystal. Since this matching is not obtained naturally in LNb crystals, it is indirectly achieved by tilting the pulse front of the IR-pulse (d).

4.3.1 THz-Generation

The frequency band ranging from 0.3 THz up to 3 THz connects the two different worlds of microwave and infrared radiation. This frequency window is also known as the THz-gap because, in the past, it was experimentally difficult to produce and to detect electromagnetic waves in this frequency range. Nevertheless, since around a decade ago, advancements in the generation and detection of THz radiation have opened up new possibilities. In the following, the THz generation method used in the setup is presented. The method is based on the optical rectification of a femtosecond NIR-pulse in LNb in combination with a tilted pulse front technique. A more general discussion of generation, detec-

tion and application of THz radiation goes beyond the scope of this thesis and explanations can be explained in great detail in different textbooks [Sae13, Lee09, PP14].

Optical rectification in nonlinear optical crystals is a common technique used to generate ps-THz-pulses. The origin of this process is the inharmonic electro static potential of the free charges inside those crystals. By driving these charges with an external laser field of frequency ω the anharmonicity gives rise to a charge displacement with a frequency of 2 ω (second harmonic generation) and 0 ω (rectification). The displacement of the charges forms a polarization P and, in approximation, the nonlinear polarization $P^{(2)}(t')$ is proportional to the absolute square of the electric field $E(t')$ of the laser light:

$$P^{(2)}(t') \propto |E(t')|^2. \tag{4.1}$$

In contrast to a continuous laser field, a pulsed laser field leads to a time-varying rectified second-order polarization $P_0^{(2)}(t')$, as shown in **Figure 4.5**a) and b). The varying rectified second-order polarization $P_0^{(2)}(t')$ has frequency components up to the order of the inverse pulse duration, **Figure 4.5**c), and its second time derivative $\frac{\mathrm{d}^2 P_0^{(2)}}{\mathrm{d}t^2}$ is the origin of an electromagnetic wave in the THz range. In the example of a 200 fs NIR-pulse, radiation with frequencies of up to 5 THz can be generated by rectification. In general, to connect $\vec{P}_0^{(2)}(t')$ and $\vec{E}(t)$, the second-order nonlinear susceptibility tensor $\chi_{ijk}^{(2)}$ of the crystal is necessary. The larger the susceptibility the more efficient the rectification process is.

A further aspect to take into account for efficient THz-generation is the movement of the polarization $\vec{P}_0^{(2)}(t', \vec{r})$, which travels with the NIR-pulse through the crystal with its group velocity v_o. During the passage the varying polarization generates THz waves which propagate with the THz phase velocity v_{THz}. If the THz phase velocity v_{THz} and the group velocity v_o of the optical laser pulse match, the generated THz radiation interferes constructively and an efficient THz-pulse is generated. For efficient THz-generation the crystal should therefore exhibit a large second-order nonlinear susceptibility $\chi_{ijk}^{(2)}$ and fulfill the velocity matching condition.

LNb crystals are ideally suited for the generation of strong THz-pulses with NIR-pulses of a wavelength of 1030 nm, but they do not intrinsically fulfill the velocity matching condition. In fact, NIR-pulses travel about 2.26 times faster than THz-pulses in LNb, which prohibits effective THz generation. Nevertheless this problem can be circumvented by tilting the pulse front of the optical pulse. By tilting the NIR-pulse front the group velocity in the THz propagation direction is effectively reduced and the velocity mismatch is resolved by a tilt angle of $\phi \approx 64°$:

$$v_o \cos(\phi) = v_{THz} \;\Rightarrow\; \phi = \cos^{-1}\left(\frac{v_{THz}}{v_o}\right) = \cos^{-1}(2.26) \approx 64°. \qquad 4.2$$

The tilt is realized experimentally with an optical grating and by projecting the NIR-pulse with two lenses from the grating into the crystal, as shown in **Figure 4.5**d). Indeed, this THz generation scheme, based on optical rectification of NIR-pulses in LNb crystal in combination with a tilted pulse front (TPF) technique, is a well-established technique for the production of highly intense THz-pulses [HF11, FPK+12, HYHN07].

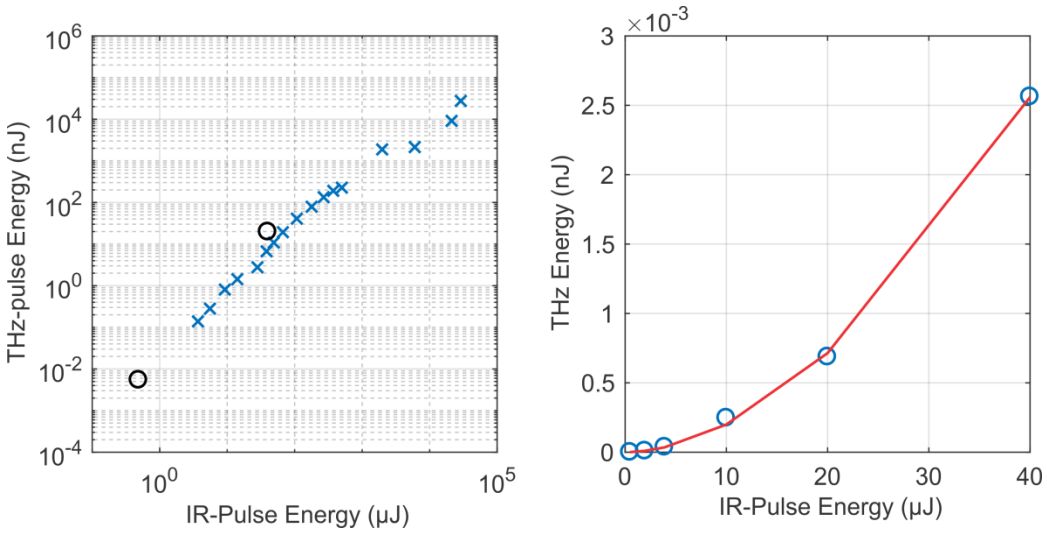

Figure 4.6 (a) measured THz-pulse energy as a function of NIR-pulse energy. The **black open circles** are estimates of the full achieved THz-pulse energies. With a highly sensitive power detector only a fraction of the THz energy was captured since the detection area was much smaller than the THz beam. The full energy was extrapolated based on the additional measured beam dimension. The **blue crosses** are literature values extracted from [HF11]. (b) The fractional THz-pulse energy as function of the NIR-pulse energy was fit using a power law function (red curve). The best fit was achieved with an exponent of 1.8 which is close to the expected quadratic behavior.

The NIR-pulses used in literature for the presented THz-pulse generation technique typically have energies larger then several microjoules (μJ). However, in the presented setup the NIR-pulse energies are smaller which could result in insufficient THz generation. Power measurements were therefore performed to extract the THz generation efficiency for small pulse energies and to compare them with literature values, see **Figure 4.6**. For the completed THz generation setup an efficiency η ranging from $\eta_{\max} = 5 \cdot 10^{-4}$ for 40 μJ NIR-pulses down to $\eta_{\min} = 1 \cdot 10^{-5}$ for 0.5 μJ NIR-pulses was found. Furthermore, the NIR-pulse energy dependence of $\eta(u_{IR})$ can be approximated by $\eta(u_{IR}) = \frac{u_{THz}}{u_{IR}} = u_{IR} \cdot 15\frac{1}{\mathrm{J}}$ since the THz-pulse energy u_{THz} depends almost ideally quadratically on the NIR-pulse energy u_{IR}, see **Figure 4.6**. These results matches with THz generation efficiencies reported in literature [HF11].

In the final setup, the generated THz-pulses are deflected with an Au-mirror and focused with two *TPX* lens into the STM. The size of THz focus at the tip positon was estimated in

a preliminary setup since the geometric constrictions of the STM and the UHV chamber make a direct optical measurement at the final focus impossible. Using a knife edge measurement [HW05] and by assuming a Gaussian beam, a focus diameter of about 2 mm (FWHM) was determined. This is on the same order than the diffraction limited beam diameter 1.2 mm ($d = 2.44\frac{\lambda}{N_r}$) of 0.6 THz radiation considering a relative aperture of $N_r = 1$ [Trä12].

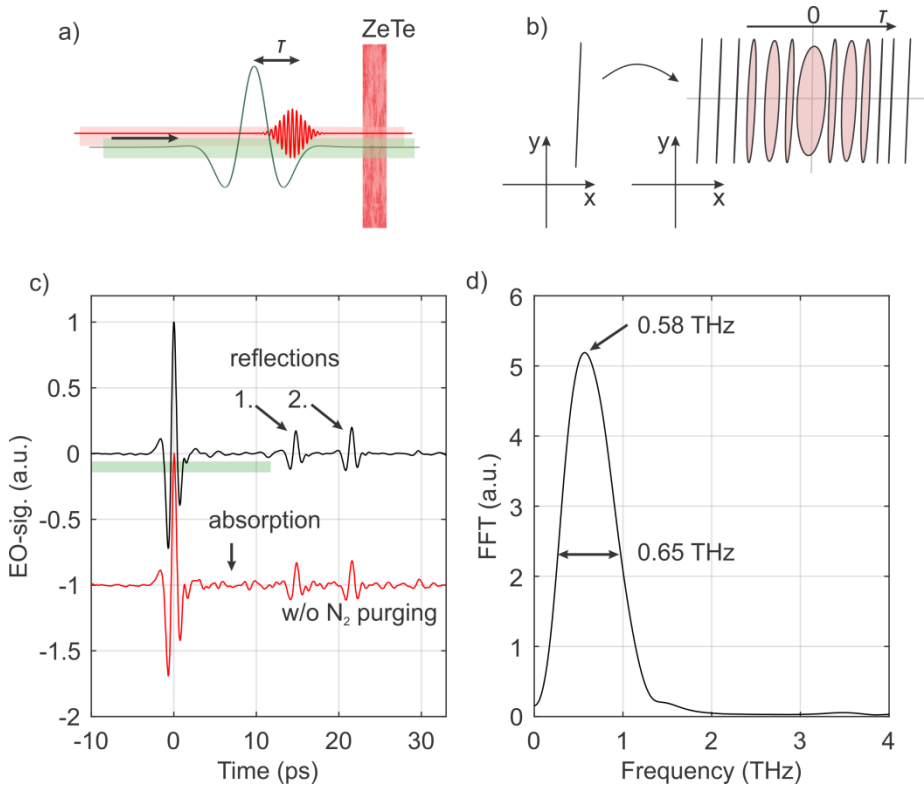

Figure 4.7 (a-b) scheme of the basic principle of EO-sampling. (a) The THz-pulse and a short IR-pulse propagate collinearly through a non-linear crystal (here: ZeTe). Depending on the delay τ the polarization of IR-pulse is modified (b). A linear polarization is transformed into an elliptical one at zero delay. The polarization phase change is proportional to the electric field of the THz-pulse. (c) The resulting EO-signal for the THz-pulses produced in the described setup. The recorded THz-pulse traces exhibit two reflections beside the main peak. Without N_2 purging the influence of THz absorption by water in normal air is visible. (d) The power spectrum of the THz-pulse (based on the EO signal marked with a green bar in (c). The fundamental frequency of the THz-pulse is 0.58 THz and has a spectral width of about 0.65 THz (FWHM).

4.3.2 The THz-pulse shape

In the previous part, the efficiency of the generation and the focus dimensions of the THz-pulses were discussed. In addition to these two parameters, the shape of the generated THz-pulses in the time domain is of particular importance for the interpretation of the envisioned pump-probe experiments. A well-known method for exploring THz-pulses in the time domain is electro-optic-(EO)-sampling [Lee09].

The EO-sampling technique is related to the *Pockels* effect and uses the nonlinear susceptibility of a nonlinear optical crystal, analogous to the generation of THz with optical rectification. In the *Pockels* effect, an externally applied electric field causes birefringence in an optical medium, which leads to a polarization change in laser light passing through it. The polarization change is described by a phase factor $\Delta\varphi$ between the two polarization directions and is proportional to the applied electric field strength E, $\Delta\varphi \propto E$.

For EO-sampling, the electric field of the THz-pulse E_{THz} induces birefringence in the optical crystal (here: ZeTe). This effect of the THz radiation is then sensed by a femtosecond laser pulse passing through the crystal simultaneously and collinearly with it. By changing the time delay between them it is possible to map the effect of the THz-pulse in time, as the THz-pulse is longer than the laser pulse, see **Figure 4.7**a) and b). The signal $EO(t')$ resulting from the polarization change is measured as function of delay time t and represents a good approximation of the electric field profile of the THz-pulse, $EO(t) \sim \Delta\varphi(t) \sim E_{THz}(t)$.

EO-sampling curves, $EO(t)$, of typical THz-pulses generated by the described setup are shown in **Figure 4.7**c). The dominant feature of the curve is the THz peak at zero time delay. To good approximation the main pulse can be described as a single cycle pulse with duration of 2.5 ps. The frequency spectrum of the main peak shows that the central carrier frequency is located at 0.58 THz and that the pulse has a spectral width of approximately 0.65 THz, see **Figure 4.7**d).

Apart from this main feature, two further peaks are observed. These peaks are caused by double reflections of the THz beam at optical components back into the propagation direction. The sources of the reflections were found by comparing their delay times to the main peak and the optical thicknesses of the optical components inside the beam path. The first reflection, located at 15 ps, originates from 1 mm thick quartz windows installed at the inner radiation shield of the THz-STM and could interfere with THz-STM measurements. In contrast, the second reflection has no impact on THz-STM measurements since it results from reflections inside the EO-sampling crystal and is not experienced by the STM tip. Much less pronounced, but nevertheless important, are small oscillatory fea-

tures observed after the main pulse. They are due to absorption of THz light by water vapor in air [vEFG89]. This is a common problem of free space THz beams and was reduced in the presented setup by air-tight encapsulation of the optics and dry nitrogen gas purging.

Based on the measured THz-pulse energy u_{THz}, in combination with the obtained shape of the THz-pulse $EO(t)$ and the size of the focus of the THz-pulses the electric field applied at the STM tip can be estimated:

$$u_{THz} = \varepsilon_0 \, c_0 \, 2\pi \int \mathrm{d}r \, r \, e^{-2\left(\frac{r}{w}\right)^2} \int \mathrm{d}t \;\; |C \cdot EO(t)|^2 \,, \tag{4.3}$$

where ε_0 is the permittivity of the vacuum, c_0 is the speed of light, w is the geometric width of the THz-pulse and C is the conversion factor which converts the measured $EO(t)$ sampling signal to an electric field strength. Based on the power measurement of **Figure 4.6** and on the EO-sampling trace of **Figure 4.7**, peak electric fields of 260 V/cm are estimated for 5.4 pJ THz-pulse energies generated with a repetition rate of 40 MHz and 16 kV/cm for 20 nJ THz-pulses generated at 500 kHz.

4.3.3 Pulse train generation and modulations

Pump-probe experiments require at least two pulses. In previous THz-STM experiments a single THz-pulse was split and recombined in a Michelson-Interferometer to obtain a pump-probe pulse pair [CJG+13, CPYR16, JIN+17, YKM+16]. This method has a major drawback: It requires complicated optical paths for the THz-pulses. In the design of the new instrument, instead of the THz pulses, the single NIR-pulses are transformed to pulse pairs with different delays, amplitudes and modulation. The NIR-pulse-train generates the THz-pulse pairs which are then directly focused into the STM without any further treatment. It is worth noting that both approaches theoretically transform a single NIR pulse equally in two identical THz-pulses. However, the NIR-pulse-split approach is highly beneficial since standard NIR optics can be used which, in contrast to THz optics, have a higher quality and are easier to adjust.

As for all pump-probe techniques, it is crucial that the pulses do not change for different delay times since this would result in artificial signals. The verification of this is of special importance here, since the two THz-pulses are generated in the same crystal and this could cause a correlation effect. With EO-sampling it was verified that generation of the two THz-pulses is independent of delay times, see **Figure 4.8**a).

In the *pulse-train-generation* section a beam-splitter divides the IR beam into two separate paths. The beams are treated individually and are recombined just before leaving the section. The recombination is realized by steering one beam closely alongside the edge of a mirror. The second beam is deflected by the same mirror such that both beams are traveling almost collinearly after it, see **Figure 4.4**. In general the section has three main tasks:

1. Control of the delay time *t*
2. Control of the pulse amplitude
3. Implementation of modulation for Lock-In detection

In order to control the delay time *t* between the two NIR-pulses, one path is equipped

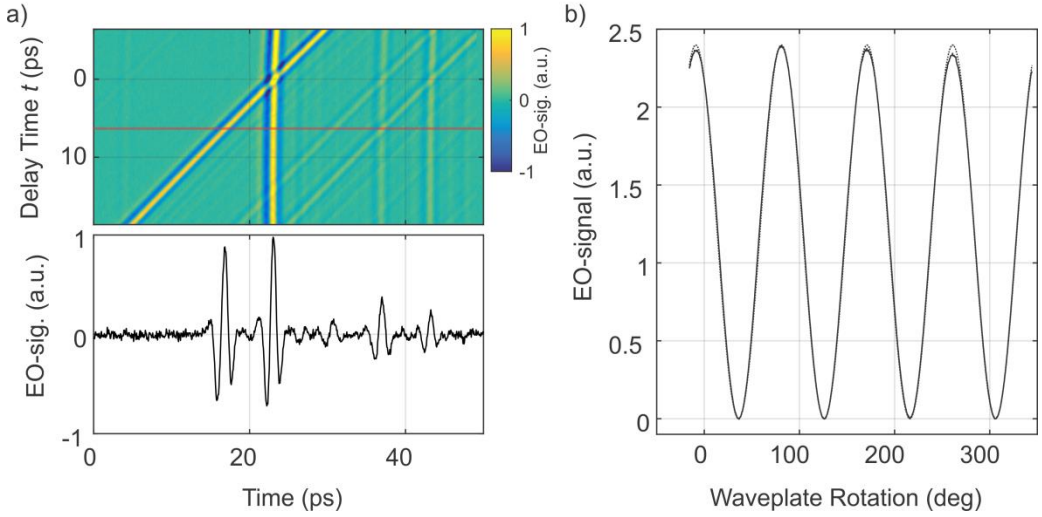

Figure 4.8 (a) EO-sampling measurement of the whole pump-probe pulse train as function of delay between the two THz-pulses in a 2D false color plot. The measurement reveals that the two THz-pulses are generated independently. In the lower panel a single EO-trace at the pump-probe delay marked with the red line. (b) Peak EO-signal of the *probe* THz-pulse as a function of the waveplate rotation angle (solid line) and fit of equation 4.4 to the recorded data (dotted line).

with a linear delay stage. The pulse travelling along this path is called *pump* pulse while the other is the *probe* pulse. The linear stage changes the path length of the *pump* pulse, and can position it before or after the *probe* pulse.

Besides controlling the delay time between the two THz-pulses, the adjustment of their amplitudes is necessary in order to enable comprehensive measurements. The THz-pulse amplitudes can be adjusted with different techniques. In this setup the polarization dependence of the THz generation is taken advantage of. The efficiency of the THz generation is tuned by rotating the polarization of the NIR-pulses with a $\lambda/2$ waveplate, since the optical rectification in the LNb as well as the reflection at the grating is polarization dependent. This approach keeps the power of the IR beam directed into the *THz-generation* section constant. This is important since IR stray light affecting the heat input on the STM cannot be completely prevented and should, at least, be kept constant.

The dependence of the THz generation on the rotation angle of the waveplate is explored experimentally. The EO-sampling signal of the THz-pulse was therefore recorded as a function of the rotation of the waveplate at a fixed time delay; see **Figure 4.8**b). Based on this measurement, the THz generation efficiency of the probe pulse is calibrated. The observed dependence of the EO-sampling signal on the rotation angle can be modeled as follows:

$$EO(t_{fix}, \varphi) = A(t_{fix}) \cos^2\left(\frac{\pi}{90}\,(\varphi - \varphi_0)\right). \qquad 4.4$$

The shift φ_0 corresponds to the rotation angle of the waveplate at which a maximal THz generation is achieved. The shift φ_0 can also found in the tunnel experiment by maximizing the THz induced current as function of the waveplate angle of rotation.

In addition to tuning the delay and pulse amplitudes, the modulation for Lock-In detection is also implemented in the *pulse-train-generation* section. Similar to differential conductance (dI/dV) spectra, see section 2.2, the THz signal is shifted to a frequency range with a lower noise floor with Lock-In detection, resulting in a better signal-to-noise ratio. For pump-probe experiment the modulation is especially important since only the delay

time dependent correlation current $I_{\mathrm{corr}}(t)$ is of interest. The meaning of $I_{\mathrm{corr}}(t)$ becomes clearer by considering the total tunnel current $I_{THz}(t)$ induced by the two THz-pulses:

$$I_{THz}(t) = I_{\mathrm{Pump}} + I_{\mathrm{Probe}} + I_{\mathrm{corr}}(t). \tag{4.5}$$

Here I_{Pump} and I_{Probe} are the current contributions of the pump and probe pulse independent of the delay time t. Typically in a pump-probe measurement, one would ideally directly modulate the correlation current $I_{\mathrm{corr}}(t)$ at the Lock-In frequency, since only $I_{\mathrm{corr}}(t)$ is of interest. Experimentally, the realization of such modulation is rather difficult. In practice a simpler modulation is realized by a chopping wheel that turns the probe pulse on-and-off at the Lock-In frequency and results in a measured Lock-In signal proportional to the sum $I_{\mathrm{Probe}} + I_{\mathrm{corr}}(t)$.

Nevertheless there are theoretical possibilities to modulate just the correlated current $I_{\mathrm{corr}}(t)$. For example, if the delay time t is directly modulated, whether by switching between the measured delay time t and a large delay time t_∞ at which the correlated current is zero $I_{\mathrm{corr}}(t_\infty) = 0$ or by adding a small oscillating delay time Δt. In the first case the measured Lock-In signal corresponds directly to $I_{\mathrm{corr}}(t)$, while in the second case the Lock-In signal corresponds to first order to $\frac{\mathrm{d}I_{\mathrm{corr}}}{\mathrm{d}t}(t)$. The disadvantage of these methods is the experimental effort required since the modulation of t means altering the length of the beam path at the Lock-In frequency.

Yet another method to modulate only $I_{\mathrm{corr}}(t)$, that does not rely on changing the beam path, exploits the fact that the correlation current $I_{\mathrm{corr}}(t)$ is only part of the current if both pump and probe are present. Turning the probe on-and-off as well as the pump pulse with slightly different frequencies will result in a signal at the difference frequency which is exclusively proportional to the correlation current $I_{\mathrm{corr}}(t)$. However, the achievable signal contribution at the Lock-In frequency is only a fraction of the full correlation current $I_{\mathrm{corr}}(t)$ and therefore the simpler on-off modulation scheme was used in the final setup.

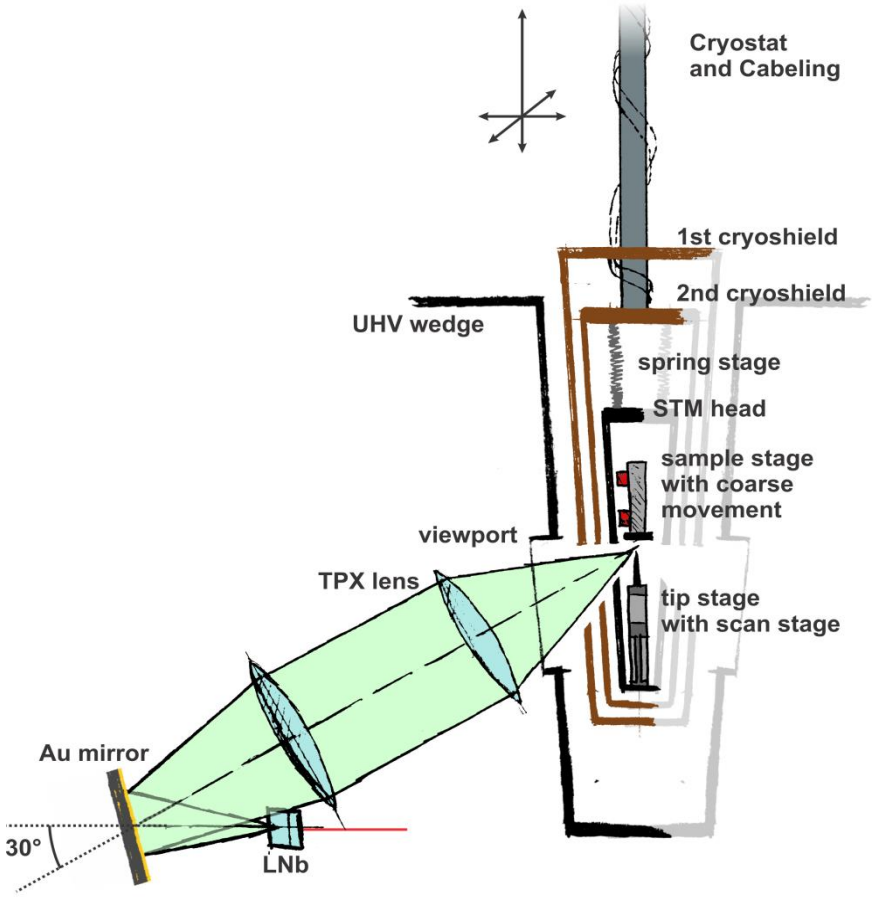

Figure 4.9 Schematic side cut through the THz-STM including the last section of the optical path. The STM is attached to a flow cryostat and is placed inside of a wedge shaped UHV chamber. The STM head itself is surrounded by radiation shields. Optical access is provided by two viewports and holes inside the shields and the STM body.

4.4 The wedged scanning tunneling microscope

The previous part of this chapter described the optical setup developed for the THz-STM setup. The setup is able to efficiently generate THz pump-probe pulse trains by optical rectification. The THz-pulse train has a repetition rate of up to 40 MHz with electric field strength of 130 V/cm for each pulse of the pulse train in the beam focus. The focus of the THz beam will be located at the tip of an STM allowing for femtosecond electronic pump-probe experiments with atomic resolution. Although the properties of the generated THz-pulse train perfectly match the requirements they are just the first compo-

nent necessary in order to perform high quality measurements. The second component is the STM which has to fulfill specific restrictions in light of the desired experiments:

- UHV conditions are necessary to prevent surface contamination.
- Variable low temperatures between 10 K and room temperature at the sample are crucial to tune complex materials across their phase transitions.
- A high mechanical stability at the tunnel junction of the order of picometers is needed to be able to detect small current signals.
- Coarse positioning is needed to investigate different areas of the sample surface.
- Reliable exchange of sample and tip must be possible without breaking the UHV (*in-situ*).

In addition to the requirements resulting from the sample systems, further design considerations arise from the alignment of THz beam onto the tip. The complexity of this very difficult problem is reduced if:

- All optical components are placed outside of the UHV camber (*ex-situ*) and are easy accessible, if an optical realignment is necessary.
- An optical access exists that allows the focusing of a 5 cm diameter THz beam with a relative aperture of $N_r = 1$ directly onto the STM tip by which a small focus and large electric fields can be achieved.
- A variable positioning of the tunnel junction in a 10×10×10 mm^3 volume with micrometer precision is possible in order to place the STM tip in the center of the THz focus without changing the optical path.

All these listed requirements are met by the new STM sketched in **Figure 4.9**. A short summary of the realized STM design is given in the following.

The core of the STM is the head inside which the tip and sample are located. The tip is connected to the scan stage which allows fine scan movement in three dimensions. The sample stage is placed onto a coarse motor which approaches the sample to the tip. The STM head is mounted to the base of a flow cryostat by a vibration-isolation-stage consisting of springs and eddy current damping. The cryostat provides cooling for low tempera-

ture operation and allows a variable sample temperature from 15 K to room temperature. The STM head is encapsulated by two radiation shields to reduce the effect of heat radiation.

Including the radiation shields, the STM fits into a slim wedged UHV chamber that can be placed inside of the optical setup. Two viewports in the wedge as well as holes in the shields and the STM head allow for optical access to the tunnel junction. The size and position of the holes yield a possible optical access of around one relative aperture. The angle between the optical path and the tip axis is 30° in order to prohibit any masking effect by the sample and to focus the full beam on the tip. This design allows the focusing and/or collecting THz optics to be placed close to the tunnel junction, but outside the UHV chamber. While one viewport can be used to couple light into the junction the other one can be used to collect the reflected light. It is also possible to use both viewports as inputs to shine in laser light from different sources.

The STM has two specific positions inside the UHV chamber: one is the *measurement* position and the other the *exchange* position which allows for sample and tip exchange. In **Figure 4.9**, the STM is in the *measurement* position, which does not allow exchange of the tip or of the sample. To bring it into the *exchange* position the STM has to be lifted. The flow cryostat is therefore equipped with an *XYZ*-manipulator. Apart from lifting the STM for tip and sample exchange a crucial task of the *XYZ*-manipulator is to align the tip and place it exactly in the THz-focus.

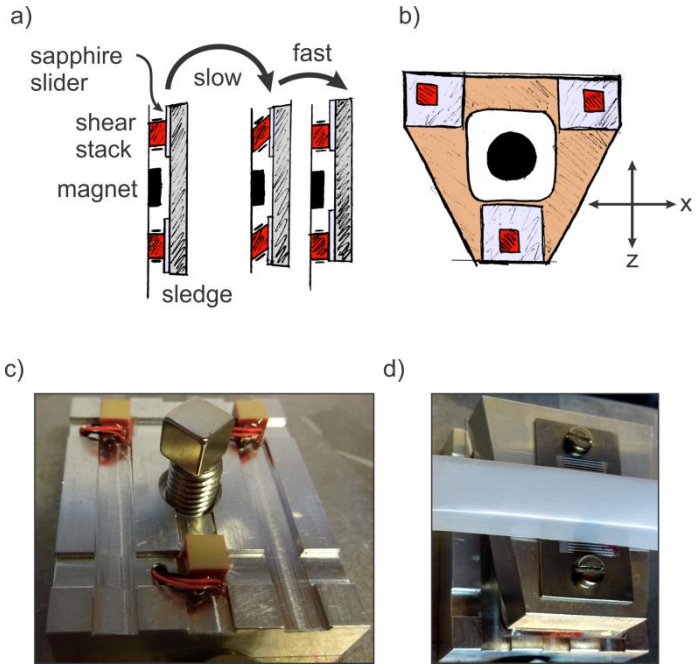

Figure 4.10 (a) The slip-stick moving principle of the coarse motor. A sled is clamped magnetically on piezo shear stacks. Repeated slow and fast shear motions of the shear stacks in the desired direction will move the sled. b) The use of three shear stacks in a triangular arrangement with the magnet in the center ensures mechanical stability. Two axis shear stacks are used to move the sled up/down (*z*-axis) or left/right (*x*-axis). (c-d) Photographs of the prototype of the THz-STM coarse motor. (c) The three shear stacks responsible for the movement are glued to a base plate and the magnet clamping the sled is attached to a screw. The distance between magnet and the sled and therefore the acting magnetic force is controlled with the screw. The motion of the sled was measured via markers attached to the sled (b).

4.4.1 The coarse movement motor

The slim design is an essential element of the new THz-STM. In fact, the UHV wedge has a cross-section of less than 8 cm at the position of the viewports, while the STM head itself has a mean cross-section of about 2.5 cm. This slim STM-head design in combination with a high mechanical stability was only achievable with a newly developed coarse movement motor. The motor is constructed with piezo shear stacks and a sled clamped on top of them, see **Figure 4.10**. The clamping force holding the sled in place is applied by a magnet. The use of a magnet is advantageous when compared to the use of springs because the magnetic force is always perpendicular to the motion axes. The mag-

net is fixed between the shear stacks such that the clamping force is acting on the center of the sled and a high stability is achieved

The operation principle of the motor is the slip stick (or inertia drive) method commonly used in piezo motors [Che08, Voi15], illustrated in **Figure 4.10**. In this technique the shear stacks are first deflected slowly (~1 ms) and then pulled back rapidly (<1 µs). During the slow movement the sled sticks to the shear stacks and slips during the fast pull back. A reproducible movement of the motor is ensured by polished sapphire plates glued to the sled on which the shear stacks slide.

A triangular arrangement of the shear stacks with the magnet in the center yields a high mechanical stability of the motor. Horizontal movement is achieved by adjusting the magnetic force to be much larger than the weight of the sled. However, the magnetic force has to be adjusted in a way that it does not lead to friction larger than the maximum applicable shear force at the shear stacks. In practice a magnetic force on the order of 10 N is sufficient for reliable movement of the sled which had a weight of about 60 g including the sample stage. Two axis shear stacks (P-122.05 from *PIceramics*) were chosen to allow

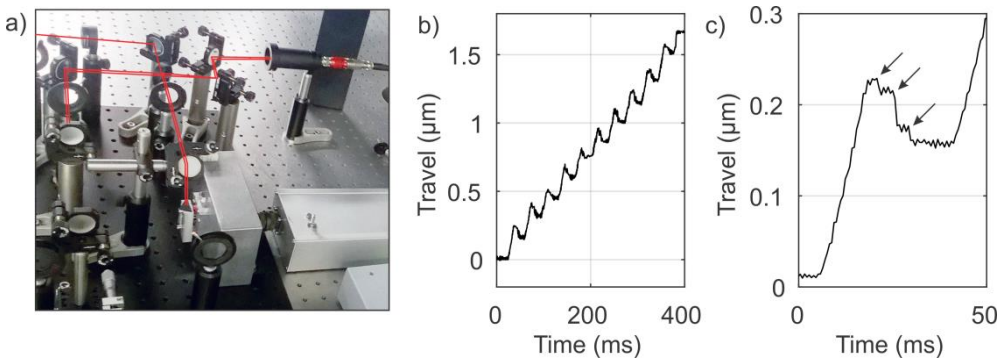

Figure 4.11 (a) Photograph of the Michaelson interferometer test. In this test single slip-stick steps were resolved by placing the motor as a mirror element of one of the two interferometer arms. The red lines show the beam path. (c) Slip-stick steps recorded as a function of time. Here, voltage ramps of about 200 V were applied to the shear stack to move the sled. Since the electronics used during the testing phase were not able to produce a steep enough voltage edge to allow all three shear stacks to slip together, the shear stacks were slipped sequentially. (d) The sequential slipping of the three shear stack is observable in the backslash if the recorded steps are averaged; arrows indicate the three slip occurrences.

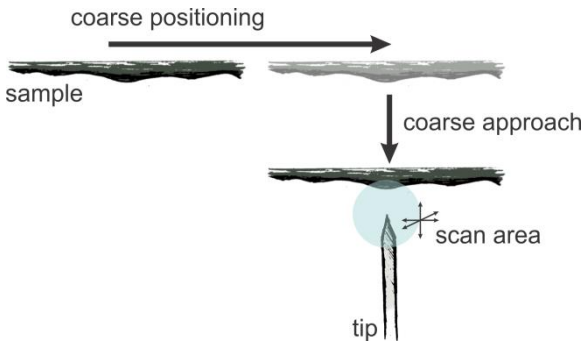

Figure 4.12 Schematic of possible movements in the STM. The sample is fixed on the coarse motor which is responsible for positioning the tip at the area of interest and bringing the tip and sample into the scan range of the scan-stage. In scan range the tip can be moved with the scan-stage attached to the tip into tunnel contact and scan the surface.

not only horizontal up/down (z-axis) and vertical left/right (x-axis) movement as well.

Before implementing the coarse movement motor in the STM head, a prototype was built and tested. Primarily, the tests had to measure the smallest reliable individual step that the motor is capable of. Only if the smallest steps are on the order of hundred nanometers will the motor be able to move the sample into tunnel range without crashing it into the STM tip, as the scan range of the STM tip is limited. In the test phase, it was further verified whether the motor moves/ slips in the wrong direction at the beginning of a step. These undesirable movements could cause crashes of the tip onto the sample, during, for example, the withdrawal of the tip from the surface. All these aspects were tested by placing the motor-prototype in a Michelson laser interferometer setup (laser wavelength $\lambda = 632$ nm) in which the displacements were directly resolved; see **Figure 4.11**. In addition to the Michelson interferometer test the prototype was also tested in vacuum. Here, the walker's capability to bring a sample and a tip safely (without crashing) in and out of tunneling region was examined.

This new coarse mover design provides a suitable platform for the sample to be stably held in front of the STM tip. The micrometer coarse movement of the motor, with a working range of 10 mm, allows the tip to be positioned at different parts of the sample. After bringing the area of interest into the scan range of the scan-stage, the motor is turned off.

The fine approach and the scan movement during STM operation is then performed by a scan stage which holds the tip, while the sample is fixed, see **Figure 4.12**.

4.4.2 Sample- and tip-stage

The sample is not permanently linked to the motor but can be exchanged reliably without disassembling the STM or breaking the UHV. The sample is fixed to a sample holder which can be placed on and removed from the motor. This functionality is provided by a simple plate design of the sample holder and a corresponding receptacle on the

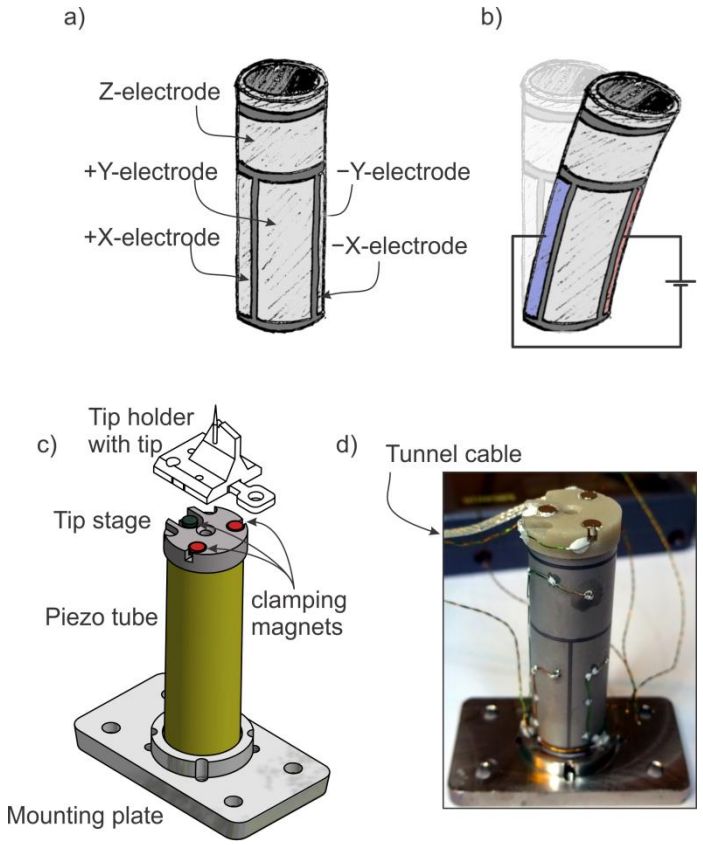

Figure 4.13 (a) The scanning piezo tube features several electrodes for the different scan directions. (b) XY scanning is realized by bending the piezo tube by applying opposing voltages at two facing electrodes. (c) To connect the scan piezo to the STM head it is glued on a mounting plate. The tip stage is glued on the top of the scan piezo. Three magnets clamp a tip holder and provide electrical contact to it. One magnet has an opposite polarization direction with respect to the two other magnets in order to restrict the tip holder to one clamping configuration. (d) Photograph of the assembled scan stage.

motor i.e. the sample stage. A leaf spring clamps the sample into the sample stage, providing mechanical stability and electrical contact through the stage, as both the stage and sample plate are made of metal.

The tip is mounted at the top of the scan stage. The scan stage is made out of a piezoelectric scan tube which is glued between a mounting plate and the tip stage, see **Figure 4.13**. Voltages applied to the electrodes of the piezoelectric tube will deform it according to the arrangement of electrodes inside and outside of the tube. Here, the outside electrode of the tube is separated into four quadrants and two rings while the inside is a single electrode, see **Figure 4.13**. Applying voltages between the four main quadrants will cause a bending of the piezo tube and thereby realize XY scanning. By applying a voltage between the inner and the ring electrode above the four quadrants the tube will expand correspondingly in the Z direction (tip-sample distance). An additional thin ring at the very top of the tube is connected to the inner electrode top and will screen the STM tip from the voltages applied at the piezo. To apply the voltages to the piezo tube three twisted pair cables are soldered to it. One pair is soldered to the $+X$ and $-X$ electrodes, the second pair to the $+Y$ and $-Y$ and the remaining pair is soldered to the Z and to the inner-electrode. At ambient conditions the scan stage provides a total range on the order of ± 7 μm in XY direction and 3 μm in Z direction, at low temperatures the scan-range will be limited to a tenth of these values.

Similar to the sample, the tip is also not permanently fixed but exchangeably connected to the scan stage with a tip holder. The tip-stage, see **Figure 4.13**, clamps and electronically contacts the tip holder with the scan stage. These two functionalities are provided simultaneously by magnets glued in the tip stage, with counterparts at the tip-holder. Three magnets are used to span a unique plane for stable mounting of the tip holder. The three magnets correspond to three accessible electrical contacts. The tunnel current is measured through one contact, while the two other contacts allow the instrument to function as an atomic force microscope by attaching the tip to a tuning fork [Voi15]. The magnet providing the contact for the tunnel current is connected to a coaxial cable while the remaining two magnets are connected to a twisted pair copper wire.

4.4.3 STM-Head

Stable tunneling is only achieved if both parts, the tip and the sample stage, are rigidly connected in a stiff yoke which makes the tunnel junction less receptive to external vibrations. This stiff yoke is the STM-head in which both stages are installed. Mechanical stiffness of the STM-head goes hand in hand with high frequency mechanical resonances. The impact of these resonances on the measurements is minimized if their located above the kHz measurement bandwidth. The mechanical properties are influenced by the material, shape, and the dimensions [RFT04]. Taking these parameters into consideration the STM head was designed with a wedge shape, as shown in **Figure 4.14**, which obeys the required slim shape as well as exhibiting high frequency resonances above the measurement bandwidth.

The *wedge* was hollowed out and split into two shells to insert the tip and the sample stage. While one shell behaves as a cover, the second shelf functions as a mounting plate for the installation of the coarse motor, the scan stage, and the cabling. As shown in **Fig-**

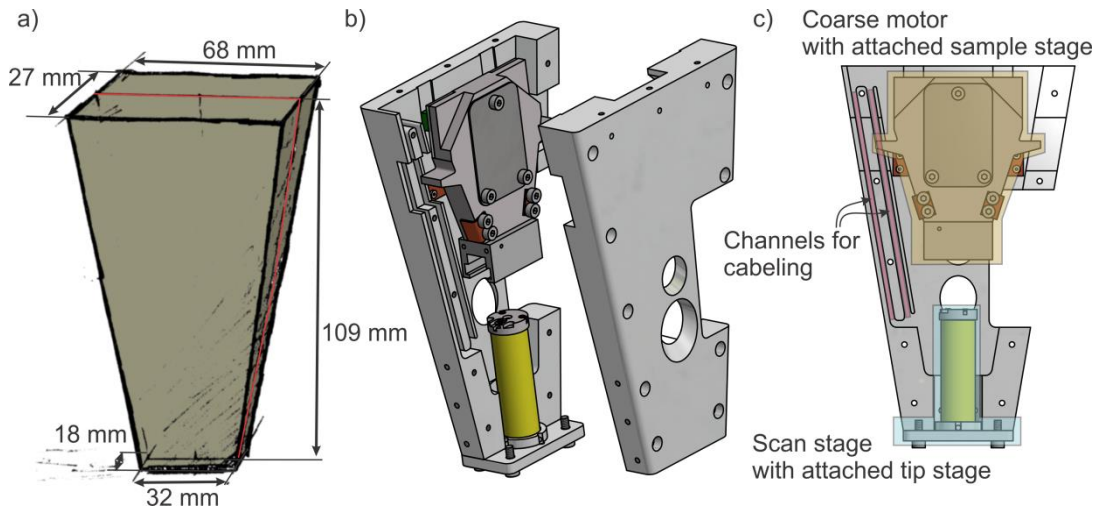

Figure 4.14 (a) Basic wedge shape of the THz-STM. (b) Wedge is cut into two shelfs inside which the STM is installed. (c) The scanning unit including the tip stage of the STM is attached from the bottom part of the wedge. The coarse motor with the sample stage is installed in the upper half of the wedge. To allow tip and sample exchange one side of the wedge features a large opening. In the other side wall of the wedge two channels are milled which will guide cables down to the scanning unit. The optical access to the junction is given by holes in the center of the two shelfs.

ure 4.14, the coarse motor, including the sample stage, is located in the upper half and the scan-stage, including the tip-stage, is mounted at the bottom part. The cables for scan- and tip-stage are placed in two channels embedded in the sidewall of the shell. In addition, holes and clearance had to be cut out of the shells providing access for tip and sample exchange, for the motor-clamping-mechanism and to allow the THz-pluses to reach the tunnel junction. A cap is screwed onto the top of the hollow wedge shells. The spring-stage is mounted at the cap and holes through it guide the cabling.

The shape and the material were chosen such that the head exhibits only high frequency mechanical resonances. Additionally, the material has to possess a good heat conductivity which is important for low temperature operation. The properties of different materials and shapes were compared and computational resonance analyses using the *Autodesk Inventor* software were performed. Based on this survey it was found that pure Aluminum best fulfils the requirements. Theoretically, this material choice would result in an STM head with its lowest theoretical bending mode at 1.5 kHz. This was confirmed by test measurements at the completed STM head, see supplement section 6.2.1 and **Figure 6.1**.

4.4.4 Final STM

Although the head is the core, other important components also have to be taken into consideration for the complete STM setup:

- Cooling and heat radiation shielding
- Sample and tip exchange mechanism
- Vibration isolation and electronic cabling

However, in order to not over burden this chapter with details, these parts are reported in supplemental section 6.2 of this thesis. A picture of the STM is shown in **Figure 4.15**. In this figure, one of the first constant tunnel-current topographies recorded is shown and proves the general stability of the completed STM. In addition to the STM itself, a complete UHV chamber was also designed and set up, in which the STM is placed, and which fits on the optical setup, see **Figure 4.16**. Before presenting the successful coupling of the

free space THz-pulses into the tunnel junction, some final remarks on the STM's stability are given.

A large portion of the development effort was driven by the fact that this machine is placed in an optical laboratory and not in a quiet room. In optical laboratories all kinds of vibrational and electronic noise are present and cannot be eliminated since their sources are often crucial components of the laser system. These noise sources are, for example, the laser system itself which is equipped with large ventilation fans as well as with an electronic controller which does not output clean voltages, the linear stages which emit high pitched sounds when moved, and the air cooling systems of the laboratory.

Despite the noisy environment, the STM has to provide a mechanical stability of the order of picometers in the tunnel junction in order to allow the planned pump-probe experiments to be performed. For this reason the mechanical properties were verified experimentally by different means which are described in detail in the supplemental section 6.2.1. In the completed setup of the THz-STM a vibrational noise floor of less than 2.5 pm is achieved which routinely allows atomic resolution and the possibility of opening the feedback loop for several minutes (limited only by residual drift).

Figure 4.15 (a) 3D drawing of the final design of the THz-STM. (b) Picture of the assembled STM prior closing the shell and radiation shields. (c) Constant current topography recorded on a Gold on Mica surface showing terraces with atomic steps (junction setpoint 1 nA at 1 V).

4.5 THz coupling

In the last two sections the optical setup generating THz pump-probe pulse trains and the scanning tunneling microscope were shown. The last part of this chapter will focus on the combination of these components and on the successful THz coupling into the tunnel junction.

The placement of the UHV chamber including the STM into the optical path, in a way that the STM tip is positioned in the THz focus was done by the following procedure:

- First the THz beam path, including a deflection Au-mirror and two *TPX* lens, was aligned in the absence of the STM. For this alignment the estimated final tip position, as well as the estimated beam path through the viewport of the UHV wedge, was considered. Here, the 30° tilt from the horizontal axis had to be accounted for. For this step the position of the THz beam focus was controlled with the help of a power detector.
- Then the location of the THz focus was marked with two optical laser beams. The two beams were guided along the THz path and focused at the THz focus where they crossed each other.
- Finally the UHV chamber was positioned such that both optical beams were able to scatter directly at the STM-tip. **Figure 4.16** shows photographs of the STM placed in the optical path are shown.

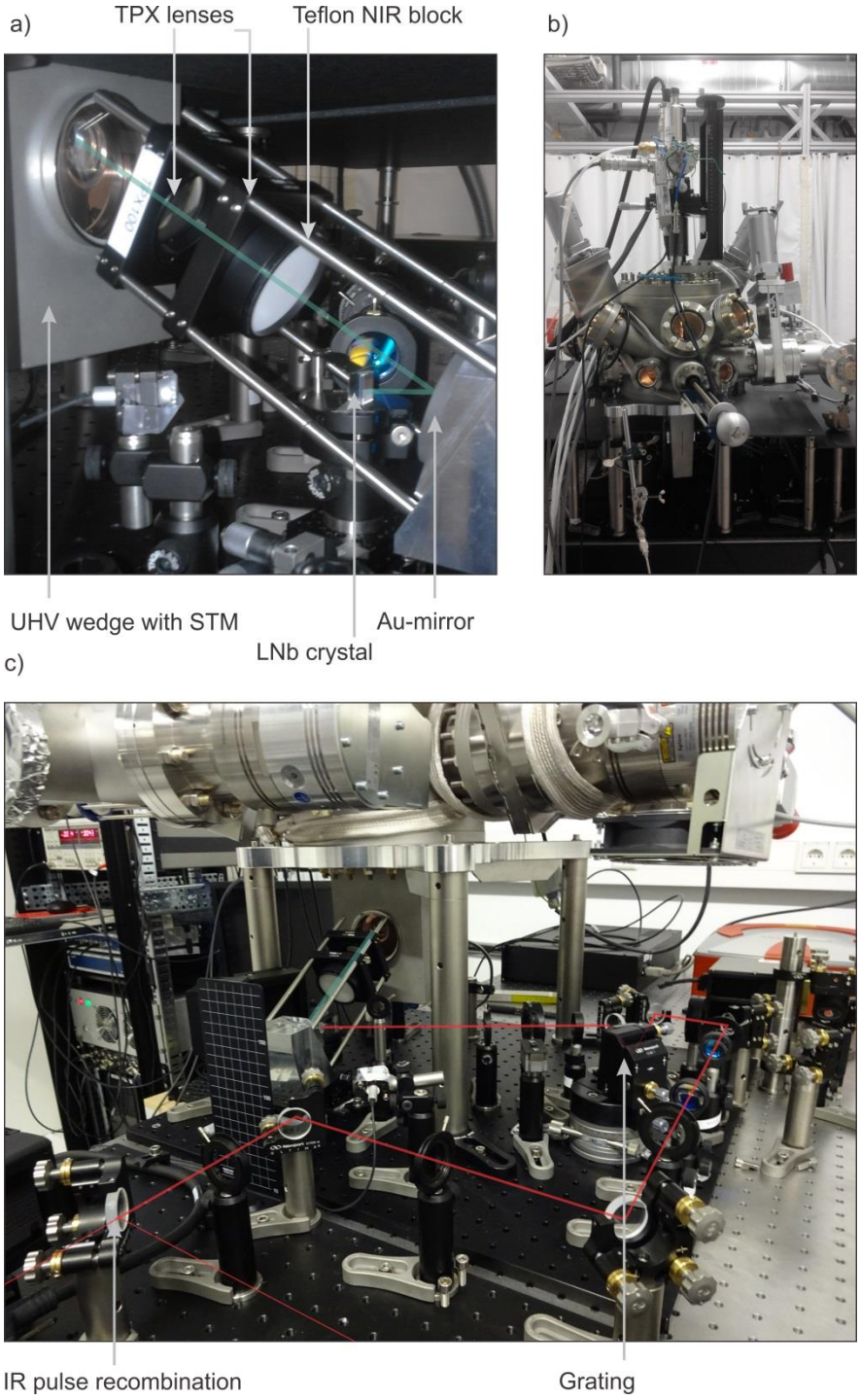

Figure 4.16 Three photographs of the STM placed into the optical setup with different perspectives. The green and the red line indicate the THz and the IR-laser path, respectively.

With this method the STM-tip was placed roughly in the THz focus with a precision of approximately 1 mm. The fine adjustment of the STM is performed by maximizing the current signal induced by THz-pulses in the STM junction. For this procedure, a commercial electro-polished Platinum Iridium (PtIr) tip is brought into tunnel contact on a gold surface. By opening the laser path and tuning the laser to its maximum pulse energy state (20 W at 500 kHz) very strong THz-pulses with a peak electric field of 16 kV/cm are generated and focused on the tip position. Although the tip might not be in the center of the THz focus, the THz electric field strength is sufficient to modulate the measured current even with the tip at the edge of the THz focus. This current is maximized by carefully displacing the STM with the XYZ-manipulator.

When the tip is precisely located in the THz focus the induced current is on the order of several 100 pA for a tunnel setpoint of 1 nA at 10 mV. This large THz induced current corresponds to 0.4 mA during the duration of the single THz-pulse and is most like not a tunnel current but rather a current stemming from field emitted electrons [CJG+13]. In fact, the current can be so strong that the tip modifies mechanically resulting in an unstable junction.

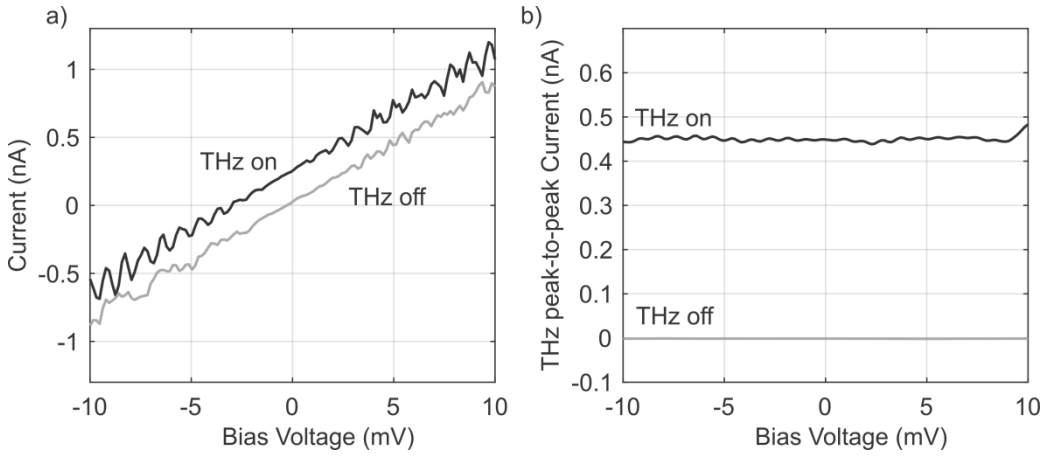

Figure 4.17 (a) *I(V)* spectra recorded on an Au on Mica surface, with and without THz radiation. (Setpoint 1 nA, 10 mV). (b) The contribution of the THz induced current was simultaneously recorded with a Lock-In on-off detection scheme. The THz-pulses were generated by 20 µJ IR-pulses with a repetition rate of 1 MHz and have peak electric fields of approximately 8 kV/cm.

4.5.1 The THz signal

In the last part of this chapter the THz coupling is characterized and described quantitatively. Several tests were performed to confirm that the THz-pulses are indeed inducing voltage pulses and will allow femtosecond pump-probe measurements. An important observation is that the THz induced current does not change sign when the polarization of the external applied bias voltage is reversed and that the induced current does not vanish, even for zero bias voltage. This directly implies that the THz signal cannot be caused by a heat effect altering the tip-sample distance.

This behavior is demonstrated with a *I(V)* spectra during which the THz induced current is simultaneously recorded, see **Figure 4.17**. In this measurement, the induced THz current contribution is so large that it shifts the linear *I(V)* visibly. Furthermore in the recorded voltage window of ±10 mV, the THz induced current does not change as a function of voltage, which indicates that the induced voltage is much larger than the external applied voltages. The THz induced voltages can be estimated based on the induced current magnitude of 450 pA at 1 MHz and the given junction setpoint of 1 nA at +10 mV. If a rectangular shape of the induced voltage pulse with a width of 1 ps is assumed and the *I(V)* is approximated by an *ohmic* trend then the THz pulses would induce a voltages of 450 V. In

practice the induced voltage is smaller since nonlinearities of the *I(V)* and a more realistic pulse shape have to be considered and presumably reaches magnitudes in the range of 5-50 V.

The presented *I(V)* spectra have shown that the THz-pulses induce a transient voltage on the order of volts at the junction. The timescale at which this effect occurs and whether it is sufficient for obtaining femtosecond time resolution remains to be determined. The time resolution can only be benchmarked indirectly, as the transient voltage cannot be measured directly. A possible indirect method is the recording of the current induced by two identical THz-pulses as a function of their delay time. The correlation spectrum of such a measurement is shown in **Figure 4.18**.

The spectrum shows a sharp peak around zero delay with a width of 400 fs (full-width-half-maximum) and amplitude of 160 pA. Away from the peak the THz induced current

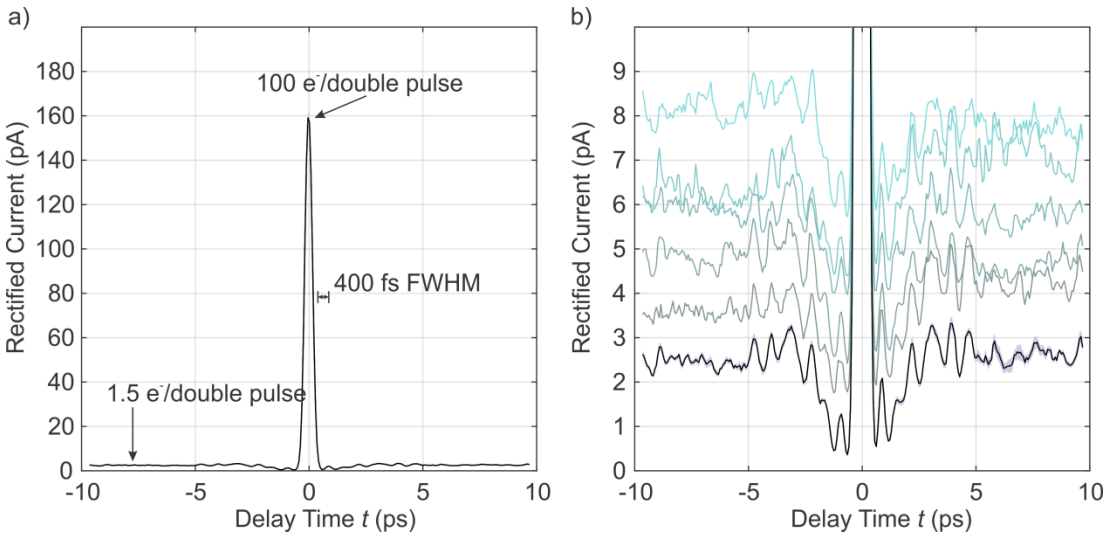

Figure 4.18 (a) recorded pulse-pulse correlation current as function of the pulse-pulse delay time. The measurement was performed on an Au on Mica surface with a tunnel setpoint of 130 pA at 22 mV. For the Lock-In detection the complete THz pulse train was on-off modulated. The THz-pulse pairs had a repetition rate of 10 MHz. In order to prevent tip changes the STM feedback was kept 'on' and the tip is slightly retracted at zero delay time to compensate for the excess current. (b) Zoom-in of the same measurement, black line. The signal was averaged over five individual traces (lighter lines, plotted with offsets to provide better visibility), showing that each individual trace has a noise floor much less than 1 pA.

drops to 2.5 pA. In this low current region reproducible features are observed which surround the central peak symmetrically. The typical signal magnitude of these features is 0.8 pA. The central peak is a strong indication that the width of the THz induced voltage pulses is similarly short and shows that the THz-STM setup allows electronic pump-probe spectroscopy with a time resolution in the femtosecond regime.

The resolved spectrum requires a more detailed examination with respect to the underlying current rectification principle. This principle can be discussed using the recorded THz-pulse shape $E(t')$ and a *I(V)* curve recorded on Au, see **Figure 4.19**. In the following this *I(V)* is approximated by the function $I(V) \sim B \cdot (e^{\kappa_1 V} - e^{-\kappa_2 V})$ with $\kappa_1 = 2.07\ \mathrm{V}^{-1}$ and $\kappa_2 = 2.25\ \mathrm{V}^{-1}$. Then the $I(V)$ is scaled to the setpoint used of 130 pA at 22 mV to reproduce the tunnel condition during the recording of the spectrum. Based on the coupling properties given in section 4.2, the THz induced voltage trace $V_{\mathrm{THz}}(t')$ corresponds to $E(t')$ up to a conversion factor α, and the transient current $I_{\mathrm{THz}}(t')$ is given by:

$$\begin{aligned} V_{\mathrm{THz}}(t') &= \alpha \cdot E(t') \\ I_{\mathrm{THz}}(t') &= I\big(V_{\mathrm{THz}}(t')\big)\,. \end{aligned} \qquad 4.6$$

Figure 4.19b) shows the calculated $I_{\mathrm{THz}}(t')$. By averaging $I_{\mathrm{THz}}(t')$ over a time T the transient current leads to a finite rectified current which corresponds to the measured current in the experiment:

$$\bar{I}_{\mathrm{THz}} = \frac{1}{T}\int \mathrm{d}t' I_{\mathrm{THz}}(t') = \frac{1}{T}\int \mathrm{d}t' I\big(V_{\mathrm{THz}}(t')\big)\,. \qquad 4.7$$

The rectified current of a single THz pulse can be computed explicitly for a given α and the peak induced voltage can be found with this approach by adjusting the conversion factor α until the computed rectified current matches to the measured one. The base-line of the spectrum in **Figure 4.18**b) shows that each THz pulse induces 1.2 pA at a pulse repetition rate of 10 MHz which corresponds to T = 100 ns. Based on this the induced voltage at the THz pulse peak is estimated and yields +3.4 V.

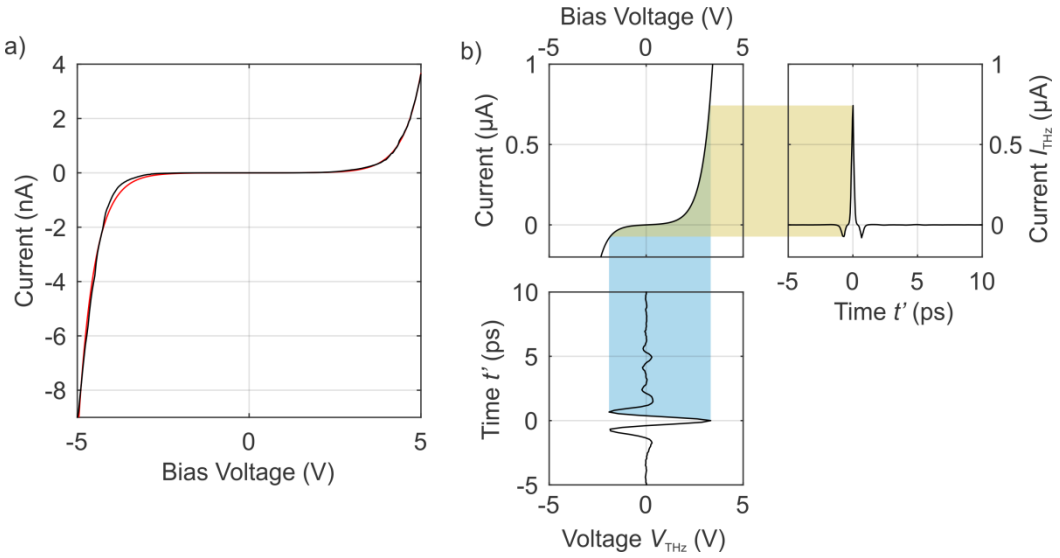

Figure 4.19 (a) (black line) *I(V)* recorded on Au (setpoint 4 nA at 5 V). (red line) $B \cdot (e^{\kappa_1 V} - e^{-\kappa_2 V})$ fit of the spectra. (b) Illustration of the rectification process of the THz laser pulse induced voltage in the tunnel junction on Au. The time trace of the induced voltage $V_{\mathrm{THz}}(t')$ (at the bottom) is converted into a tunnel current pulse $I_{\mathrm{THz}}(t')$ (right) via the *I(V)* characteristic (shown in the center). The time trace of the voltage is based on a typical THz-pulse shape and has no DC component. The resulting current trace has a finite DC component because the *I(V)* curve is nonlinear. The *I(V)* used here is the fit curve from (b) which is scaled to the setpoint 130 pA at 22 mV.

The formalism introduced can be used even further to calculate the full correlation spectrum $\bar{I}_{\mathrm{THz}}(t)$:

$$\begin{aligned} V_{\mathrm{THz}}(t') &= \alpha \cdot \big(E_1(t') + E_2(t'+t)\big) = V_{1,\mathrm{THz}}(t') + V_{2,\mathrm{THz}}(t'+t) \\ I_{\mathrm{THz}}(t',t) &= I\left(V_{1,\mathrm{THz}}(t') + V_{2,\mathrm{THz}}(t'+t)\right) \\ \bar{I}_{\mathrm{THz}}(t) &= \frac{1}{T}\int \mathrm{d}t' I_{\mathrm{THz}}(t',t) = \frac{1}{T}\int \mathrm{d}t' I\left(V_{1,\mathrm{THz}}(t') + V_{2,\mathrm{THz}}(t'+t)\right), \end{aligned} \tag{4.8}$$

where E_1 and E_2 are the electric fields of the two THz-pulses and $V_{1,\mathrm{THz}}$ and $V_{2,\mathrm{THz}}$ are the corresponding induced voltages. The Lock-In modulation has to be considered in addition to equation 4.8 if the measured correlation spectrum is approximated by this formalism.

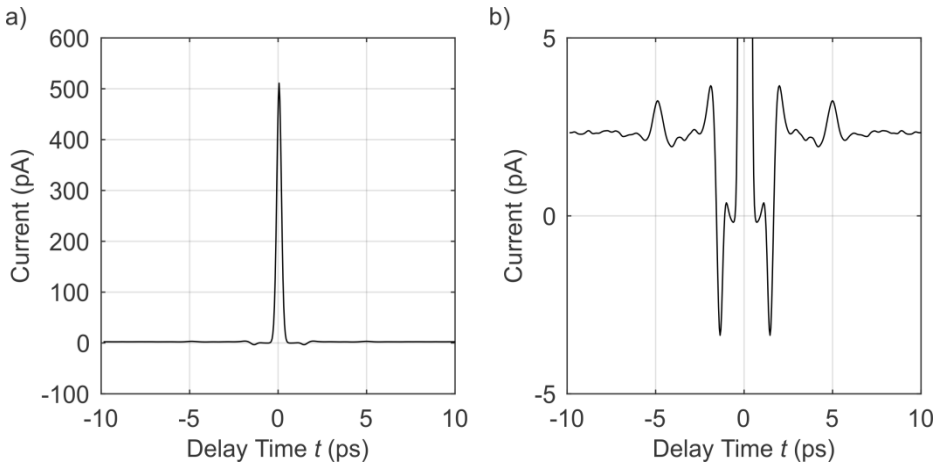

Figure 4.20 (a-b) calculated correlation spectrum to estimate the spectrum in **Figure 4.18**. For the calculation the *I(V)* curve and the THz field shape E(t′) shown in **Figure 4.19**b) are used (setpoint 130 pA at 22 mV, THz pulse repetition rate 10 MHz). The conversion factor α was chosen such that the THz field induces at its peak a voltage of +3.4 V.

In **Figure 4.20** the calculated correlation spectrum $\bar{I}_{\mathrm{THz}}(t)$ is shown which results when all mentioned details are taken into account. The calculated spectrum is very similar to the recorded correlation function shown in **Figure 4.18**. The main difference between the calculation and the recorded curve is the height of the central peak. This is explainable by the closed feedback loop during the measurement and the thereby restricted net current flow.

Not only is the peak of the correlation spectrum interesting, so too is the signal when both pulses do not overlap. In this regime the rectified current is almost two orders of magnitude smaller and reproducible features surround the correlation peak symmetrically in the recorded correlation spectrum, see **Figure 4.18**b). Similar features are also found in the calculated correlation spectrum, see **Figure 4.20**b). These feature stem from the shape of the THz pulse which contains small oscillatory tails due to water absorption or reflections. It should be noted that such effects would affect the signal of pump-probe spectra and would have to be considered carefully in the analysis of the experimental data. These features depends strongly on details of the induce voltage shape and details of the *I(V).* It is therefore not surprising that these features differ between calculation and measurement since the THz-pulse shape or the *I(V)* curve used in the calculation do not correspond identically to the conditions during the measurement.

Despite the mentioned differences the calculated correlation spectrum clearly shows that the measured spectrum curve is explained in the framework presented here. This proves, in particular, that the shape of the induced voltage pulse corresponds to the shape of THz field. In addition, it worth pointing out that the small features surround the center peak are already visible in the single measurement trace and signal variations on the order of 100 fA are distinguishable. This impressively demonstrates the high signal quality achieved with the new THz-STM.

4.6 Summary

In this chapter the development of a new STM with femtosecond time resolution was presented. This was achieved by the coupling of a highly effective and fast repeating THz-pulse source with a very compact and stable scanning tunneling microscope. The THz source built is able to operate in different regimes, with large THz-pulse energies but lower repetition rates, up to 20 nJ at 500 kHz, or high repetition rates but small THz energies, 5 pJ at up to 40 Mhz. A novel design for a low temperature STM was envisioned allowing optical access to the tunnel tip directly from the *ex-situ* environment (no optical components inside the UHV chamber). For this design a new coarse motor was developed and tested. The properties of the completed STM were analyzed and the vibrational noise was found to be smaller than 2.5 pm.

In the last part of the chapter, first measurements on Au prove the unique properties of the instrument. It was shown that the THz-pulses induces fast oscillating voltage pulses proportional to its electric field in the tunnel junction and that the instrument will allow pump-probe spectroscopy with femtoampere signal sensitivity and time resolution in the femtosecond regime.

Chapter 5 Charge density wave dynamics in 2H-$NbSe_2$

The development of the THz-STM with sub-picosecond resolution presented in the last chapter was driven by the goal of investigating the temporal imprint of atomic scale inhomogeneities in complex materials. Here, this idea was realized for the first time by the exploration of Niobium Diselenide (2H-$NbSe_2$), which is a prominent sample system for the study of charge density wave (CDW) formation.

A charge density wave is the emergence of a wave-like modulation in the electron density originating from the electron phonon interaction [Grü94]. This phenomenon exhibits collective modes and is found in low dimensional system such as 2H-$NbSe_2$ [Grü94]. The properties of CDW's are highly affected by atomic defects, which act as pinning centers and can lead, for example, to a modification of the dispersion of the collective modes or to a locally increased phase transition temperature [Grü94, ACR+14].

This chapter starts with the fundamentals of the sample system 2H-$NbSe_2$ and the formation of CDW's. Although 2H-$NbSe_2$ is often called a '*prototypical*' CDW, the origin of CDW's in this system is still under debate [ARA+15, WRC+11, FvW15]. In this introductory part some static STM measurements of 2H-$NbSe_2$ and its CDW are also presented.

In the main part of the chapter THz-STM pump-probe measurements will be shown and discussed. It will be shown that the THz-STM can resolve the dynamics of the system with femtosecond resolution. In fact, different dynamic processes can be identified such as the amplitude and the phase mode of the CDW. Based on these observations the atomic scale inhomogeneity of the dynamics is investigated in the last part of the chapter.

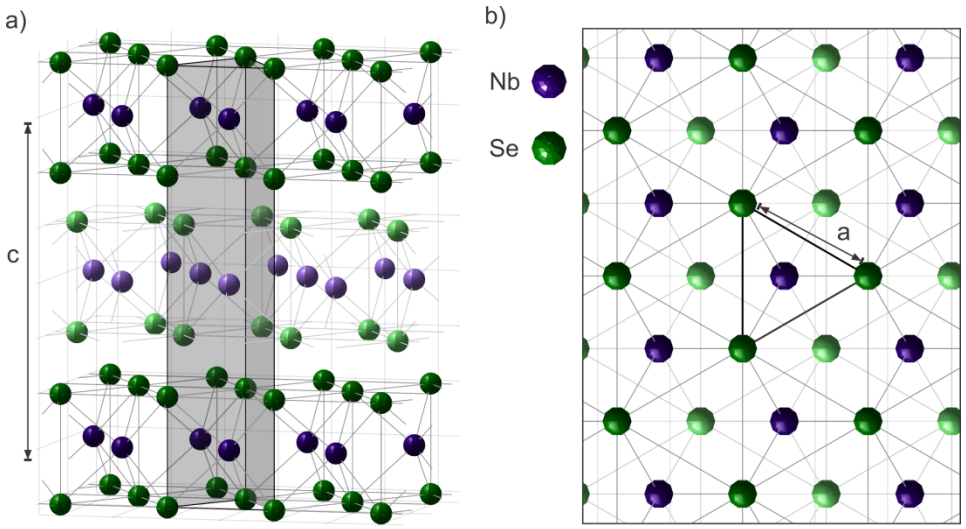

Figure 5.1 Side (a) and top (b) view of the crystal structure of 2H-$NbSe_2$. Each 2H-$NbSe_2$ layer consists of three atomic planes; the plane of the Nb atoms (violet spheres) is between the two planes of Se-atoms (green spheres). Three layers are shown here, the spheres of the middle layer are brightened for better visibility. Each layer is rotated by 180° in plane with respect to the previous one and aligned such that the Nb atoms are on top of each other.

5.1 Basic concepts

Niobium Diselenide (2H-$NbSe_2$) is a layered transition metal dichalcogenide (TMD) and a quasi 2D system. The structure of 2H-$NbSe_2$ is shown in Figure 5.1. Each layer exhibits a trigonal prismatic unit cell in which a Niobium (Nb) plane is placed between the Selenium (Se) planes. In the bulk crystal, 2H-$NbSe_2$ has an alternating stacking of layers such that the Nb atoms are on top of each other. The lattice constants are a = 3.445 Å and c = 12.551 Å [NR11, KT16].

Whereas the intra-layer bonding of the atoms is of covalent nature and strong, the layers are only weakly coupled via Van-der-Waals interaction. For that reason the electric and optical properties remain almost two dimensional [WY69, KT16]. Another consequence of the weak coupling is the possibility of cleaving large surface areas (on the order of mm^2) without atomic steps simply by using adhesive tape. Combined with an inert surface (free of dangling bonds) this property allows for the preparation of the clean and high quality surfaces necessary for scanning tunneling techniques.

Bulk 2H-$NbSe_2$ specimens exhibit a charge density wave (CDW) transition at 35 K and becomes superconducting below 7 K [NR11]. The origin of the CDW formation is still under debate although it has been studied for decades. The superconducting state stems from conventional electron-phonon coupling and can be described in the picture of Bardeen-Cooper-Schrieffer (BCS) theory [BK08]. The nature of the coexistence of the CDW and superconductivity was the subject of various studies with particular focus on the interplay between them, and the competition thereof [RHK+12, XZW+15].

Historically, the formation of a charge density wave in 2H-$NbSe_2$ was confirmed by neutron scattering experiments [MAD77, MAD75]. Earlier indications of the CDW formation were already given by experiments sensitive to the electronic properties, such as the broadening of Bragg peaks in electron diffraction of TaS_2 (a similar TMD system) and the sign change of the Hall-coefficient in transport measurements [WDSM74, LGMW70]. The results of neutron scattering proved that changes in the electronic properties are accompanied by a periodic displacement of the atomic core positions, as neutron scattering is sensitive to the position of the nuclei. In these experiments additional Bragg peaks appear at wave vectors $\vec{q}_{\mathrm{CDW}}$ with magnitude of about one third of the magnitude of the original lattice vector $\vec{q}_{\mathrm{l}}$, $\vec{q}_{\mathrm{CDW}} = (1-\delta)\frac{\vec{q}_{\mathrm{l}}}{3}$ with $\delta = 0.02$. Their appearance and location could only be explained by the formation of an incommensurate CDW with a wavelength of slightly more than three times the lattice constant. Ever since then, CDW formation in 2H-$NbSe_2$ has been intensively investigated. One primary aspect of the research was, and still is, the origin and the mechanism of the CDW formation.

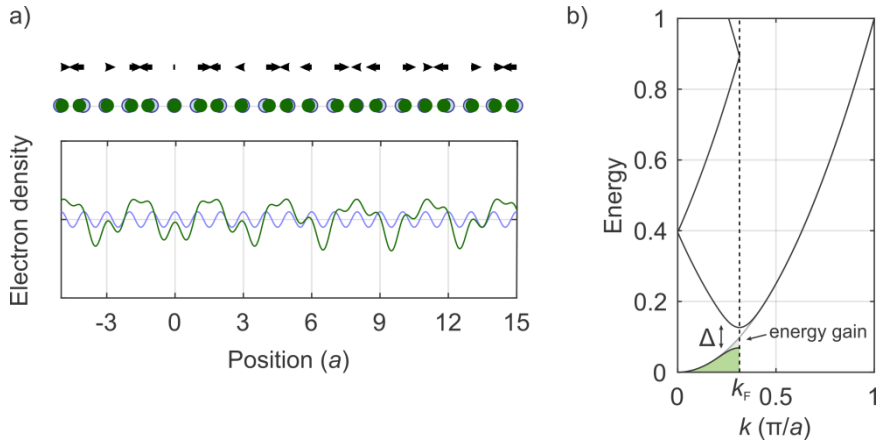

Figure 5.2 (a) Illustration of the formation of an incommensurate charge density wave in 1D. **Top**: Due to the formation of the CDW the position of the atoms of the 1D chain with lattice constant a are displaced (blue circles show the position of the atoms without CDW, green circles show displaced atoms, black arrows are the displacement field). In this example the CDW has a wavelength $\lambda = 3.1\ a$. **Bottom**: Charge density as function of position (blue: without CDW, green: with CDW). Here the charge density was approximated by Gaussian functions centered at the atom positions. (b) Schematic band diagram of the 1D chain. With the formation of the CDW a gap Δ is opened at the CDW wave vector which corresponds to the Fermi wave vector. A net energy gain will result if the gap shifts occupied states down and unoccupied states up in energy.

5.2 About the CDW formation mechanism

The concept of a charge density wave (CDW) in solids was introduced by Peierls [Pou16, Grü88]. The CDW is a modulation of the charge density ρ_{CDW} with a wave vector $\vec{q}_{\mathrm{CDW}}$ on top of the equilibrium density ρ_0. The modulation of the charge density is accompanied by the displacement of the atomic positions $\vec{u}$ and the opening of an electronic gap Δ. This situation is illustrated in **Figure 5.15**. Similar to other thermodynamic states of matter, a CDW occurs when the system is cooled below a transition temperature T_c.

The reason for the formation of a CDW is the possibility of lowering the free energy of the system. In textbooks [Grü94, Kit96, Grü88] the CDW is typically introduced with a pure 1D system like an atomic chain where the CDW formation can be explained in the picture of a *Peierls* transition. In this picture the system lowers its electronic energy by opening a gap around the Fermi energy. To do this, electronic states with quasimomentum $\vec{k}$ and

$\vec{k} + \vec{k}_F$ have to be able to scatter into each other (and to mix). This becomes possible by electron-phonon interactions and results in the introduction of a periodic distortion of the lattice with a wavelength corresponding to two times the Fermi wave vector ($2\vec{k}_F$). The distortion simultaneously introduces strain which limits the total energy gain. Interestingly an ideal 1D electron system is always unstable against the formation of a CDW; an infinitesimally weak coupling between electron and phonons will force the formation of a CDW.

In contrast to this hypothetical 1D model, in real systems with higher dimensions this process relies sensitively on Fermi-surface nesting [ZCZ+15, Ros11, Mon12]. Fermi-surface nesting describes the existence of parallel sections of the Fermi surface, which result in a partially one-dimensional character. However, in 2H-$NbSe_2$ such nesting conditions cannot be confirmed experimentally [BKZ+09, RSK+01]. In addition to the missing Fermi-surface nesting, several other experimental observations do not match to a model which relies on weak electron-phonon coupling to open an electronic gap at the Fermi wave vector $\vec{k}_F$ [WRC+11, ARA+15]. In fact, the debate on the origin of CDW formation in 2H-$NbSe_2$ is ongoing. Perhaps the most promising explanation is based on strong electron-phonon coupling that leads to a broad softening of acoustic phonons at the CDW wave vector down to zero energy [ZCZ+15, FvW15, WRC+11, ARA+15]. This debate strongly influences the interpretation of low voltage tunnel current spectra measureable with STM.

A typical tunnel current spectrum in a narrow voltage window (from −80 mV to +80 mV) is shown in **Figure 5.3**b). The *I(V)* spectrum shows a distortion located at zero bias voltage. The corresponding dI/dV shows a gap-like structure with kinks at −35 mV and +35 mV, see **Figure 5.3**d). After its first observation, this *'gap'* was attributed to the CDW band gap since it appears simultaneously to the CDW [WGS+90]. However, the width of the gap-like feature would correspond to an electronic gap of 35 meV and is much larger than the CDW-gap found by angle resolved photoemission spectroscopy (ARPES). This technique finds a gap on the order of 4-5 meV in the Fermi surface pocket around the K-point [BKZ+09, RHK+12]. Indeed, recent studies suggest that the tunnel spectroscopy feature is not the CDW gap itself, but it is nevertheless directly connected to CDW formation

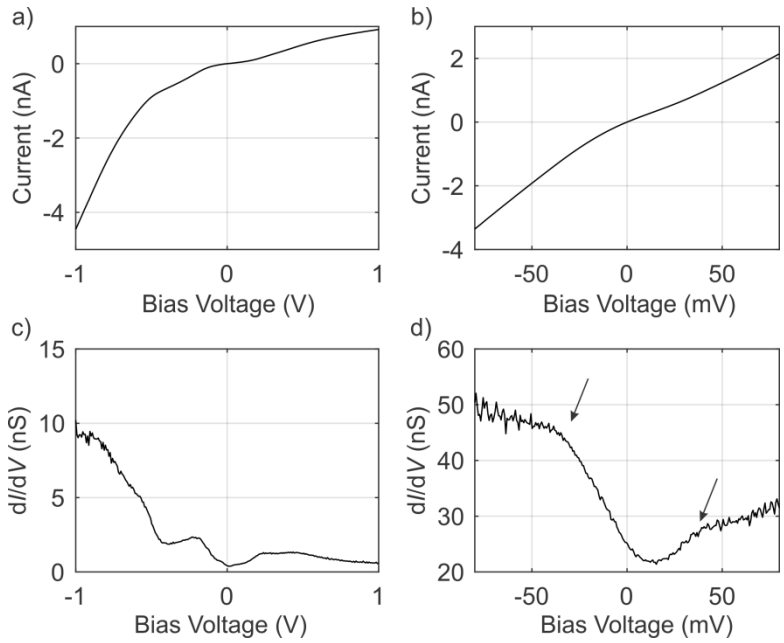

Figure 5.3 Typical $I(V)$ and the corresponding dI/dV spectra recorded on a 2H-$NbSe_2$ surface at 20 K. (tunnel setpoint (a) and (c): 1 nA at +1 V and (b) and (d): 2 nA at +80 mV). The two black arrows indicate the two prominent kinks which only appear in the CDW state of 2H-$NbSe_2$.

[SYH+13]. It appears that the origin of the two kinks is the renormalization of the electronic states due to strong electron-phonon coupling [SYH+13]. In a further STM study investigating 2H-$NbSe_2$ in the single layer limit, a 4 meV wide gap was found which supports the statement that the wide kinks are not the CDW gap [UBZ+16].

For completeness, **Figure 5.3**a) shows the current spectra with a wider voltage window. In the voltage range from −500 mV to +500 mV the spectrum is dominated by a hook-shaped non-linearity. The differential conductance is larger at negative voltage polarity than at positive polarity, see **Figure 5.3**c). It is worth noting that the THz induced voltage will presumably be located in this voltage range.

5.3 CDW modes

Although the full microscopic picture is missing for 2H-$NbSe_2$, the CDW formation can still be described with phenomenological Landau theory [Grü94, Ric75, SN86]. In this framework the free energy $F[\Psi]$ is minimized by a complex order parameter $\Psi = |\Psi|\, e^{i\varphi}$ which is proportional to the displacement field $\vec{u}$ of the atoms or the modulated electron density ρ_{CDW}.

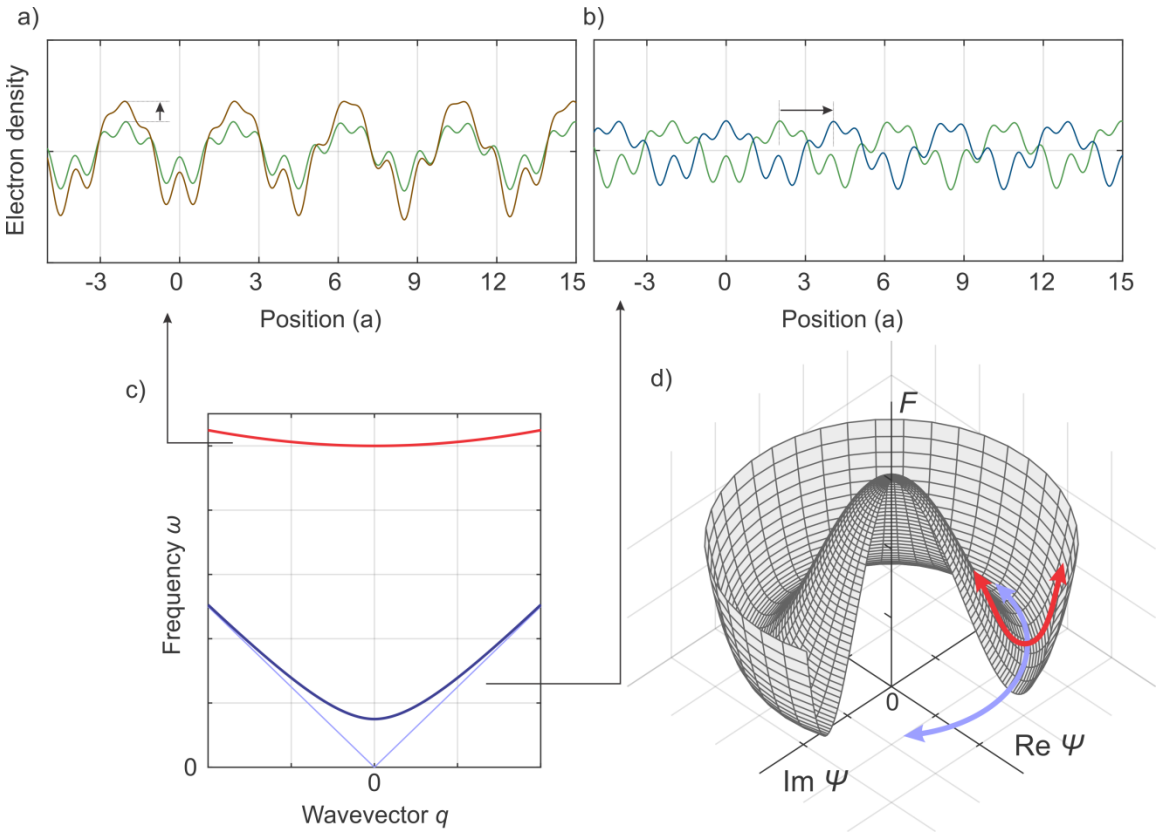

Figure 5.4 Illustration of the two collective modes of a CDW system that modify the equilibrium CDW (green line). (a) In the *amplitude* mode the displacement is increased, which results in a larger amplitude of the charge density modulation (red line). (b) The *phase* mode shifts the maximum of the charge density modulation (blue line). (c) Dispersion relation of the amplitude mode (red) and the phase mode (pale blue). The presence of pinning lifts the $q = 0$ *phase* mode to finite energies (dark blue). d) *Mexican-Hat* potential of the free energy F as function of the complex order parameter Ψ. Here the two collective modes are pictured with arrows (red arrow: *amplitude* mode, blue arrow: *phase* mode).

While more information on those phenomenological theories can be found elsewhere, the important essence for this thesis is the occurrence of low energy collective modes of the order parameter in the free energy potential landscape, see **Figure 5.4**d) [LRA74, Grü94]. For long wavelengths ($q \ll q_{CDW}$), these modes are typically separated into the *phase* and the *amplitude* mode, schematically shown in **Figure 5.4**a) and b). The *amplitude* mode corresponds to the modification of the amplitude of the complex order parameter $|\Psi| + \delta \sin(qx - \omega t)$ and exhibits a rather flat dispersion relation with a finite frequency at $q = 0$ (excitation gap), see **Figure 5.4c**).

The *phase* mode, on the other hand, is the modification of the phase of the complex order parameter $\varphi + \Delta\varphi \sin(qx - \omega t)$. In contrast to the *amplitude* mode the dispersion of the *phase* mode of an ideal and incommensurate CDW system is gapless, see **Figure 5.4c**). Since the $q = 0$ phase mode can carry a net current this would have the interesting consequence of a supercurrent running without resistivity through the system. Indeed the theory of CDW proposed by Fröhlich [Frö54] was one of the precursors of BCS-theory, which is the accepted theory for the description of conventional superconductivity. However, in real materials a CDW pinning at impurities suppresses the supercurrent. In this situation the free energy *F* is minimized at a certain phase of the CDW and a finite energy is necessary to unlock it. This lifts the *phase* mode at $q = 0$ to a finite frequency, see **Figure 5.4c**).

The occurrence of these two collective modes and their dynamic properties were experimentally investigated by various means. In the 1980s frequency dependent electric transport measurement of 1D systems ($NbSe_3$, TaS_3, $K_{0.3}MoO_3$) showed conductance peaks at around 0.01 - 0.1 THz, which were attributed to the pinned *phase* mode [Grü88]. For 2H-$NbSe_2$ an *amplitude* mode was found by Raman-spectroscopy at a wavenumber of 40 cm^{-1} (1.2 THz) [TSS76, XZW+15]. By comparison, in Raman-experiments performed on $La_{2-x}Sr_xCu0_4$ the appearance of additional peaks at 30 cm^{-1} (0.9 THz) and 80 cm^{-1} (2.4 THz) was reported, which were attributed to the *phase* and the *amplitude* mode [STH06].

Although static optic probes elucidated the basic properties of collective CDW-modes, the extraction of the dynamic behavior of collective modes by static measurements is unfeasible because of their broad spectral response. Alternatively optical pump-probe experi-

ments can measure them stroboscopically. This was successfully demonstrated for the CDW system $K_{0.3}MoO_3$ [DBM99]. Here an oscillation frequency of $\nu = 1.7$ THz and a lifetime of $\tau > 10$ ps was found, which was attributed to an *amplitude* mode. In similar experiments even *phase* modes have been identified ($\nu = 0.01$ THz and $\tau > 60$ ps) [RXL04]. In a further study of a La_2SrCO_4 film collective CDW modes could be identified [TMB+13]. Surprisingly, the CDW state of 2H-$NbSe_2$ has only been weakly explored by time-resolved experiments while other TMD CDW systems such as TaS_2 were investigated extensively [HRK+12, RHW+11, PLM+14]. In particular, neither the *amplitude* mode nor the *phase* modes in 2H-$NbSe_2$ have yet been observed in a time-resolved fashion.

5.4 CDW topography

Although the origin of the CDW in 2H-$NbSe_2$ is still unclear its presence is indu-

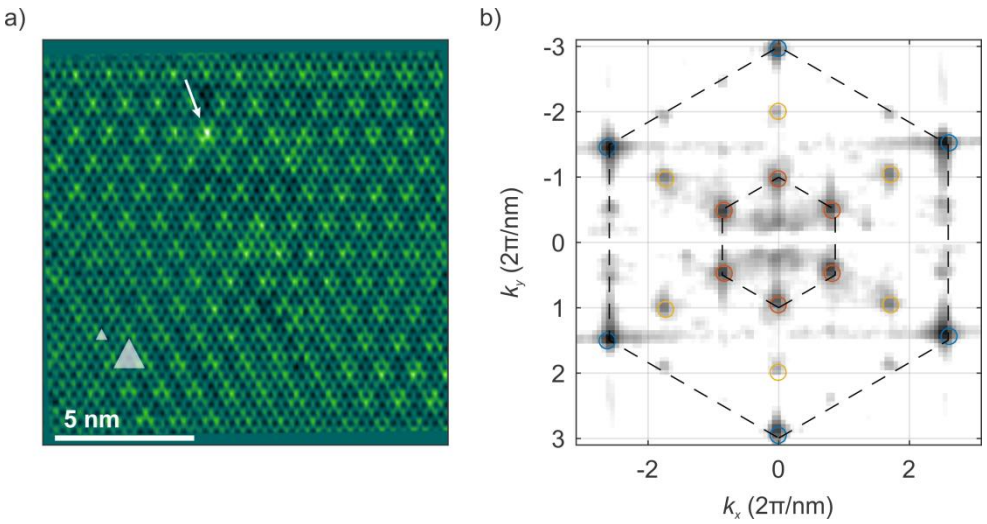

Figure 5.5 (a) constant current STM topography of 2H-$NbSe_2$ at 20 K. (Junction setpoint 40 pA and 32 mV). The atomic as well as the CDW corrugation are clearly visible. Both form a hexagonal lattice and the CDW has a unit cell approximately three times larger than the atomic lattice, which is indicated by the two triangles. White arrow marks a dominant defect. (b) Amplitude of the Fourier transformation of the STM topography. The blue circles mark the peaks of the atomic lattice and the red circles mark the CDW lattice. The yellow circles mark additional satellites corresponding to difference wavelengths between the atomic and CDW lattice. Not all peaks are marked. The dashed lines connect the peaks of the atomic lattice as well as the peaks of the CDW lattice.

bitable. Scanning tunneling microscopy shows the CDW formation perhaps most impressively. As early as 1987, shortly after the invention of STM itself, the first studies of 2H-$NbSe_2$ investigated with STM were published [TBM+86, TBK+87, KBE+87]. In 1988 the first observation of the CDW with a low temperature STM was reported [GJC+88].

In STM topographies the CDW is visible as an additional modulation of the atomic corrugation as shown in **Figure 5.5**a). In this typical STM topography the most dominant feature is the hexagonal atomic corrugation which corresponds to the positions of the Se-atoms of the surface [GJC+88]. The second most dominant feature is the corrugation of the CDW. The lattice formed by the CDW is about three times larger than the atomic lattice and also hexagonal. In addition to the periodic structures the topography exhibits some local defects disturbing the periodic structures.

The connection between CDW and atomic lattices can be visualized in the Fourier transform of the topography, see **Figure 5.5**b). In reciprocal space the hexagonal atomic and CDW lattice appear as peaks. From the peaks the ratio of the atomic ($\vec{q}_{\mathrm{l}}$) and the CDW ($\vec{q}_{\mathrm{CDW}}$) lattice vectors can be obtained:

$$\vec{q}_{\mathrm{l}} = (3.1 \pm 0.05) \cdot \vec{q}_{\mathrm{CDW}} \quad \text{or} \quad \vec{q}_{\mathrm{CDW}} = (1-\delta)\frac{\vec{q}_{\mathrm{l}}}{3} \text{ with } \delta = (0.032 \pm 0.016). \tag{5.1}$$

In the presented topography, the CDW lattice is indeed incommensurate with the atomic lattice, and a mismatch value similar to the neutron scattering observations was found [MAD77]. As a consequence the apparent maximum of the CDW lattice wanders with respect to the atomic lattice. This behavior is illustrated in **Figure 5.6** by comparing the CDW maximum position to a hypothetical commensurate CDW lattice.

A closer look at the marked defect, **Figure 5.6**a) reveals another interesting feature. The CDW lattice seems to be aligned such that its maximum perfectly matches to the position of the defect. Although in this specific case the match might merely be coincidence, it still addresses an important point of CDW formation: the pinning by defects. In the vicinity of pinning centers a charge density wave can form at temperatures much higher than that of the bulk transition. In STM studies of 2H-$NbSe_2$ CDW transition temperatures up to 96 K (three times the bulk transition temperature) were reported for localized CDW formation around defects [ACR+14, CZI+15].

From STM measurements the very local effect of the impurity on the CDW becomes obvious. As previously mentioned, the impurity pinning affects the *phase* mode of the CDW globally. Naturally the question arises of how the impurities pin the collective *phase* mode on the atomic scale. THz-STM is the only known technique that allows these questions to be answered by means of locally resolved pump-probe spectroscopy with atomic spatial resolution and femtosecond time resolution.

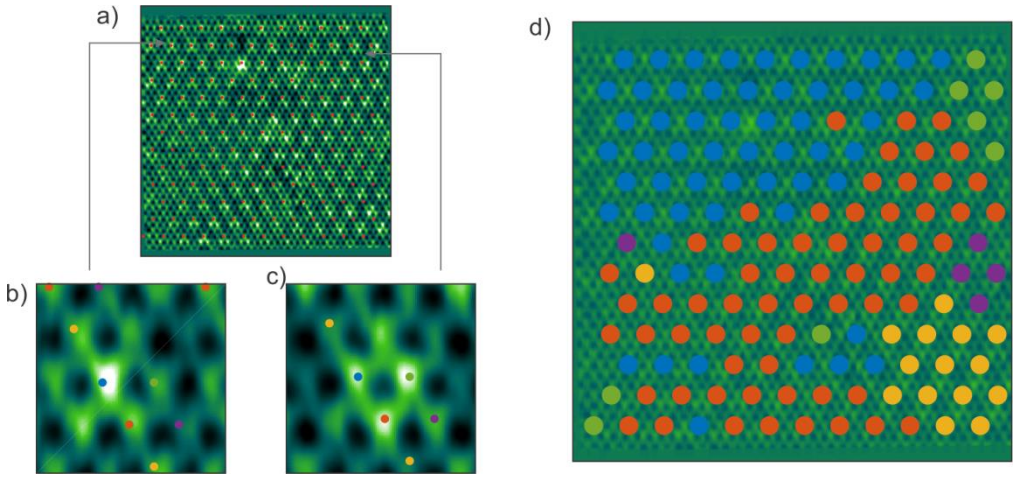

Figure 5.6 Analysis of the phase of the CDW relative to the atomic lattice observed in the constant current topography **Figure 5.5**. (a) Red points mark an ideal 3x3 super lattice. (b-c) The maximum of the CDW shifts with respect to the ideal 3x3 lattice. Colored points are positioned in reference to the ideal 3x3 lattice and help to identify the shift of the CDW maximum. (d) Map of the CDW maximum position in the ideal 3x3 unit cell showing the shift of the CDW phase. Here each 3x3 unit cell is marked with a dot and its color reflects the position of the CDW maxima in the 3x3 unit cell in accordance with their assignment in (b-c).

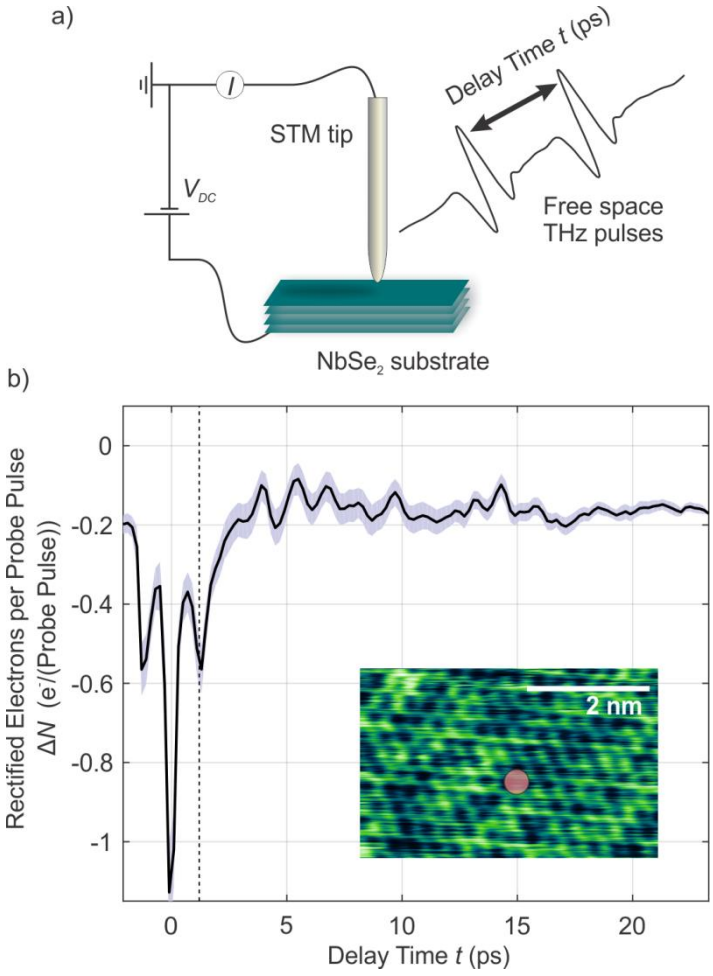

Figure 5.7 (a) Schematic of the experimental setup. (b) Femtosecond pump-probe spectrum recorded with THz-STM on 2H-$NbSe_2$ at 20 K (junction setpoint 1 nA at +1 mV). THz source was adjusted to a pulse repetition rate of 40 MHz, and to a pump and probe pulse amplitude of 130 V/cm in the THz focus. The dotted line separates the *excitation* region from the *relaxation* region. Inset shows position of the tip during the measurement.

5.5 Femtosecond pump-probe spectroscopy

In the previous part of the chapter, the formation of a CDW and its manifestation in 2H-$NbSe_2$ was introduced. It was pointed out that local atomic defects globally influence the dynamics of CDW's but the local impact on the dynamics is still unclear. Spatially resolved pump-probe spectroscopy with the THz-STM is the only known technique able to resolve the dynamic properties on the atomic scale. The next part of the chapter focuses on THz pump-probe spectra recorded on 2H-$NbSe_2$ in its CDW phase.

Figure 5.7 report a typical THz-STM pump-probe spectrum recorded on 2H-$NbSe_2$. This spectrum and all the following ones are recorded with an open feedback loop, at zero bias voltage ($V_{DC} = 0$) and with a Lock-In detection scheme with on-off modulation of the probe pulse at 617 Hz. The measured signal is therefore the additional rectified current due to the presence of the probe THz-pulse. The THz induced current signal is converted to number of electrons rectified per probe pulse (ΔN) [e^-/pulse] by dividing the current signal by the pulse repetition rate (40 MHz) and the electron charge.

The pump-probe spectrum has quite a complex shape and can be characterized as follows. A dip at zero time delay with amplitude of −1.2 e^-/pulse is the central feature and is symmetrically surrounded by two humps. This dip-structure is offset from the base-line of the

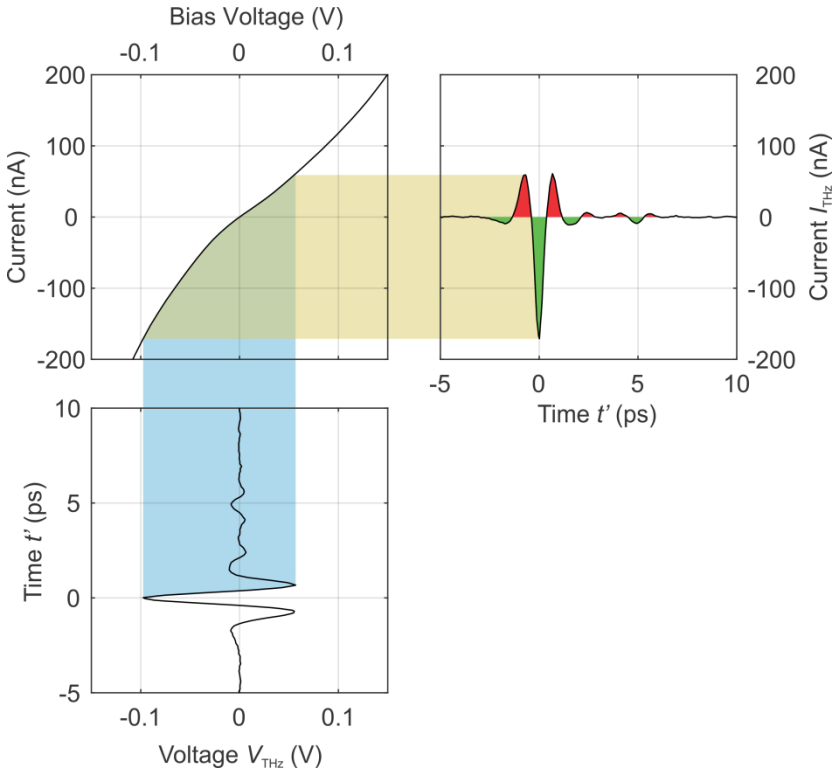

Figure 5.8 Illustration of the rectification process of the THz laser pulse induced voltage in the tunnel junction on 2H-$NbSe_2$. The time trace of the induced voltage $V_{\mathrm{THz}}(t')$ (at the bottom) is converted into a tunnel current pulse $I_{\mathrm{THz}}(t')$ (right) via the *I(V)* characteristic (shown in the center). (right) In the current pulse $I_{\mathrm{THz}}(t')$ the statistical contribution of electron tunneling from the sample in to the tip is marked green and the electron tunneling from tip into the sample is marked red.

spectrum by about −0.4 e^-/pulse. The offset decays for delay times between 1.2 ps and 3 ps and saturates at the base-line amplitude of −0.17 e^-/pulse. At this point different oscillations appear with magnitudes of up to 0.1 e^-/pulse, which vanish over a further delay time interval of 17 ps.

In section 4.5 of the previous chapter it was shown that the correlation spectrum of the two THz induced voltage pulses can already have a complicated shape without considering any sample dynamics. Understanding these static features is therefore important in order to identify dynamic effects in the recorded pump-probe spectrum. The correlation spectrum can be estimated based on the formalism presented in section 4.5 and the use of the *I(V)* spectra recorded on 2H-$NbSe_2$ (see **Figure 5.3**) scaled to the tunnel setpoint 1 nA at 1 mV, see **Figure 5.8**. Using this method, a THz induced voltage of −100 mV was found for a THz field amplitude of 130 V/cm by adjusting the THz-field-to-voltage conversion factor α such that the calculated rectified current $\bar{I}_{\mathrm{THz}}$ (equation 4.7) corresponds to a signal amplitude of −0.17 e^-/pulse. The induced voltage corresponds to an electric field of 1 MV/cm confined in the tunnel junction if the tip-sample distance is estimated to be 1 nm. The full correlation spectrum is then calculated with equation 4.8 and considering an on-and-off modulation of the probe pulse, see **Figure 5.9**a).

In **Figure 5.9**a) the calculated correlation function is directly compared to the recorded pump-probe spectrum. The comparison immediately makes it clear that any attempt to explain the observed pump-probe spectrum with only the correlation spectrum is insufficient. In order to understand the observed differences other effects must play an important role. Such effects are dynamics triggered by the pump pulse in the sample which lead to a time varying transient *I(V,t)*. Dynamic electronic phenomena in particular, such as a excited electron bath or collective CDW modes will directly influence the DOS under tip and will lead to a time varying *I(V,t)*. This results in the observed features which cannot be not be explained by the correlation spectrum.

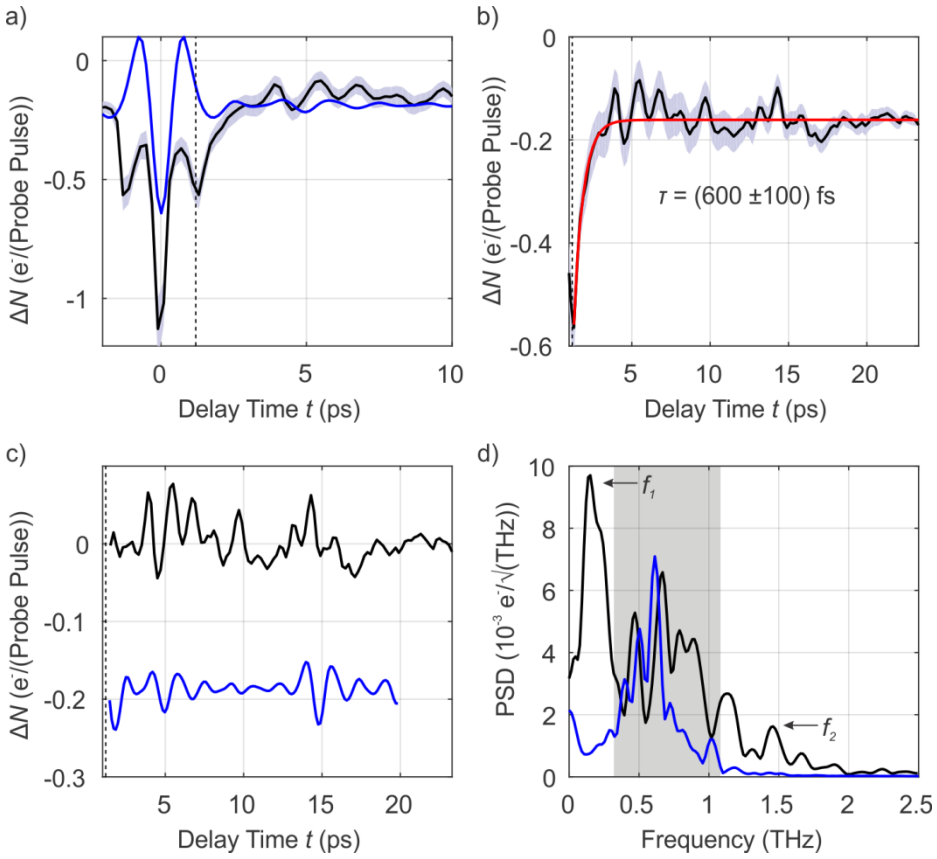

Figure 5.9 Further analysis of the pump-probe spectrum shown in **Figure 5.7**. (a) The calculated correlation spectrum (blue line). (b) Exponential fit to the *relaxation* region (red line) with a decay constant of τ = (600 ± 100) fs. (c) Residual r*elaxation* regime after subtraction of the exponential fit (black line) and correlation spectrum (blue line). (d) Power spectral density (PSD) of curves in (c). The grey interval is the interval with the most dominant frequency components of the correlation function. Outside this interval the PSD of the pump-probe spectra shows two further peaks (f_1, f_2).

The details of the differences between the recorded pump-probe and the calculated correlation spectrum are discussed in the following. For this discussion the delay times are separated phenomenologically into two regimes, see dotted lines in **Figure 5.9**(a–c). The delay time regime around zero is called the *excitation* regime. For delay times larger than 1.2 ps the two THz pulses become significantly separated and this regime is called the *relaxation* regime. In the *excitation* regime the pump-probe spectrum is dominated by the dip-structure. This dip-structure is also found in the correlation spectrum and is therefore an effect of the correlation of the two THz voltage pulses over the nonlinear *I(V)*.

Interestingly, the offset of the dip-structure and in particular the resulting decay in the *relaxation* regime observed in the pump-probe spectrum is not reproduced in the correlation spectrum. This strongly indicates that dynamics are being probed. In order to extract the time constant of the observed decay an exponential function ($a\, e^{-t/\tau} + b$) is fit to this part of the pump-probe spectrum. A decay constant of τ = (600 ± 100) fs is found, see **Figure 5.9**b).

The differences of the oscillatory features in the *relaxation* regime can be identified in the power spectral density (PSD) of the pump-probe and the correlation spectrum, see **Figure 5.9**c) and d). The PSD is calculated using a 15 ps wide hamming window and averaging over full *relaxation* regime. In addition, the decay was removed from the pump-probe-spectrum by subtracting the exponential fit prior the calculation of the PSD.

The PSD of the calculated correlation spectrum has it main weight in a frequency range from 0.32 THz to 1.08 THz. Features found in this frequency range in the PSD of the pump-probe spectrum presumably therefore results from the THz-pulse correlation and less likely from dynamics. Nevertheless, two further peaks are observable which are located at f_1 = 0.15 THz and f_2 = 1.46 THz and do not lie within the aforementioned frequency range. These oscillations can be attributed to dynamics.

This single pump-probe spectrum already contains a large amount of information including the appearance of a complex dynamic signal. However, the assignment of the different features to certain phenomena remains difficult at this point. Nevertheless some statements can be made:

- A dynamical response of 2H-$NbSe_2$ can be excited and probed with the THz-STM technique.
- A fast decay (600 fs) and oscillations at 0.15 THz and 1.46 THz can be linked to dynamics.
- The dynamics are excited and probed by voltage pulses on the order of 100 mV corresponding to an electric field of approximately 1 MV/cm in the junction.

- The signal current detected is so small that on average only 0.2 electrons are rectified per THz-pulse.

The last point deserves to be examined further, since it is an important hint, which helps the underlying mechanism of the pump-probe experiment to be understood. In the pump-probe spectrum shown, on average only 0.2 electrons are rectified during the probe pulse. That means that an electron will be rectified only once per five probe pulse , since electrons cannot be split. This consideration can also be extended to the pump pulse since the pump and probe pulses have approximately the same strength. By considering the experiment to only be sensitive to the events during which an electron is rectified at the probe pulse it becomes clear that only 1/5 of the signal stems from events during which an electron was also rectified during the pump pulse. While the rectified electrons are measurable, the corresponding total amount of electrons tunneling between tip and sample during the THz-voltage pulse is not. Nevertheless on an approximate level, the calculated transient current allows the statistical electron tunneling between tip and sample to be evaluated, see **Figure 5.8** (right panel). On this basis one finds that the 0.2 rectified electrons per pulse originate from 0.8 electrons tunneling statistically into the tip per pulse and 0.6 electrons tunneling out of the tip per pulse.

This evaluation points to two fascinating properties of the pump-probe spectrum recorded with the THz-STM. First, the measured signal results from a single electron tunneling during the probe pulse. Second, it appears that electron injection during the pump-pulse is not responsible for exciting dynamics since, statistically, less than one electron is tunneling per pulse. In fact the induction of the THz voltage itself gives a more plausible excitation mechanism as will be elaborated later in this chapter. The next section will elucidate these aspects further with pump-probe spectra recorded with heavily decreased electron tunneling rates.

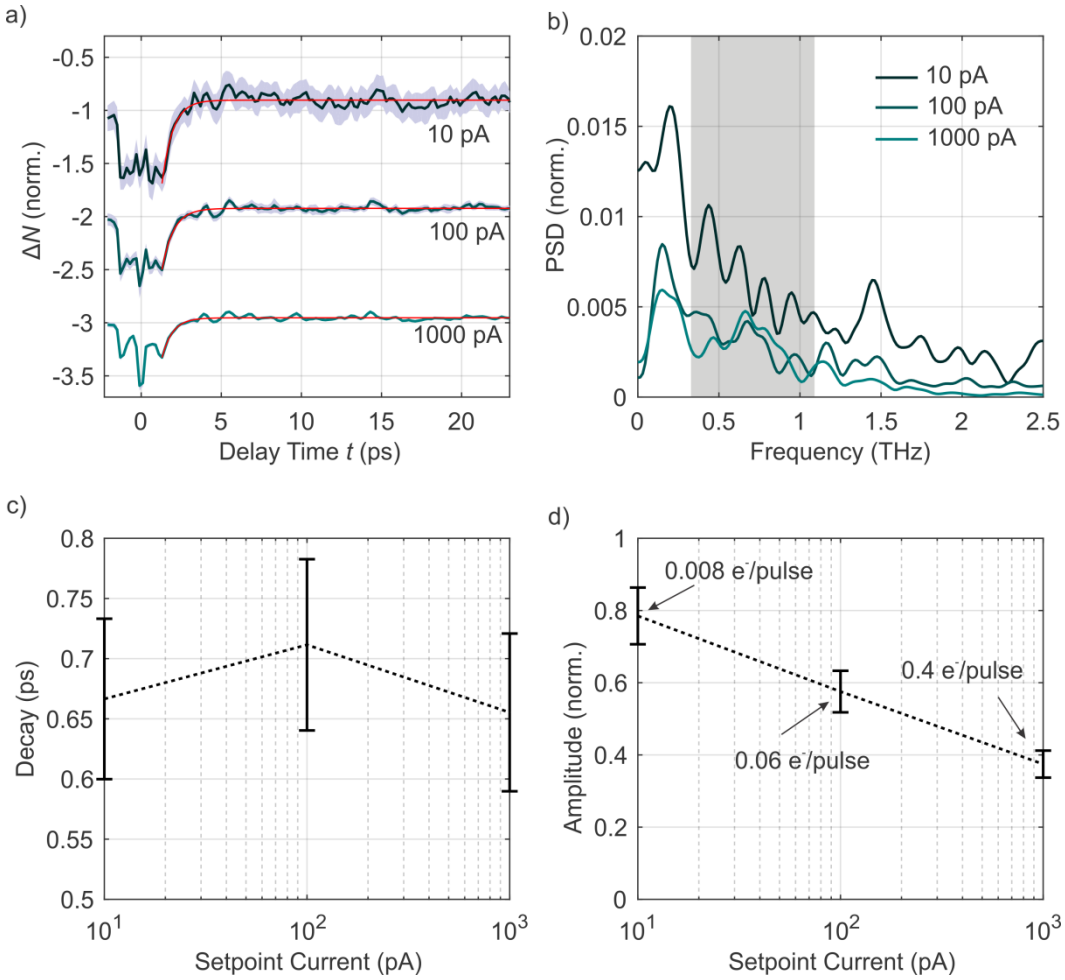

Figure 5.10 (a) Setpoint current dependence of the THz pump-probe spectra as a function of delay time recorded on 2H-$NbSe_2$ at 20 K, junction setpoint 1 nA, 100 pA and 10 pA at 1 mV (THz repetition rate: 40 MHz, pump strength: 130 V/cm, probe strength: 130 V/cm). The spectra are normalized by dividing them by their setpoint current and vertically shifted for better visibility. In the *relaxation* regime ($t > 1.2$ ps) an exponential fit was performed (red lines). (b) PSD of the normalized relaxation region with the exponential fit subtracted (grey area: frequency interval with largest contributions of the correlation spectrum, see **Figure 5.9**). (c-d) Decay constant and amplitude of the exponential fit as a function of the setpoint current. The amplitude magnitudes are also given in non-normalized units (electron per pulse).

5.5.1 Junction setpoint dependence

The following section discusses a series of pump-probe spectra recorded with different setpoint conductances, see **Figure 5.10**a). Three different junction setpoints: 1 nA, 100 pA, and 10 pA at 1 mV are used while keeping all other parameters constant.

An intriguing observation can be made regarding these pump-probe spectra when they are normalized by dividing them by their respective setpoint current. Surprisingly, normalization of the three spectra reveals that features such as the decay or the oscillations do not vanish when the setpoint current is reduced by a factor of 100. If these dynamic features are caused by electron tunneling during the pump pulse (ΔN_{ee}) then they should scale with the square of the setpoint current, $\Delta N_{ee} \sim (I_{\mathrm{set}})^2$, since they are also sensed by tunneled electrons. For that reason, these features should vanish in the normalized spectra for much reduced setpoint current,

$$\frac{\Delta N_{ee}}{I_{\mathrm{set}}} \xrightarrow[I_{\mathrm{set}} \to 0]{} 0 \,. \qquad 5.2$$

The fact that they remain clearly observable directly implies that the observable dynamic features cannot be caused by electron tunneling during the pump pulse.

In addition, the shape of the spectra shows changes for different setpoints. In the *excitation* regime the pronounced dip observed for large setpoint currents vanishes for small setpoint currents and instead small sharp peaks evolve. It is not possible to explain these changes based on the correlation spectrum since its shape is independent of the chosen setpoint current and remains as shown in **Figure 5.9**a). This is an indication that the appearance of sharp peaks is a direct signatures of the excitation process.

Setpoint dependent changes are also observed in the *relaxation* regime. Here, the changes can be quantified by the variation of the exponential fit and the magnitude of the oscillations, see **Figure 5.10**b), c) and d). While the decay time is constant for different setpoint currents, see **Figure 5.10**c), the normalized amplitude of the decay becomes significantly larger for smaller setpoint currents, see **Figure 5.10**d). The oscillatory features in the *relaxation* regime also increase with decreasing setpoint. They are identified by subtracting the exponential fit and then calculating PSD of the residual part, similar to **Figure 5.9**. The most significant changes in the PSD due to decreasing the setpoint current are a reduction of the relative contribution of components in the frequency window dominated by oscillation resulting from the correlation spectrum. On the other hand the peak at 0.15 THz in-

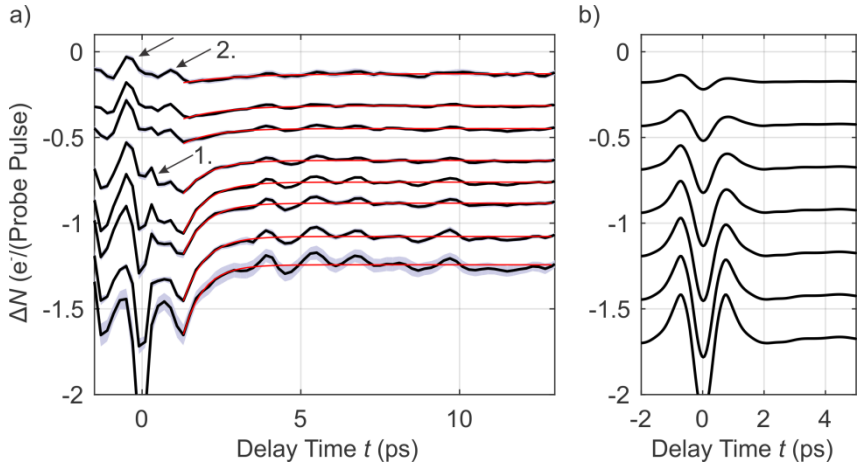

Figure 5.11 (a) Series pump-probe spectra recorded on 2H-$NbSe_2$ at 20 K as function of delay time with different pump-pulse-amplitudes (Junction setpoint 1 nA at +1 mV). The pump pulse amplitude ranges from 20 V/cm (top) to 130 V/cm (bottom) while all other parameters were kept constant (THz repetition rate: 40 MHz, probe strength: 130 V/cm). For better visibility the curves were offset. The two arrows (2.) indicate the anisotropy of the two side humps of the central dip. The arrow (1.) marks an additional peak at +0.3 ps delay time. The red lines are exponential fits to the *relaxation* regime. (b) Static estimate of the pump-probe spectra with sequentially reduced pump amplitude.

creases and at 1.46 THz a pronounced peak emerges. In the last section, these two features were attributed to dynamics.

The results of the junction setpoint dependence are counterintuitive. Features linked to dynamics become more pronounced for smaller setpoint currents. These features are the sharp peaks at zero delay time, the decay, and the oscillations at 0.15 THz and 1.46 THz. Pump-probe spectra recorded with large setpoint currents are more similar to the correlation spectrum while spectra record with small currents are dominated by dynamics-related feature. In conclusion, this shows that dynamics are not caused from electron injection during the pump pulse but on the contrary that stronger tunnel currents are invasive and suppress the dynamic signal.

5.5.2 Pump amplitude dependence

The setpoint current dependence measurements have shown that the system is not excited by a tunnel current during the pump-pulse. In order to clarify the origin of the

excitation the next part of the chapter discusses a series of pump-probe spectra in which the amplitude of the THz pump pulse was sequentially reduced while keeping the probe pulse constant, see **Figure 5.11**a). As discussed earlier, the peak THz field of the pump pulse is converted to the estimated peak voltage amplitude induced at the junction.

The shape of the *excitation* regime of the pump-probe spectra changes significantly; see **Figure 5.11**a). The dominant dip vanishes and an asymmetry forms when pump amplitudes are reduced. For the largest pump amplitude, when pump and probe are identical the two humps at the side of the dip have the same height. For smaller pump amplitudes the hump at $t > 0$ becomes less pronounced. An additional peak appears for intermediate pump amplitudes at a delay time of $t = +0.3$ ps.

Changes in the *excitation* regime can be discussed with respect to the correlation spectrum calculated at different pump-pulse amplitudes, see **Figure 5.11**b). While the vanishing dip at $t = 0$, as well as the asymmetry of the two side humps, is found in the correlation spectra, the additional peak at $t = +0.3$ ps is not. In fact, its appearance is similar to the peaks found in the low current pump-probe spectra (**Figure 5.10**) and is conclusively also a signature of the excitation process.

In the *relaxation* regime the changes are mostly connected to the decay behavior. By fitting an exponential function to the relaxation region of each spectrum the decay constant as well as the amplitude of the decay can be extracted, see **Figure 5.12**a) and b). The amplitude decreases almost linearly with decreasing pump strength. The decay constant increases for decreasing pump strength and exhibits a non-linear trend. The largest decay extracted is $\tau_{max} = (1.7 \pm 0.3)$ ps and the smallest is $\tau_{min} = (0.6 \pm 0.1)$ ps. It appears as if the trend of the decay constant saturates and approaches 610 fs asymptotically. Based on this estimation, the voltage at which the saturation becomes observable is 50 mV, i.e. 65 V/cm.

Further investigation of the oscillatory part of the pump-probe spectra is performed by analyzing the PSD of the *relaxation* regime, see **Figure 5.12c**). The PSD curves appear similar to the one reported earlier for high setpoint current, see **Figure 5.9**. Although some changes occur, there is no clear trend as a function of pump strength.

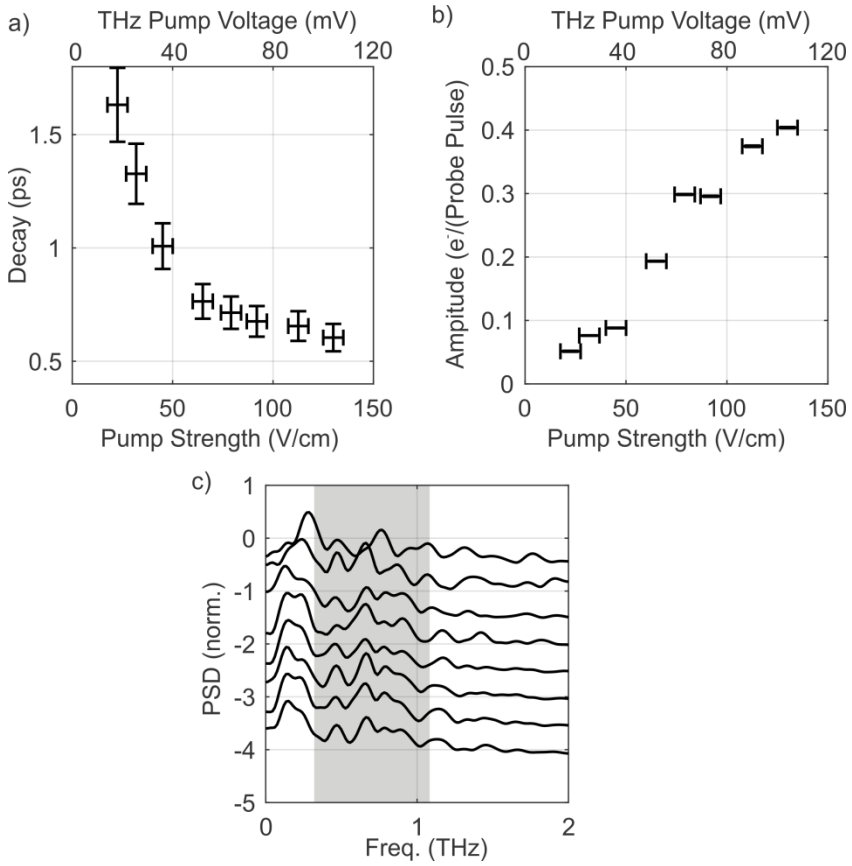

Figure 5.12 (a) Extracted decay constant of the exponential fits of **Figure 5.11** as a function of pump amplitude. (b) Extracted amplitude of the exponential fits of **Figure 5.11** as a function of the pump amplitude strength. (c) PSD of the relaxation regime after subtracting the exponential fit for different pump strength amplitude. Curves are normalized and shifted vertically with decreasing pump strength from bottom to top (grey area: frequency interval with largest contributions of the correlation spectrum, see **Figure 5.9**).

The observed changes of the pump amplitude dependent pump-probe spectra indicate that the more the system is driven out of equilibrium the faster it tends to relax back. The decay constant decreases for increasing pump strength and saturates. The following analysis of the experimental findings from the previous sections reveals that the measurement can be explained by an electronic excitation which is accompanied by the launch of collective modes of the CDW.

5.6 Interpretation of femtosecond spectroscopy

In the previous part the first results of femtosecond spectroscopy on 2H-$NbSe_2$ performed with the THz-STM were shown. In the next part an in depth analysis of the experimental results is presented, reveiling new aspects and allowing the interpretation to be put on a strong footing.

The discussion is structured in three parts. The first part is focused on the separation of the static and the dynamic contribution from the pump-probe signal. In the second part a possible excitation mechanism based on an in-plane screening current is presented. The information obtained in the first two parts provides a clear hint to the nature of the dynamics which are discussed in the third part.

5.6.1 Separation of the static and dynamic contributions

The appearance of the pump-probe spectra can be understood with dynamic and static features. Static features are those features which appear as if the sample system would not react to the presence of the THz voltage pulses. All other features are dynamic features. The separation of the pump-probe spectrum into a dynamic and a static contribution is in general possible without using any details of the experiment. A starting point for this separation is a generic transient $I(V,t')$:

$$I(V,t') = I_s(V) + I_d(V,t')\,, \tag{5.3}$$

where $I_s(V)$ is the static contribution and $I_d(V,t')$ is the dynamic contribution of the transient $I(V,t')$. This separation is, mathematically, always possible and is not an assumption. With this definition and according to section 4.2 this leads to a separation of the pump-probe signal $I_{PP}(t)$ into a static part and a dynamic contribution:

$$\begin{aligned} I_{PP}(t) &= \frac{1}{T}\int \mathrm{d}t' I(V_{THz}(t',t),t') \\ &= \frac{1}{T}\int \mathrm{d}t' I_s\big(V_{THz}(t',t)\big) + \frac{1}{T}\int \mathrm{d}t' I_d(V_{THz}(t',t),t') \\ &= I_{PP,s}(t) + I_{PP,d}(t) \end{aligned} \tag{5.4}$$

where $V_{THz}(t', t)$ is the voltage trace produced by the two THz-pulses as a function of time t' and time delay t between the two pulses. Although it is always possible to define the static and the dynamic pump-probe part, it is not possible to apply this formalism to the recorded data without any further assumptions.

As already mentioned in section 5.5, in order to show that the pump-probe signal has dynamical content, see **Figure 5.9** or **Figure 5.11**, a reasonable assumption which allows the dynamic contribution to be separated is to consider the calculated correlation spectrum as an estimate for the static pump-probe spectrum. However, the calculation of this estimate relies not only on a measured *I(V)* but also on a guess of the THz-shape and the rectification factor α, see equation 4.8. It is therefore necessary to experimentally verify this procedure by an independent approach.

It is possible to extract the static part $I_{PP,S}(t)$ from the setpoint current dependent measurements presented in **Figure 5.10**. For this approach less drastic assumptions suffice. The first assumption is that the static $I_S(V)$ is not affected by any current pumping effects and $I_S(V)$ can therefore be written as:

$$I_{S,I_{\mathrm{set}}}(V) = I_{\mathrm{set}}\, \tilde{I}_S(V)\,, \tag{5.5}$$

where $\tilde{I}_S(V)$ represent only the shape and is independent of the setpoint current I_{set}. In other words, the static $I_S(V)$ can be adjusted to a different setpoint current by a scaling factor. From here it follows that the static contribution $I_{PP,S}(t)$ can also be described by a setpoint independent shape $\tilde{I}_{PP,S}(t)$:

$$I_{PP,S,I_{\mathrm{set}}}(t) = I_{\mathrm{set}}\, \tilde{I}_{PP,S}(t) \tag{5.6}$$

Accordingly the normalized pump-probe spectrum $\hat{I}_{PP,I_{\mathrm{set}}}(t)$ has a static contribution which is independent of the setpoint current:

$$\hat{I}_{PP,I_{\mathrm{set}}}(t) = \frac{I_{PP,I_{\mathrm{set}}}(t)}{I_{\mathrm{set}}} = \tilde{I}_{PP,S}(V) + \frac{I_{PP,d,I_{\mathrm{set}}}(t)}{I_{\mathrm{set}}}\,. \tag{5.7}$$

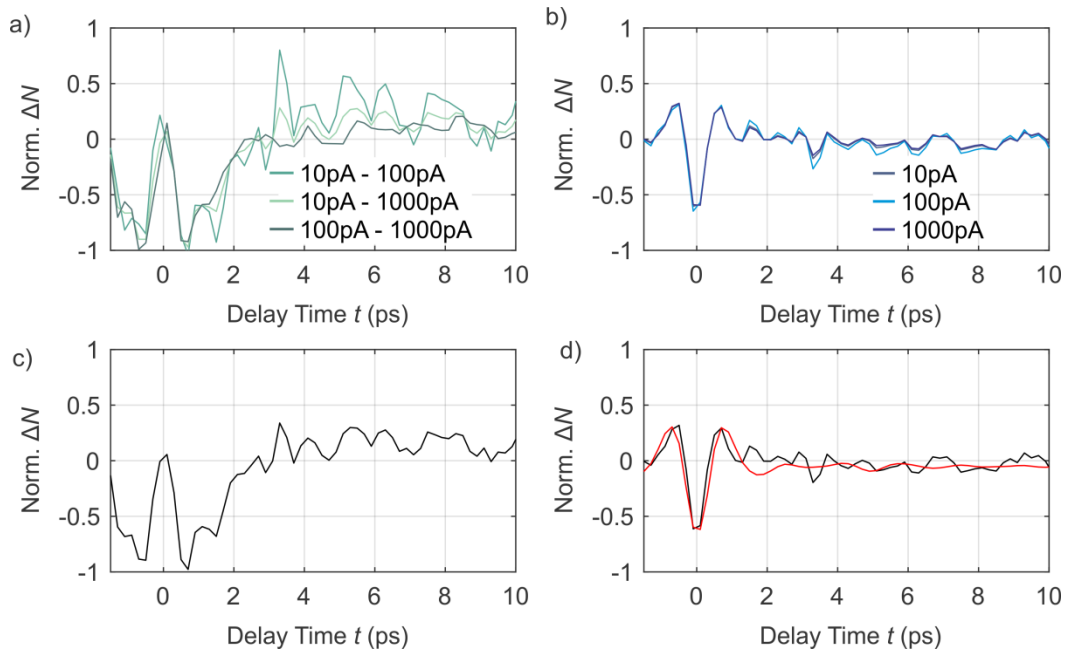

Figure 5.13 Analysis of the current pump-probe spectra in **Figure 5.10**, for details see main text. (a) The three normalized difference curves. (c) The mean of the normalized difference curves. (b) The calculated normalized static pump-probe contribution $\hat{I}_{PP,I_{\mathrm{set}}}(t)$ for each setpoint is calculated. (d) The mean of the static shape (black line) matches well with the correlation function (red line), which is calculated based on a recorded *I*(*V*) and the THz-pulse shape according to the *EO*-sampling signal and a peak voltage of −110 mV.

Subtracting the normalized setpoint current dependent pump-probe spectra from each other will result in curves comprised exclusively of the dynamic contribution:

$$\hat{I}_{PP,I_{\mathrm{set},1}}(t) - \hat{I}_{PP,I_{\mathrm{set}},2}(t) = \frac{I_{PP,d,I_{\mathrm{set}},1}(t)}{I_{\mathrm{set},1}} - \frac{I_{PP,d,I_{\mathrm{set}},2}(t)}{I_{\mathrm{set},2}}. \qquad 5.8$$

For the three pump-probe spectra of **Figure 5.10** all three difference curves were computed. The overall shape of the resulting curves is very similar and, although differences in the oscillatory behavior are present, the main differences can be accounted for by considering constant multiplication factors. This leads to the second assumption that the dynamic contribution $\hat{I}_{PP\,,d,I_{\mathrm{set}}}(t)$ has a setpoint current independent shape:

$$I_{PP,d,I_{\mathrm{set}}}(t) = I_{\mathrm{set}}\, A(I_{\mathrm{set}})\tilde{I}_{PP,d}(t). \qquad 5.9$$

The weight factors $A(I_{\mathrm{set}})$, see **Table 5.1**, and the setpoint current independent shape $\tilde{I}_{PP,d}(t)$ can be determined directly from the difference curves, see **Figure 5.13**a) and c).

$\boldsymbol{I_{\mathrm{set}}}$	1000 pA	100pA	10pA
$\boldsymbol{A(I_{\mathrm{set}})}$	(0.5 ± 0.01)	(0.8 ± 0.02)	1 (fixed)

Table 5.1

Based on this knowledge the static contribution $\tilde{I}_{PP,s}(t)$ can also be computed directly. Indeed for all three measurements the same curve is found, see **Figure 5.13**b). The experimentally obtained $\tilde{I}_{PP,s}(t)$ can be compared directly with the correlation spectrum showing remarkable agreement, **Figure 5.13**d). This means that the calculated correlation spectrum is indeed the static contribution of the pump-probe spectrum and justifies the analysis made in section 5.5.

On the other hand, this approach allows the observed exponential feature to be clearly identified as a dynamical relaxation, and sheds some light on the excitation dynamics. The shape of the dynamic contribution $\tilde{I}_{PP,d}(t)$ shows the evolution of the excitation of the system. Starting from zero time delay the dynamic contribution reaches its largest magnitude at ±700 fs. This delay indicates that the system needs approximately 700 fs to be driven into the excited state.

In order to evaluate the result of this analysis it is important to be aware of some limitations. In this approach, part of the normalized dynamical contribution does not change with the setpoint current, which can be present in the experimental data, and be spuriously accounted for as part of the static contribution. Although the good agreement observed in **Figure 5.13**d) suggests that such spurious effects do not play a major role, it can be responsible for the small oscillatory features observed in the *relaxation* regime. For this reason, the extrapolated dynamic contribution will not be used to directly gain more insight into the frequency domain.

The separation of static and dynamic contributions also helps to clarify the appearance of the additional peaks in the pump-probe spectra during the *excitation* regime, as shown in

Figure 5.10 and in **Figure 5.11**. These peaks simply result from the linear combination of the static and the dynamic part.

Another substantial observation is that the pre-factors $A(I_{\mathrm{set}})$ decrease with increasing setpoint current and are directly proportional to the amplitude of the relaxation found in **Figure 5.10**d). This strongly supports the finding that for large setpoint currents the measurement of dynamics is suppressed. The fewer electrons tunnel, the larger the contribution of electrons probing the dynamics will be. This is a captivating finding since the tunnel conductance for these measurements was so small that the probability of a single tunnel event during a pulse was much smaller than one. Two different explanations are plausible: If an electron tunnels during the pump pulse …

- the tunneling of a second electron during the probe pulse is suppressed when the delay is less than a few picoseconds, similar to a coulomb blockade effect [WBJJ89, AFJ93], or
- the dynamics of the system become suppressed by the injected electron.

5.6.2 Excitation mechanism

The separation of the pump-probe spectra clearly reveals the probed dynamics. However, their excitation mechanism remains unknown. Nevertheless, the experiment excludes the possibility that the tunnel current during the pump pulse is triggering the dynamics. The coupled THz-pluses have to affect the system by another mechanism. This mechanism is less sensitive to the tip-sample distance then the tunnel current but still depends on the pump-amplitude, since the excitation strength basically remains constant for different setpoint currents but changes when the THz-amplitude is altered. The electric field induced inside the tunnel junction by the THz-pulses can cause an excitation scheme that satisfies such requirements. This can be understood when the full THz-pulse coupling and voltage induction mechanism is reconsidered.

In the simplest approach, a coupled THz-pulse has the primary effect of shifting charges at the tip apex. The charges generate an electric field around the tip apex that is very strong because of the tip geometry. In contrast to the tunnel current, this process, mediat-

ed by the electric field, is almost insensitive to the tip-sample gap as long as they are in the tunneling regime. The surface of 2H-$NbSe_2$ screens this electric field and confines it inside the junction between tip and sample, which results in the voltage between tip and sample. For this screening, free carriers in the 2H-$NbSe_2$ surface must generate a surface charge. Although this surface charge is also present for a conventional applied voltage an important difference is that, in this case, the resulting field oscillates with THz frequencies. The reaction of the surface charge to the oscillating field leads to an alternating current inside the 2H-$NbSe_2$ sample.

As will be described below, the resulting alternating current can be estimated and reach magnitudes large enough to drive the system out of equilibrium. In contrast to a tunnel current the screening current flows on a length scale comparable to the radius of the tip apex which is typically tens to hundreds of nanometers and the system is excited on a similar length scale.

The alternating current $\vec{j}(\vec{r}, t')$ can be estimated from the time varying charge distribution

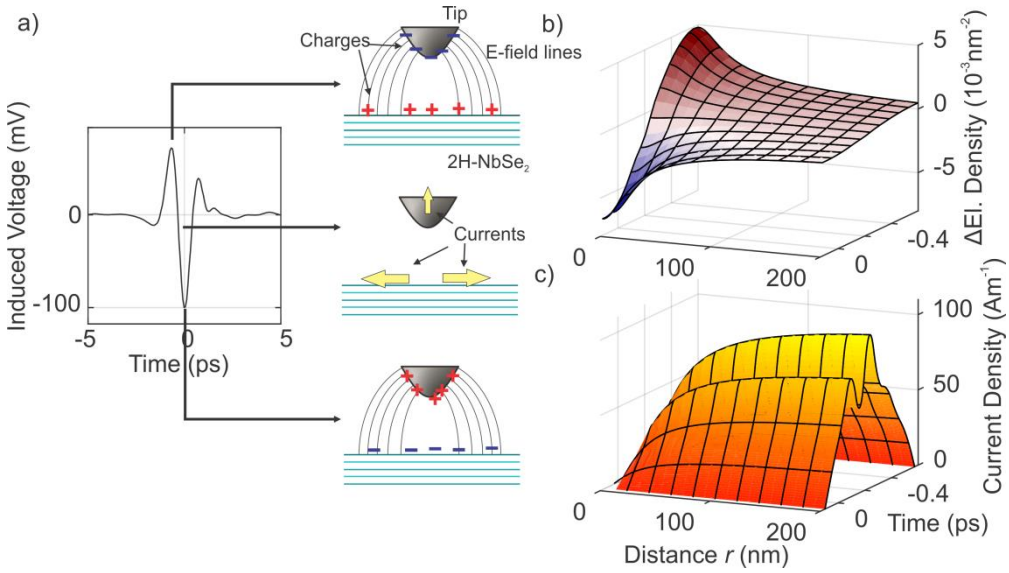

Figure 5.14 (a) Sketch of the presumed excitation mechanism. The time varied THz induced voltage is accompanied with a varying surface screening charge. Varying charges lead to a current which dominantly flows in the first $NbSe_2$ layer since the inter layer resistance is high. (b) Calculated screening excess electron density and (c) current density at the 2H-$NbSe_2$ surface as a function of time and distance to the tip apex based on the model explained in the main text.

$\rho(\vec{r},t)$ at the 2H-$NbSe_2$ surface. For the approximation of the charge distribution $\rho(\vec{r},t)$ it will be assumed that the electric field $E(\vec{r},t')$ between tip and sample surface is completely screened for all times (quasi static) and that the charge distribution is restricted to the surface which lies in the xy plane at z = 0, $\rho(\vec{r},t') = \sigma(\vec{r},t')\,\delta(z)$. This assumption is reasonable since 2H-$NbSe_2$ remains mostly metallic since a CDW gap only opens in a small fraction of the band structure. Due to the metallic part of the band-structure 2H-$NbSe_2$ exhibit a plasma frequency of 240 THz at low temperatures which is sufficient to screen electric fields basically instantaneously for the time scales considered here [DBD+03].

Then, for a given potential difference between the tip and the sample and a given geometry the resulting surface charge distribution $\sigma(\vec{r},t)$ can be calculated by the Poisson equation: $\vec{\nabla}^2\phi(\vec{r},t') = -\frac{\rho(\vec{r},t')}{\varepsilon_0}$, where ε_0 is the vacuum permittivity. The potential difference is nothing else but the induced THz voltage $V_{THz}(t')$. For simplicity a hyperbolic tip geometry was chosen to relate the voltage to the electric field [Fee03]. Under the assumption that the current is only flowing in the first layer of 2H-$NbSe_2$, which is justified by the much larger inter-layer residence [EF71, LN10], the current can be directly computed using the continuity equation:

$$\frac{\mathrm{d}\rho(\vec{r},t')}{\mathrm{d}t} + \vec{\nabla}\cdot\,\vec{j}(\vec{r},t') = 0. \qquad 5.10$$

Based on this model the surface charge density $\sigma(\vec{r},t')$ and the current density $\vec{j}(\vec{r},t')$ were calculated, see **Figure 5.14**. The calculation results in surface current densities up to 150 Am^{-1} in the vicinity of the STM tip. Considering the thickness of one 2H-$NbSe_2$ layer, 0.6 nm, this strength corresponds to a volume current density of 1.7 10^7 Acm^{-2}. This strong screening current density will certainly affect the metallic part of electronic system which carries it by heating [LHT+12, TBT12]. Although this current will most likely being carried by the CDW, the heating of the electronic system results in a cascade of effects which will also perturb the CDW. This is discussed in the next section.

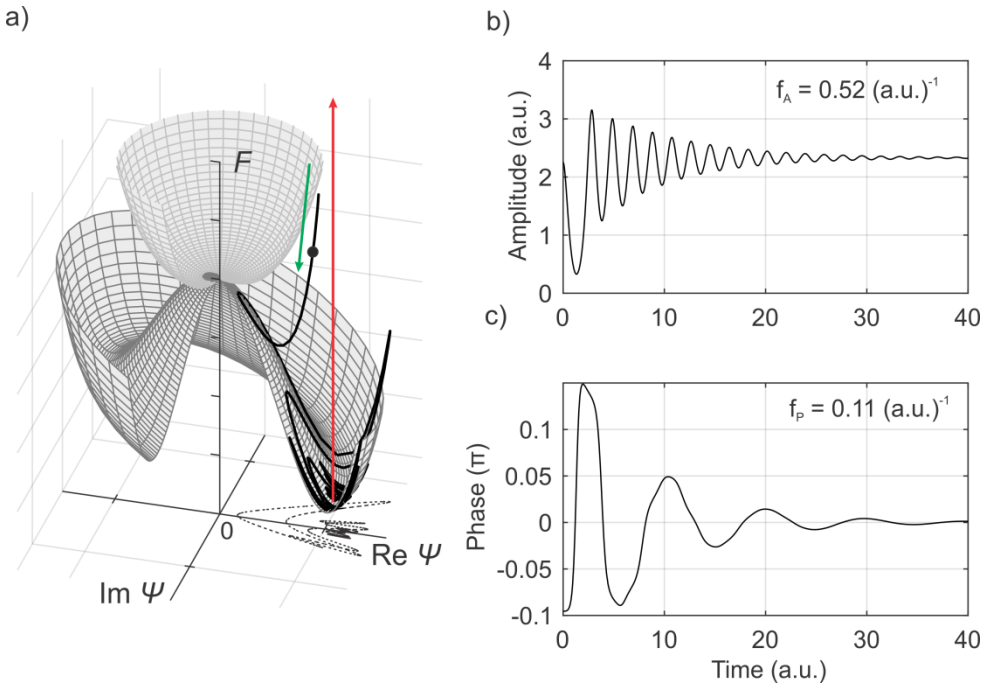

Figure 5.15 Schematic picture of the CDW excitation and relaxation process based on a simple Landau model. a) The *U*-shaped free energy potential of the order parameter of the excited system relaxes quickly back into the *Mexican-hat*-shape. Black line is the resulting trajectory of a complex order parameter Ψ in this changing free energy potential. Red arrow indicates the instant excitation process and the green arrow indicates the direction of the relaxation. b) Amplitude of the order parameter as function of time. c) Phase of the order parameter as function of time. For both panels the dominant oscillation frequency is indicated.

5.6.3 Nature of the dynamic signal

As discussed in the previous section, the most likely origin of the excitation is related to THz-induced in-plane screening currents. This excitation shakes the free energy landscape of the CDW order parameter leading to the launch of collective modes [LGP+13, TMB+13]. A simple picture of this excitation and relaxation process in a CDW system based on Landau theory [SN86] is illustrated in **Figure 5.15**. A more detailed explanation is given in supplement section 6.3. The sequence of excitation and relaxations of the electronic system, such as heating and collective modes, will influence the electron density under the STM tip, whether by broadening of the electron distribution or by altering the CDW modulation, see **Figure 2.3** and **Figure 5.4**. The tunnel current is sensitive to

changes in the electron density which then results in a transient $I(V, t')$. Probed by the probe THz pulse this leads to the observed dynamic features:

- Excitation process in the first 700 fs;
- Exponential decay process with a decay constant as small as 600 fs;
- 0.15 THz oscillation;
- 1.46 THz oscillation;

According to the interpretation presented, the excitation process and the exponential decay can be attributed to be signatures of the heated electronic system. For such excited systems it would be reasonable to relax more rapidly the stronger it is excited, analogous to hot electrons [EPCR00] and a similar behavior of a CDW was just reported recently [FHW+17]. Indeed, this behavior is found in the pump amplitude dependent measurements, giving strong support for this interpretation, see section 5.5.2. The residual oscillations most likely originate from collective modes of the CDW state.

Comparing the observed dominant frequency components with literature, it is reasonable to assign the 0.15 THz and 1.46 THz frequencies to the *phase* and the *amplitude* mode respectively. The frequency attributed to the *amplitude* mode matches to the frequency found with Raman spectroscopy [MGC+14]. To the best of our knowledge, the experimental observation of the phase mode of 2H-$NbSe_2$ has not yet been reported. However, a frequency similar to the 0.15 THz found here has been reported to be the *phase* mode of the CDW system $La_{(2-x)}Sr_xCuO_4$ [STH06].

Although the comparison of the detected frequencies is natural, the techniques conventionally used to detect the dynamic response of complex matter are usually restricted to certain optical selection rules. However, the pump-probe experiments performed with the THz-STM are not in principle restricted by the same selection rules since the excitation field stems from the STM tip, a very local source with a complex shape. Silent optical modes could therefore appear as fluctuations of non-linear components of the transient $I(V, t')$. It is thus possible that the other observed frequencies could stem from other CDW modes not observable by optical methods.

5.6.4 Additional contributions to the dynamic signal

The explanation given here is a first approach toward the understanding of the pump-probe signal. In the time regime of picoseconds of femtoseconds many dynamics of condensed matter can be present in addition to electronic one such as, for example, lattice vibrations.

It is therefore also conceivable that phonons contribute to the observed features in the pump-probe signal since in principle lattice vibrations can alter the tip-sample distance. Raman spectroscopy shows that inter-layer phonon modes can have THz frequencies similar to some observed by THz-STM pump-probe spectroscopy [HvBY+16, STH+16, XZW+15]. For example, shear modes at 1.17 THz and breathing modes at much softer 0.075 THz are observed in 15 monolayer thick 2H-$NbSe_2$ specimen [HvBY+16].

5.7 Spatial variation

So far the pump-probe spectra were only discussed as function of delay time but, in great contrast to other time resolved measurements, the THz-STM is a local probe. For the first time, this opens the possibility of investigating fast dynamics as a function of atomic position on the surface. In this last section of the thesis two different measurements showing the spatial dependence of the pump-probe signal are presented.

5.7.1 Topography of THz pump-probe signal

In this section the spatial distribution of the dynamic response is explored. A constant current topography will be discussed during which the pump-probe signal $\Delta N(t_{fix})$ at a fixed delay time was recorded simultaneously. Based on the previous results the pump-probe signal map $\Delta N(x,y,t_{fix,})$ was recorded with a reduced pump amplitude of around 60 mV (75 V/cm). At these parameters a peak attributed to the excitation process was detected, see **Figure 5.11**. The time delay was fixed to the additional peak $t_{fix,} = t_{peak} = +0.3$ ps, since here the dynamic feature will have a significant contribution to the recorded signal.

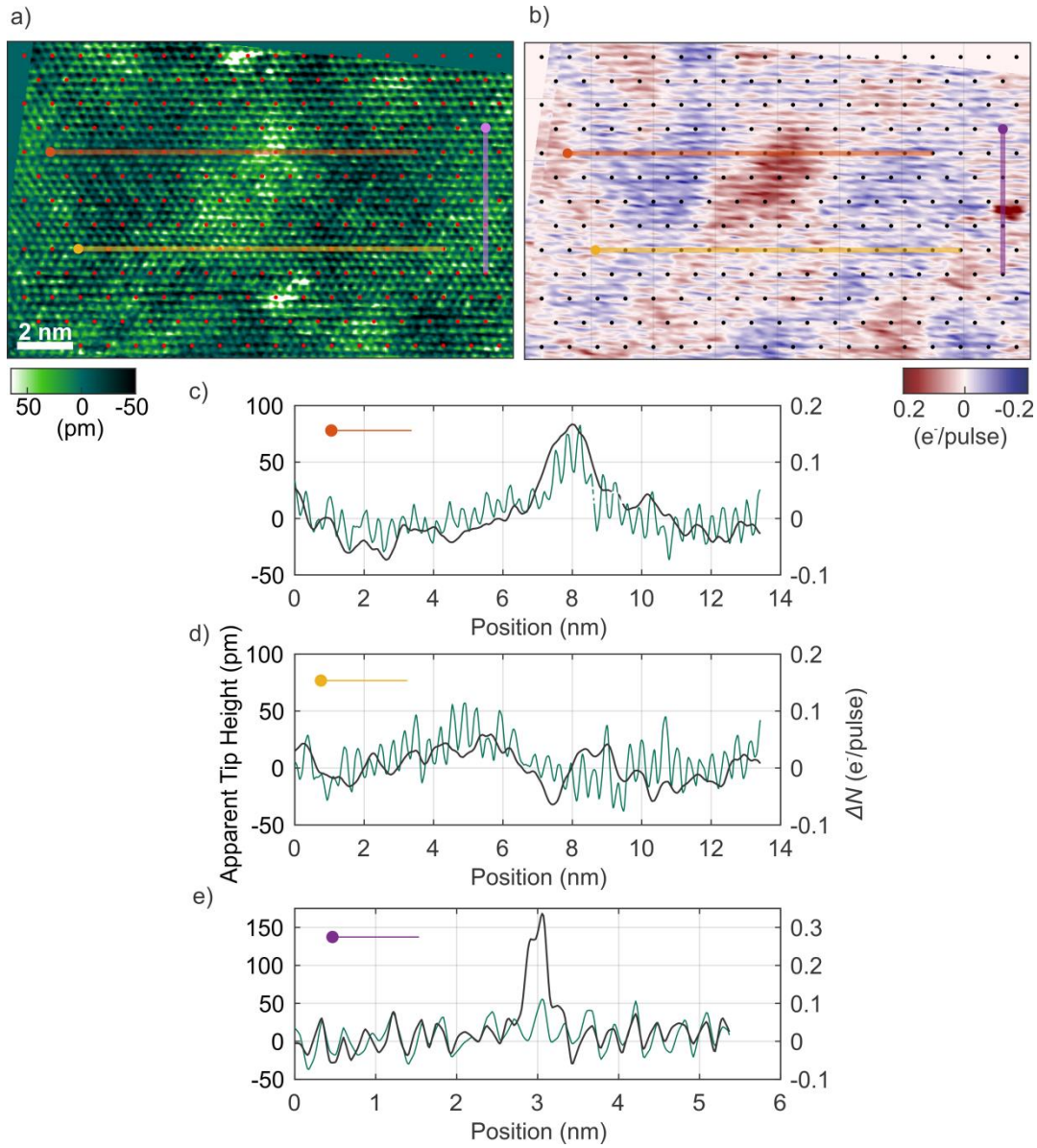

Figure 5.16 Simultaneous recording of (a) constant current topography and (b) THz pump-probe signal at a fixes delay (Junction setpoint 1 nA and 1 mV). The 3x3 unit cell of the CDW is indicated with points on top of the two maps. (c-e) Three cross-sections plotted as function of position. (tip height: green, pump-probe signal: black). The position and the direction of the cross-sections in the maps are marked with colored lines, a dot marks zero position.

In **Figure 5.16** the recorded pump-probe signal map $\Delta N(x,y,t_{peak})$ and the corresponding constant current topography $z(x,y)$ are shown. In contrast to the topography in the beginning of this chapter, here the 2H-$NbSe_2$ exhibits a larger amount of defects. The large topographic contrast of the defects itself causes the CDW to appear less pronounced. Still,

on the defect-free sections of the topography the CDW corrugation can be clearly observed.

The simultaneously recorded pump-probe map $\Delta N(x,y,t_{peak})$ shows reproducible variations with tip position on different length scales ranging from long-range fluctuation on the 5 nm scale to short-range on a single-atom scale. The signal ranges from -0.28 to +0.37 electrons per probe pulse. It is important to note that the signal changes not only in magnitude but also in sign. Comparison of pump-probe signal with the topographic height reveals that the constant current topography and pump-probe signal map are correlated. When the apparent tip height is larger, the pump-probe signal is more positive. This correlation is clearly shown in a cross-section through the central defect of the map, see **Figure 5.16**c) (top panel).There are however deviations from this general correlation and, at some local defects, topographic height and pump-probe signal do not match. Two further cross-sections show these deviations **Figure 5.16**d) and e). In **Figure 5.16**e) at 3 nm the pump-probe signal shows a strong peak which is not found in the topography and in **Figure 5.16**d) at 7 nm the pump-probe signal exhibits an additional dip.

Another observation is that the pump-probe signal is not just sensitive to variation on the nanometer scale but also down to the single atom. In fact, the horizontal lines visible in the THz signal map originate from the atomic lattice, as shown in the horizontal cross-section in **Figure 5.16**d). The atomic modulation in the other lattice directions is less dominant since these directions are more parallel to the *fast* scan axis of the STM and therefore averaged out by the finite Lock-In integration constant. This observation proves that the pump-probe current is sensitive on the atomic scale.

The correlation between constant current and pump-probe topography is not surprising, since both measurements are sensitive to the local density of states. The increased density is leading to a larger tunnel rate which will be compensated by moving the tip out and this static effect would also affect the pump-probe signal. However, it cannot explain the observed deviations at some defects of topography, as well as the sign change of the THz signal. For the interpretation of the pump-probe signal map the dynamic response of the

system has to be considered. This leads to the conclusion that defects do indeed modify the dynamical response of 2H-$NbSe_2$ on the nanometer scale.

5.7.2 High quality spectra at two different position

Instead of a map at a single delay time, two high quality pump-probe spectra recorded *on* and *off* an atomic defect are presented, see **Figure 5.17**. These spectra allow a detailed comparison of the pump-probe signal recorded at different positions.

In contrast to most THz-pump-probe spectra shown so far the spectra reported here do not show a dominant dip in the *excitation* regime, see **Figure 5.17**a)**.** Instead, they both exhibit a peak at zero delay time, which is more pronounced for the spectra recorded *off*-defect. The peak at zero delay is followed by a second peak/shoulder at +0.6 ps. While the main peak can be attributed to the excitation of the system the peak/shoulder is a static

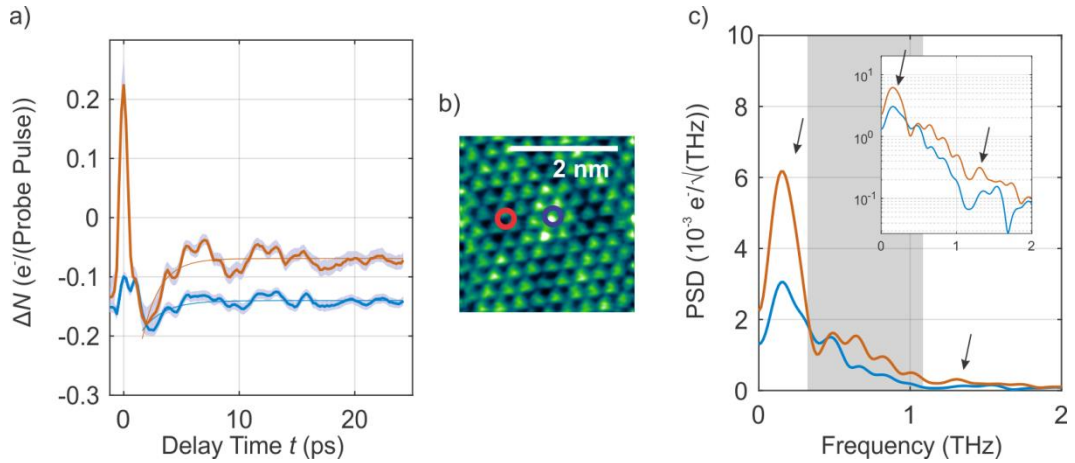

Figure 5.17 (a) THz pump-probe spectra recorded *off* (red) and *on* (blue) an atomic defect on 2H-$NbSe_2$ at 20 K (junction setpoint: at 1 nA at 1 mV, THz repetition rate: 40 MHz, pump strength: 130 V/cm, probe strength: 130 V/cm). Tip positions are marked in the constant height topography (b). Corresponding to the previous spectra exponential functions were fit to the *relaxation* part (starting at a delay time of +1.2 ps). Decay constant $\tau_{off} = (1.8 \pm 0.2)$ ps and $\tau_{on} = (2.3 \pm 0.2)$ ps are found *off*-defect and *on*-defect, respectively. (c) Corresponding PSD of the *relaxation* regime after subtraction of exponential fit (red: *off*-defect, blue: *on*-defect, grey area: frequency interval with largest contributions of the correlation spectrum, see **Figure 5.9**, inset: PSD curves with logarithmic scaling). Arrows mark peaks at 0.16 THz and 1.3 THz in the *off*-defect PSD which can be linked to the *phase* and *amplitude* of the CDW, respectively.

feature and is the residuum of the previously occurring dip-structure in accordance to the separation method (see section 5.6.1) of the static and dynamic pump-probe spectra.

The exponential decay during the *relaxation* is also less pronounced. For the spectra recorded *on*-defect the decay is almost not visible. Nevertheless, an exponential function can be used to fit the two curves. Decay constants of $\tau_{off} = (1.8 \pm 0.2)$ ps and $\tau_{on} = (2.3 \pm 0.2)$ ps are found for the spectra *off*-defect and *on*-defect respectively. The amplitude of the decay is (0.05 ± 0.01) e^-/pulse *on*-defect and (0.14 ± 0.1) e^-/pulse *off*-defect. A further difference between the two spectra is that the baseline of the *on*-defect spectrum is twice as negative (-0.14 e^-/pulse) as the one recorded *off*-defect (-0.07 e^-/pulse). In total these observations match to the properties of a weakly pumped system below the saturation as shown in **Figure 5.11** for the pump dependence measurements. It should be noted that, in contrast to all previous presented THz pump-probe measurements these pump-probe spectra were recorded with a different 2H-$NbSe_2$ sample (from the same batch) and a different tip. This resulted in a less effective THz coupling and makes a direct comparison to the previous measurements non trivial.

In the PSD of the residual *relaxation* regime (with subtracted exponential fit), the frequencies around 0.16 THz have the largest contributions. These frequencies were previously attributed to the *phase* mode of the CDW **Figure 5.17**b). Although this dominant peak is located at the same frequency for both spectra, the overall shapes of the PSD show significant differences that cannot be explained simply by a scaling factor. This indicates a position dependent PSD for the dynamics involved. Not only is the 0.16 THz peak strongly reduced *on*-defect, at 1.3 THz an increased signal contribution can be detected *off*-defect which is not present *on*-defect. In agreement with the previous results this is a sign of an *amplitude* mode which cannot be observed on the defect itself.

In conclusion, the dynamic feature such as the excitation-peak, the decay and the oscillations are weaker *on*-defect and the system appears less disturbed in comparison to a position only a nanometer away. This is in agreement with the observation made with the pump-probe signal map (**Figure 5.16**) and can be explained by a pinning potential locking the CDW at the defect. The strength of the pinning potential could, in particular, protect

the CDW from being excited and hinders the launch of collective modes while only a nanometer away from the defect position the collective mode can form.

5.8 Conclusion

In this chapter the dynamic properties of 2H-$NbSe_2$ in its CDW state were investigated with THz-STM allowing femtosecond time resolution on the atomic scale. The dynamic measurements presented here are the first of their kind. A sophisticated analysis was performed to disentangle the dynamic information. Electron-injection was experimentally excluded as a cause for the excitation, instead a mechanism based on fast oscillating in-plane currents screening the THz induced voltages was found. The analysis allowed the clear identification of different dynamical processes such as the heating of the electronic bath as well as the collective *amplitude* and *phase* mode of the CDW.

The position-resolved measurement sets have proven that the dynamics of the 2H-$NbSe_2$ surface are significantly altered on the atomic scale and that the changes occurring can be

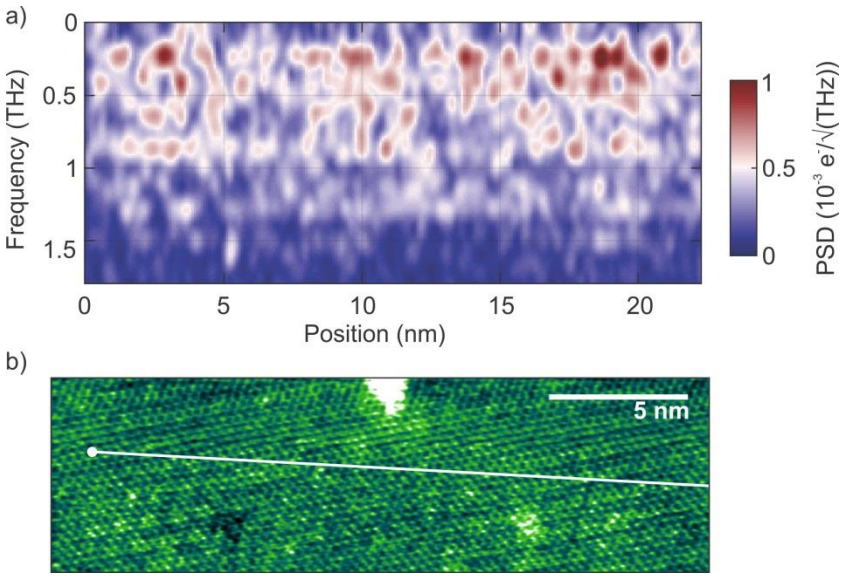

Figure 5.18 (a) Filtered power spectral density of the relaxation region of a pump-probe line scan as function of frequency and tip position on 2H-$NbSe_2$ at 20 K (junction setpoint: at 140 nA at 1+0 mV, THz repetition rate: 40 MHz, pump strength: 130 V/cm, probe strength: 130 V/cm). (b) Constant current topography recorded after the line scan. White line is route of the line scan and the dot marks the zero position.

observed with the THz-STM technique. A continuation of the investigation of the CDW state of 2H-$NbSe_2$ with THz-STM on the basis of the results of this thesis will hopefully provide a more detailed understanding of the direct effect of specific defects on the dynamics. Pump-probe spectra recorded as function of time and space and the spectral analysis thereof is a promising measurement avenue. Such recording was already tested preliminary in the progress of this thesis, see **Figure 5.18**. In order to fully understand this kind of data on a theoretical basis, approaches will be necessary which explicitly account for the spatially dependent and time resolved spectral density.

2H-$NbSe_2$ was just the first sample system investigated with the new THz-STM. The fascinating results obtained show the impressive potential of this new THz-STM instrument. The results of this thesis open a new view on the properties of complex materials and it would come as no surprise if other CDW or high-T_c superconducting systems showed similarly interesting results.

Chapter 6 Supplement

The *supplement* chapter gives additional information to specific parts of the thesis.

6.1 Chapter 3 - Fitting routine

In this section the fitting routine for the rate equation model described in the third chapter is explained and the resulting parameters are listed (**Table 6.1**). The routine is based on a least squares method. An error function $E(\boldsymbol{P})$ was minimized with respect to the parameter set $\boldsymbol{P}$. The error function was defined as follows:

$$E(\boldsymbol{P}) = \sum_{\sigma_{\mathrm{set}}} \int_{-15\mathrm{mV}}^{+15\mathrm{mV}} \mathrm{d}V \frac{\left(\frac{\mathrm{d}I}{\mathrm{d}V}_{\mathrm{exp},\sigma_{\mathrm{set}}} - \frac{\mathrm{d}I}{\mathrm{d}V}(\boldsymbol{P})_{\mathrm{sim},\sigma_{\mathrm{set}}}\right)^2}{{\sigma_{\mathrm{set}}}^2},$$

where $\frac{\mathrm{d}I}{\mathrm{d}V}_{\mathrm{exp},\sigma_{\mathrm{set}}}$ is the experimental dI/dV spectrum recorded at the tunnel setpoint σ_{set} (referring to +15 mV) and $\frac{\mathrm{d}I}{\mathrm{d}V}(\boldsymbol{P})_{\mathrm{sim},\sigma_{\mathrm{set}}}$ is the calculated dI/dV spectrum at the given setpoint for the parameter set $\boldsymbol{P}$.

In total 24 different setpoint values σ_{set} are used to fit the parameter set $\boldsymbol{P}$. Only the coupling strength between tip and Cu-substrate $G_{st}(=G_{ts})$, the tip-tip coupling G_{tt} and the tip interaction J_t change with respect on the given setpoint since they dependent directly on the tip-sample distance. All other model parameters were assigned as material properties and therefore kept constant for each setpoint. At each setpoint the tip interaction was approximated by:

$$J_{\mathrm{t}} = A\left(\frac{\sigma_{\mathrm{set}}}{\sigma_0}\right)^{\chi},$$

where $\sigma_0 = 0.433$ µS. A and χ are free parameters. This functional form is a valid assumption regarding the magnetic interaction between tip and sample [WBT+91, KSW07] and

reduces drastically the number of fit parameters. The tip-tip coupling G_{tt} was assumed to be half of G_{st} ($G_{tt} = 0.5\, G_{st}$). The coupling strength between tip and Cu-substrate was fixed by adjusting the model current $I(15\text{ mV}, G_{\text{st}})_{\text{sim},\sigma_{\text{set}}}$ to the setpoint:

$$I(15\text{ mV}, G_{\text{st}})_{\text{sim},\sigma_{\text{set}}} \stackrel{!}{=} \sigma_{\text{set}} \cdot 15\text{ mV}.$$

This approach allowed the parameter set $\boldsymbol{P}$ to be defined independently of the setpoint σ_{set}. The complete parameter set including the values minimizing the error function are listed in **Table 6.1**.

Parameter	**Best fit values**
D_1, D_2, D_3 (meV) *	(−1.88±0.02), (−2.42±0.01), (−1.87±0.02)
E_1, E_2, E_3 (meV) *	(0.39±0.01), (0.20±0.05), (0.31±0.02)
J_{12}, J_{23} (meV) *	(0.71±0.02), (0.66±0.01)
η *	(0.58±0.06)
u *	(1.1±0.3)
G_{ss} (μS) *	(2.6±0.9)
A (T) *	(−0.95±0.05)
χ *	(1.1±0.1)
S_1, S_2, S_3	2 ,2 ,2
T (K)	0.5
B (T)	(0, 0, 1)
g_1, g_2, g_3	2.1, 2.1, 2.1 [YCB+15b]

Table 6.1 The parameter set $\boldsymbol{P}$ used in the manuscript. Fitted parameters are marked with a (*). The table also includes the optimized values of the fit parameters and their error.

6.2 Chapter 4

6.2.1 Mechanical stability and vibration analysis of THz-STM

In this section different mechanical tests and an analysis of the noise performance of the THz-STM are presented. In the first test the mechanical resonances of the homebuilt STM head were investigated. The STM head was designed to only exhibit mechanical res-

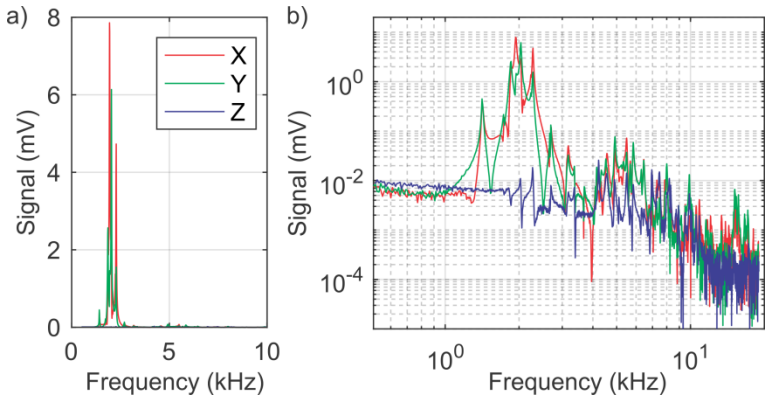

Figure 6.1 *XYZ* deflection signal of the scan piezo caused by exciting one shear stack piezo of the coarse motor at a specific frequency, on a linear scale (a) as well on a log-log scale (b). Below a driving frequency of 1.5 kHz the scan piezo is almost not deflected by the excitation which reflects the stiffness of the STM-head.

onances at frequencies above the detection bandwidth of 1 kHz. In order to verify this, an oscillating voltage with frequency f was applied at one of the shear stages of the coarse motor to excite a vibration in the STM head. The response of the system was captured by recording the voltage induced by the vibrations at the piezo-tube of the scan-stage. The resulting spectrum in **Figure 6.1** shows that the first resonances are located above 1.5 kHz. These resonances would not modulate the tunnel junction since they can only be detected in the *XY* deflection of the scan-stage. An increased deflection in the *Z* direction (corresponding to the tip-sample direction) is only observed at frequencies higher than 1.8 kHz and two order of magnitude weaker than the lateral motion resonances.

In addition to the stiffness and resonant behavior of the STM head, the mechanical noise performance of the spring stage holding the head also plays a significant role. In the second test the characteristics of the spring stage were investigated. The spring stage consists of four springs connected to the top four corners of the STM head. The springs are made of Copper-Berylium (CuBe) wire, which is a typical material for springs. To harden the springs after winding they were annealed at approximately 300 C. In contrast to the high eigenfrequency of the STM head, the spring stage ideally has low eigenfrequencies of about 3 Hz in order to effectively damp high frequency vibrations of the environment [Voi15]. By tuning wire diameter, winding number, winding diameter and preload a satisfying set of springs were produced. In order to test the spring stage, a motion capturing

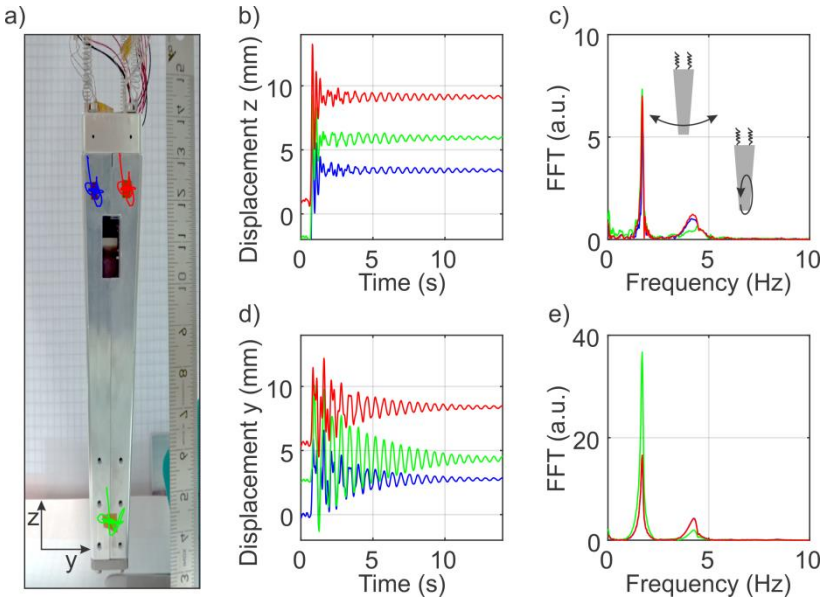

Figure 6.2 The properties of the spring stage were investigated by motion capturing three marks at the STM head (a). The spring stage attached STM head was lifted about 1 cm and then dropped to swing freely on the spring suspension. The trajectories of the three markers were tracked with a video camera (blue, red and, green line). (b),(d) Displacement in z and y direction, respectively, of the three markers as function of time. (c),(e) Power spectral density (PSD) of the movement in z and y direction, respectively. PSD curves are dominated by two modes, a sharp mode at 1.7 Hz and a broad mode at 4.2 Hz. While the 1.7 Hz mode is a swing mode the broad 4.2 Hz mode is a complex bounce mode, as indicated in the two cartoons.

technique was used. The movement of the attached STM head was video-recorded after exciting it with a little push. By tracking three markers the full movement of the STM head was recovered. The results of this analysis are shown in **Figure 6.2**. The test revealed two dominant modes. The first mode is a swing-mode at 1.7 Hz with low damping and the second one is the *up-down* mode at 4.2 Hz which is much more damped.

The undamped swing mode in particular could cause noise in the tunneling experiment. In order to suppress it a damping mechanism is installed. The damping is achieved by magnets attached to wings at the bottom of the STM head, which cause eddy currents in the radiation shield when the STM head moves. The eddy current damping at this point is very effective since all the detected modes move the bottom of the STM head significantly. Although the measured modes will change when the cabling and braids are connected to

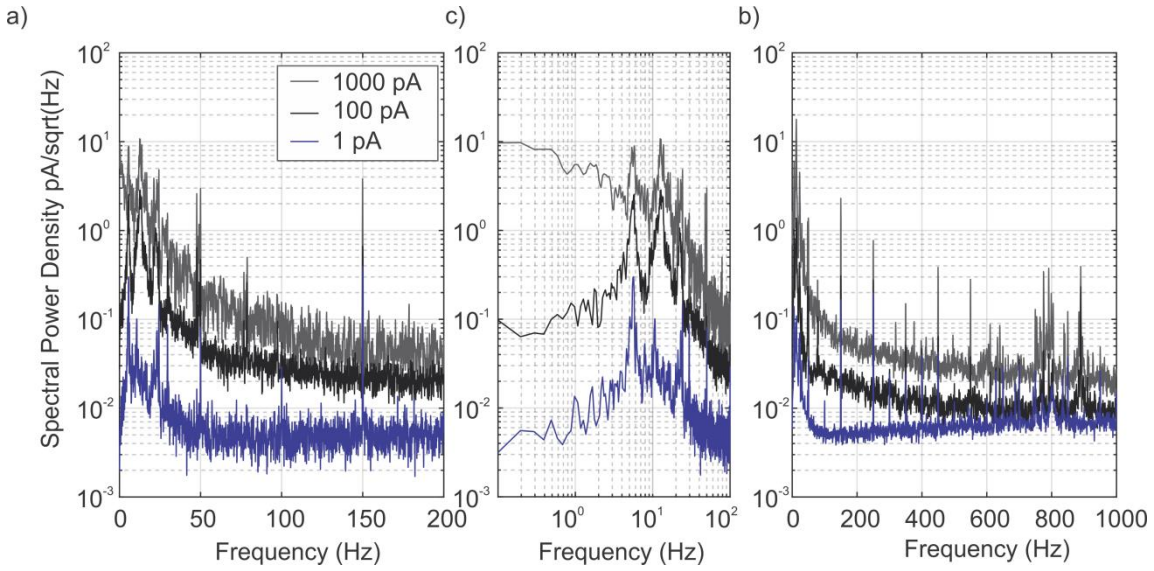

Figure 6.3 tunnel current power spectra for different setpoint currents from 1 pA to 1 nA at a voltage of 100 mV recorded on a $NbSe_2$ surface at 20 K with very slow feedback settings. For a setcurrent of 1 pA the current noise for frequencies above 50 Hz is on the same order as the current noise with the tip withdrawn.

the STM head or when the experiment is cooled down, the demonstrated analysis gives a good impression of the behavior of the spring stage.

Finally, the effect of the mechanical properties on the noise performance of the STM is explored in the tunneling experiment itself. The impact of vibrations altering the tip sample distance can be revealed with current power spectra for different setpoint currents and under slow feedback conditions. In the final experimental setup on 2H-$NbSe_2$ at low temperature conditions several noise spectra were recorded, see **Figure 6.3**. The origins of the features in the spectra are manifold. Not just vibrations, which directly alter the tip-sample distance, but also other voltage- or current-noise sources have their impact, such as capacitive-crosstalk, microphonic noise and so forth. Apart from the sharp features at frequencies which are multiples of 50 Hz (originating from electronic hum), the most pronounced features are located at 6 Hz, 13 Hz and 23 Hz. These rather broad features result from vibrations in the environment which couple through the spring stage to the tunnel-cable or directly to the tunnel junction. At high frequencies, around 800 Hz, another broad feature is located. This vibrational noise is most likely caused by acoustic noise.

The laser's cooling fans could for example couple into the junction through the UHV chamber.

Although the detailed examination of the power spectra is rather difficult it gives an approximation of the total vibrational noise floor. Assuming that for a large setpoint current I_0 the noise is dominated by vibrations perturbing the tip-sample distance z by Δz, the current can be approximated by:

$$I(z + \Delta z) = A\, e^{-2\kappa(z+\Delta z)} \propto I_0(1 - \kappa\, \Delta z). \tag{6.1}$$

Here κ is the decay constant of the tunnel current with increasing tip-sample distance and has typical a value of about $\kappa \approx 1\ \text{Å}^{-1}$ [Che08]. Integrating over the power spectrum and applying the approximated form of the tunnel current yields a root mean square of the vibration noise of 2.5 pm. This vibration performance is sufficient for the planned experiments. Considering that the current power spectra are not recorded under the best possible conditions and that some of the noise is not vibrational in origin, the calculated mean vibrational noise is overestimating the true vibration acting at the tunnel junction.

6.2.2 Cryostat and radiation shields

The intended experiments require that the sample inside the THz-STM be cooled. To enable this, the STM is attached to a cooling system based on a commercial low-noise flow cryostat from *Advanced Research Systems* (*ARS)*. A flow cryostat uses the latent heat occurring during the vaporization of a cryogenic liquid to cool a *cold finger* attached to the experiment. Moreover, in the case of the flow cryostat from *ARS,* the cold evaporated gas also cools the experiment in a heat exchange unit. In this thesis liquid Helium is used as a cryogenic, which in principle allows cooling down to 4.2 K [Adv15].

The STM head is only indirectly attached to the *cold finger* of the cryostat via the vibration isolation stage. This connection is not sufficient to effectively cool the STM-head, as the four springs of the vibration isolation stage have only a limited heat conductance. Additional Cu-braids between cold-tip and STM head are therefore attached to increase the

heat conductance. Similar braids are also used inside the head to thermally contact the sample to the body of the head.

Despite the additional braids the heat conductance between head and *cold finger* remains limited and heat radiation from the environment can prevent low temperatures at the sample from being reached. To counteract this, the head is encapsulated in a radiation shield. This shield is rigidly connected to the *cold finger* and blocks heat radiation emitted onto the head. The radiation shield is made out of pure Copper and has been polished in order to reduce heat absorption. In addition to the low temperature shield, a second radiation shield is attached to a second mount at the cryostat with higher temperature but also higher cooling power. This second shield completely encapsulates the first one and reduces the total heat load that has to be transported away by the *cold finger*.

To estimate the heat load the optical access for the THz-laser pulses has to be considered. The shields have holes through which head radiation will enter the system. Based the Stefan-Boltzman law, the heat radiation P incident on the inner shield is estimated as [SSSM13]:

$$P = 5.67 \times 10^{-8} \frac{\mathrm{W}}{\mathrm{m^2 K^4}} A\, T^4. \qquad 6.2$$

Here A is the area and T is the temperature of the emitting surface. Assuming a temperature below 60 K of the second shield and an approximate surface area of 0.175 m^2, the second shield emits roughly 0.1 W onto the inner shield. A more significant contribution comes from the two holes (with radius $r \approx 1.5$ cm) in the second shield. Since the radiation transmitted through them originates from the room temperature environment they behave like a room temperature surface and accordingly emit 0.6 W onto the inner shield. Based on this estimation, if all the radiation is absorbed the cryostat has to deliver about 0.7 W of cooling power to be able in order to keep the STM cold. This large amount of necessary cooling power is one of the reasons for the choice of a flow cryostat from *ARS* which can provide about 0.5 W at 4.2 K and about 3 W at 30 K.

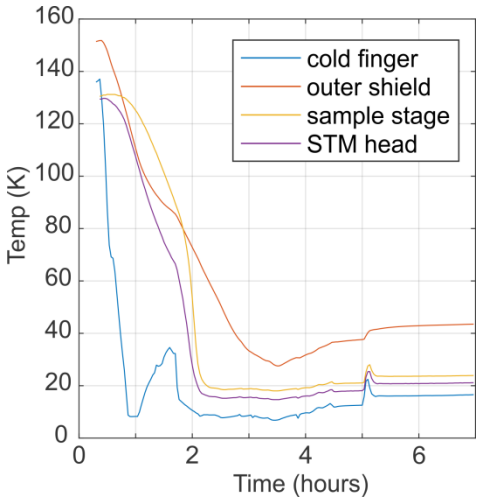

Figure 6.4 A typical cooling curve of the THz-STM. The four thermal sensors are attached to the *cold finger* of the cryostat, the 2nd radiation shield, the sample stage and at the STM body. While the *cold finger* reaches the base temperature in about 30 minutes the STM head needs around two hours to cool down from 150 K. At the base temperature the *cold finger* has a temperature of 7 K while the sample reaches about 18 K. By increasing the temperature of the *cold finger* the temperature difference with the sample is reduced as well. With a *cold finger* at 16 K the sample temperature only rises to 24 K.

The cooling capacity achieved is shown in a typical cool down curve in **Figure 6.4**. The temperature of different parts of the STM was recorded during the cooling process. The complete cool down procedure requires approximately 30 minutes. However, based on later STM measurements it was found that a fully equilibrated state is only reached after several hours. **Figure 6.4** also illustrated that the *cold finger* of the cryostat is the coldest spot in the instrument. The temperature of STM head and of the sample stage are about 5 K and 8 K warmer than the *cold finger*, respectively. This can be explained by the heat radiation coming through the holes and being absorbed at the sample in particular. The outer shield is about 26 K warmer than the *cold finger*. Without restricting the Helium flow through the cryostat a minimum temperature of about 15 K can be reached at the sample.

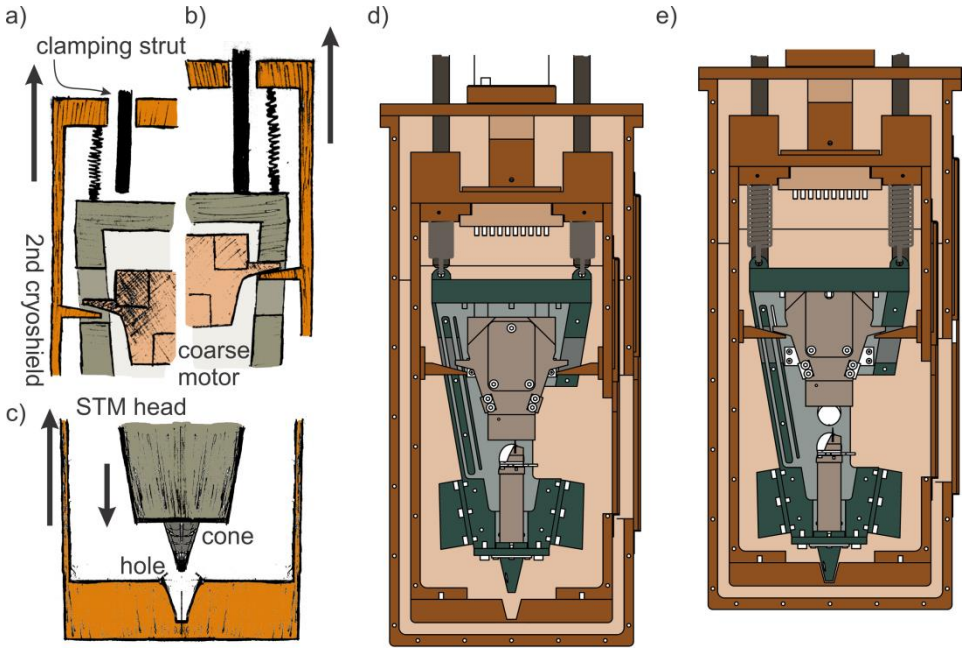

Figure 6.5 sketch of the clamping mechanism. (a) When lifting the STM two clamping struts penetrate the STM through the top of the radiations shields. (b) The struts hold the STM head in position while the other parts continue to lift. Two wedge-shaped protrusions fixed at the inner shield lock the coarse motor in place by pressing it against the STM head. c) When the cone attached to the bottom of the head is plugged into the hole in the radiation shield, the clamping is completed. (d),(e) Technical drawing of the clamping procedure.

6.2.3 Clamping mechanism for tip and sample exchange

A reliable *in-situ* tip and sample exchange procedure is essential for continuous measurement performance and the investigation of sample systems which need to stay *in-situ* after their final preparation. Although exchange procedures are specific for every STM design certain principles are similar. One main principle is the prevention of accidental damage to the STM by locking all free or movable parts before any exchange. This prevents damage such as ripping of cables or the breaking of a piezo. For the THz-STM, the STM-head and the coarse movement motor have to be locked. A locking mechanism was invented for this purpose which clamps the STM head and the coarse motor while lifting the STM to the *exchange* position.

Upon lifting the STM, two struts mounted to the top of the UHV chamber plunge into the inside of the radiation shield through holes in the shields. During the lift, and at a prede-

fined height the struts will touch and keep the STM head in position. At this moment, the shields are still moving up but the STM head becomes clamped between the struts and cone at the bottom which fits into a hole inside the first shield. This procedure is sketched in **Figure 6.5**.

The clamping of the coarse motor during lifting is achieved by wedge-shaped protrusions at the inner shield and at the coarse motor, see **Figure 6.5**. The wedges are arranged in a way such that when the struts are keeping the head in place, the wedges at the shield are lifting the motor and finally lock it by pressing is against the STM-head.

A further critical point during clamping is the possible danger of breaking the STM if it is lifted above the final locking position. An indirect spring loaded mounting of the struts to chamber prevents this scenario. Analogous to a shock absorber, the indirect mounting has springs which start to squeeze when the struts begin to clamp the STM. This squeezing is observable by the user and allows the lift to be stopped at the right position. When the STM is locked safely the tip and the sample can be exchanged with a UHV-manipulator wobblestick from *Ferrovac*.

6.3 Chapter 5 - Simple Landau model of CDW dynamics

A rudimentary understanding of CDW dynamics is achieved in a toy model based on Landau theory [SN86, McM75]. This toy model is briefly explained here. Neglecting further details in the framework of Landau theory the spatially averaged free energy $F(\psi)$ of a system with a complex order parameter ψ can be written as:

$$F(\psi) = \alpha(T)|\psi|^2 + \beta\,|\psi|^4 + Y(T)\,Re(\psi), \tag{6.3}$$

with phenomenological parameters $\alpha(T)$, β, $Y(T)$. The last term on the right hand side is introduced in order to consider pinning at atomic defects. Above the transition temperature $T > T_c$ it holds that $\alpha(T) > 0$ and $Y(T) = 0$, while below the transition it holds that $\alpha(T) < 0$ and $Y(T) \neq 0$.

The order parameter in equilibrium $\psi_0$is found by minimizing the free energy. At equilibrium the following equation has to be fulfilled:

$$\left.\frac{\partial F(\psi)}{\partial \psi}\right|_{\psi_0} = 0. \tag{6.4}$$

The dynamic behavior of the order parameter can be described by the introduction of a kinetic energy term:

$$T = M\,\frac{\partial \psi}{\partial t}\,\frac{\partial \psi^*}{\partial t} = M|\dot{\psi}|^2. \tag{6.5}$$

Here *M* is the effective mass of the order parameter. Based on a Lagrangian formalism the equation of motion can be found. The Lagrangian $\mathcal{L}$ is given by:

$$\mathcal{L} = T - F \tag{6.6}$$

If ψ^* is treated as a generalized coordinate then the equation of motion is given by:

$$\frac{\mathrm{d}}{\mathrm{d}t}\left(\frac{\partial \mathcal{L}}{\partial \dot{\psi}^*}\right) - \frac{\partial \mathcal{L}}{\partial \psi^*} = 0 \tag{6.7}$$

This yields:

$$M\ddot{\psi} = -\alpha(T)\psi - 2\beta\,\psi|\psi|^2 - \frac{Y(T)}{2} - \gamma\dot{\psi}. \tag{6.8}$$

Here, the last term $-\gamma\dot{\psi}$ is added to account for energy dissipation. The trajectory of the order parameter $\psi(t)$ can be calculated numerically from equation 6.8. The effect of a relaxing heated electron system modeled by a time varying free energy potential. This can be simulated by time-dependent parameters $\alpha(t)$ and $Y(t)$. For **Figure 5.15** $\alpha(t)$ and $Y(t)$ were modeled by:

$$\alpha(t) = (\alpha_0 + \Delta\alpha\, e^{-\frac{t}{\tau}}) \text{ and } Y(t) = Y_0\left(1 - 1\, e^{-\frac{t}{\tau}}\right). \tag{6.9}$$

Here τ is the relaxation time of the electronic system. At $t = 0$ the electron system is heated and the free energy favors a vanishing order parameter ($\alpha(t=0) = (\alpha_0 + \Delta\alpha) > 0$ and $Y(t=0) = 0$). For long times ($t \to \infty$) the equilibrium order parameter is finite ($\alpha(t \to$

$\infty) = \alpha_0 < 0$) with a defined phase ($Y(t \to \infty) = Y_0 \neq 0$) which result in a amplitude and a phase mode. The model parameters used in the main text are listed in **Table 6.2**.

$\boldsymbol{\alpha_0}$	$\boldsymbol{\Delta\alpha}$	$\boldsymbol{\beta}$	$\boldsymbol{Y_0}$	$\boldsymbol{M}$	$\boldsymbol{\tau}$	$\boldsymbol{\gamma}$	$\boldsymbol{\psi(t=0)}$
-10	+12	1	-4	2	0.6	0.25	$2.25 \cdot e^{0.3i}$

Table 6.2 parameter for Landau Model

References

[ACR+14] C. J. Arguello, S. P. Chockalingam, E. P. Rosenthal, L. Zhao, C. Gutierrez, J. H. Kang, W. C. Chung, R. M. Fernandes, S. Jia, A. J. Millis, R. J. Cava, and A. N. Pasupathy. Visualizing the charge density wave transition in 2H-$NbSe_2$ in real space. *Physical Review B*, 89:235115, 2014.

[Adv15] Advanced Research Systems, Inc. *LT3B Helitran: Instruction manual*, 2015.

[AFJ93] M. Amman, S. B. Field, and R. C. Jaklevic. Coulomb-blockade spectroscopy of gold particles imaged with scanning tunneling microscopy. *Physical Review B*, 48:12104–12109, 1993.

[And72] P. W. Anderson. More is different. *Science*, 177(4047):393–396, 1972.

[App67] J. A. Appelbaum. Exchange model of zero-bias tunneling anomalies. *Physical Review*, 154:633–643, 1967.

[ARA+15] C. J. Arguello, E. P. Rosenthal, E. F. Andrade, W. Jin, P. C. Yeh, N. Zaki, S. Jia, R. J. Cava, R. M. Fernandes, A. J. Millis, T. Valla, R. M. Osgood, and A. N. Pasupathy. Quasiparticle interference, quasiparticle interactions, and the origin of the charge density wave in 2H-$NbSe_2$. *Physical Review Letters*, 114:037001, 2015.

[ARV92] N. Agraït, J. G. Rodrigo, and S. Vieira. Transition from the tunneling regime to point contact and proximity-induced Josephson effect in lead-normal-metal nanojunctions. *Physical Review B*, 46:5814–5817, 1992.

[Ave02] A.J. Averitt, R. D.and Taylor. Ultrafast optical and far-infrared quasiparticle dynamics in correlated electron materials. *Journal of Physics: Condensed Matter*, 14(50):R1357, 2002.

[BAvdM+11] D. N. Basov, R. D. Averitt, D. van der Marel, M. Dressel, and K. Haule. Electrodynamics of correlated electron materials. *Reviews of Modern Physics*, 83:471–541, 2011.

[BK08] K.-H. Bennemann and J.B. Ketterson. *Superconductivity*. Springer Science & Business Media, 2008.

[BKZ+09] S.V. Borisenko, A.A. Kordyuk, V.B. Zabolotnyy, D.S. Inosov, D. Evtushinsky, B. Büchner, A.N. Yaresko, A. Varykhalov, R. Follath, W. Eberhardt, L. Patthey, and H. Berger. Two energy gaps and fermi-surface "arcs" in 2H-$NbSe_2$. *Physical Review Letters*, 102:166402, 2009.

[BLF13] S.J. Bartolome, F. Luis, and J.F. Fernández. *Molecular Magnets: Physics and Applications*. NanoScience and Technology. Springer Berlin Heidelberg, 2013.

[Bod03] M. Bode. Spin-polarized scanning tunnelling microscopy. *Reports on Progress in Physics*, 66(4):523, 2003.

[BPC+15] S. Baumann, W. Paul, T. Choi, C. P. Lutz, A. Ardavan, and A.J. Heinrich. Electron paramagnetic resonance of individual atoms on a surface. *Science*, 350(6259):417–420, 2015.

[BR08] N. Behr and M.B. Raschke. Optical antenna properties of scanning probe tips: Plasmonic light scattering, tip-sample coupling, and near-field enhancement. *The Journal of Physical Chemistry C*, 112(10):3766–3773, 2008.

[BRGW] G. Binnig, H. Rohrer, Ch. Gerber, and E. Weibel. Tunneling through a controllable vacuum gap. *Applied Physics Letters*, 40(2):178–180.

[BRGW82] G. Binnig, H. Rohrer, Ch. Gerber, and E. Weibel. Surface studies by scanning tunneling microscopy. *Physical Review Letters*, 49:57–61, 1982.

[BSWB16] A. Burtzlaff, N.L. Schneider, A. Weismann, and R. Berndt. Shot noise from single atom contacts in a scanning tunneling microscope. *Surface Science*, 643:10 – 12, 2016.

[BWBB15] A. Burtzlaff, A. Weismann, M. Brandbyge, and R. Berndt. Shot noise as a probe of spin-polarized transport through single atoms. *Physical Review Letters*, 114:016602, 2015.

[CET74] L.L. Chang, L. Esaki, and R Tsu. Resonant tunneling in semiconductor double barriers. *Applied Physics Letters*, 24(12):593–595, 1974.

[Che08] C.J. Chen. *Introduction to scanning tunneling microscopy*. Monographs on the physics and chemistry of materials. Oxford University Press, 2008.

[CHZ+07] L. Chen, Z. Hu, A. Zhao, B. Wang, Y. Luo, and J.G. Yang, J.and Hou. Mechanism for negative differential resistance in molecular electronic devices: Local orbital symmetry matching. *Physical Review Letters*, 99:146803, 2007.

[CJG+13] T.L. Cocker, V. Jelic, M. Gupta, S.J. Molesky, J.A.J. Burgess, G. De Los Reyes, L.V. Titova, Ying Y. Tsui, Mark R. Freeman, and Frank A. Hegmann. An ultrafast terahertz scanning tunnelling microscope. *Nature Photonics*, 7(8):620–625, 2013.

[CN05] H. Cao and A. Nahata. Coupling of terahertz pulses onto a single metal wire waveguide using milled grooves. *Optics Express*, 13(18):7028–7034, 2005.

[CPRP+17] T. Choi, W. Paul, S. Rolf-Pissarczyk, A.J. Macdonald, F.D. Natterer, K. Yang, P. Willke, C.P. Lutz, and A.J. Heinrich. Atomic-scale sensing of the magnetic dipolar field from single atoms. *Nature Nanotechnology*, 12(5):420–424, 2017.

[CPYR16] T.L. Cocker, D. Peller, P. Yu, and R. Repp, J.and Huber. Tracking the ultrafast motion of a single molecule by femtosecond orbital imaging. *Nature*, 539(7628):263–267, 2016.

[CRRT99] J. Chen, M. A. Reed, A. M. Rawlett, and J. M. Tour. Large on-off ratios and negative differential resistance in a molecular electronic device. *Science*, 286(5444):1550–1552, 1999.

[CRY+17] D.-J. Choi, R. Robles, S. Yan, J.A.J. Burgess, S. Rolf-Pissarczyk, J.-P. Gauyacq, N. Lorente, M. Ternes, and S. Loth. Building complex Kondo impurities by manipulating entangled spin chains. *Nano Letters*, 17(10):6203–6209, 2017.

[CZI+15] U. Chatterjee, J. Zhao, M. Iavarone, R. Di Capua, J.P. Castellan, G. Karapetrov, C.D. Malliakas, M.G. Kanatzidis, H. Claus, J.P.C Ruff, F. Weber, J. van Wezel, J. C. Campuzano, R. Osborn, M. Randeria, N. Trivedi, M. R. Norman, and S. Rosenkranz. Emergence of coherence in the charge-density wave state of 2H-$NbSe_2$. *Nature Communications*, 6, 2015.

[Dag05] E. Dagotto. Complexity in strongly correlated electronic systems. *Science*, 309(5732):257–262, 2005.

[DBD+03] S.V. Dordevic, D.N. Basov, R.C. Dynes, B. Ruzicka, V. Vescoli, L. Degiorgi, H. Berger, R. Gall, L. Forro, and E. Bucher. Optical properties of the quasi-two-dimensional dichalcogenides 2H-$TaSe_2$ and 2H-$NbSe_2$. *The European Physical Journal B - Condensed Matter and Complex Systems*, 33(1):15–23, 2003.

[DBM99] J. Demsar, K. Biljakovic, and D. Mihailovic. Single particle and collective excitations in the one-dimensional charge density wave solid $K_{0.3}MoO_3$ probed in real time by femtosecond spectroscopy. *Physical Review Letters*, 83:800–803, 1999.

[Dem15] W. Demtröder. Time-resolved laser spectroscopy. In *Laser Spectroscopy 2: Experimental Techniques*, pages 271–368. Springer Berlin Heidelberg, Berlin, Heidelberg, 2015.

[DLZFR15] F. Delgado, S. Loth, M. Zielinski, and J. Fernández-Rossier. The emergence of classical behaviour in magnetic adatoms. *EPL (Europhysics Letters)*, 109(5):57001, 2015.

[DMK+01] Z. J. Donhauser, B. A. Mantooth, K. F. Kelly, L. A. Bumm, J. D. Monnell, J. J. Stapleton, D. W. Price, A. M. Rawlett, D. L. Allara, J. M. Tour, and P. S.

Weiss. Conductance switching in single molecules through conformational changes. *Science*, 292(5525):2303–2307, 2001.

[DPFR10] F. Delgado, J.J. Palacios, and J. Fernández-Rossier. Spin-transfer torque on a single magnetic adatom. *Physical Review Letters*, 104:026601, 2010.

[DWEM06] J.A. Deibel, K. Wang, M.D. Escarra, and D.M. Mittleman. Enhanced coupling of terahertz radiation to cylindrical wire waveguides. *Optics Express*, 14(1):279–290, 2006.

[EF71] J. Edwards and R.F. Frindt. Anisotropy in the resistivity of 2H-$NbSe_2$. *Journal of Physics and Chemistry of Solids*, 32(9):2217 – 2221, 1971.

[EPCR00] P.M. Echenique, J.M. Pitarke, E.V. Chulkov, and A. Rubio. Theory of inelastic lifetimes of low-energy electrons in metals. *Chemical Physics*, 251(1):1–35, 2000.

[ES90] D.M. Eigler and E.K. Schweizer. Positioning single atoms with a scanning tunnelling microscope. *Nature*, 344(6266):524–526, 1990.

[Esa58] L. Esaki. New phenomenon in narrow germanium *p-n* junctions. *Physical Review*, 109:603–604, 1958.

[Esa74] L. Esaki. Long journey into tunneling. *Reviews of Modern Physics*, 46:237–244, 1974.

[ESK+10] Maximilian Eichberger, Hanjo Schafer, Marina Krumova, Markus Beyer, Jure Demsar, Helmuth Berger, Gustavo Moriena, German Sciaini, and R. J. Dwayne Miller. Snapshots of cooperative atomic motions in the optical suppression of charge density waves. *Nature*, 468(7325):799–802, December 2010.

[ET06] F. Elste and C. Timm. Transport through anisotropic magnetic molecules with partially ferromagnetic leads: Spin-charge conversion and negative differential conductance. *Physical Review B*, 73:235305, 2006.

[Fee03] R.M. Feenstra. Electrostatic potential for a hyperbolic probe tip near a semiconductor. *Journal of Vacuum Science & Technology B: Microelectronics and Nanometer Structures Processing, Measurement, and Phenomena*, 21(5):2080–2088, 2003.

[FHW+17] T. Frigge, B. Hafke, T. Witte, B. Krenzer, C. Streubühr, A. Samad Syed, V. Mikšic Trontl, I. Avigo, P. Zhou, M. Ligges, D. von der Linde, U. Bovensiepen, M. Horn-von Hoegen, S. Wippermann, A. Lücke, S. Sanna, U. Gerstmann, and W. G. Schmidt. Optically excited structural transition in atomic wires on surfaces at the quantum limit. *Nature*, 544(7649):207–211, 2017.

[FPK+12] J. A. Fülöp, L. Pálfalvi, S. Klingebiel, G. Almási, F. Krausz, S. Karsch, and J. Hebling. Generation of sub-mj terahertz pulses by optical rectification. *Optics Letters*, 37(4):557–559, 2012.

[Frö54] H Fröhlich. On the theory of superconductivity: the one-dimensional case. volume 223, pages 296–305. The Royal Society, 1954.

[FR09] J. Fernández-Rossier. Theory of single-spin inelastic tunneling spectroscopy. *Physical Review Letters*, 102:256802, 2009.

[FTD+11] D. Fausti, R. I. Tobey, N. Dean, S. Kaiser, A. Dienst, M. C. Hoffmann, S. Pyon, T. Takayama, H. Takagi, and A. Cavalleri. Light-induced superconductivity in a stripe-ordered cuprate. *Science*, 331(6014):189–191, 2011.

[Ful12] P. Fulde. *Electron Correlations in Molecules and Solids*. Springer Series in Solid-State Sciences. Springer Berlin Heidelberg, 2012.

[FvW15] F. Flicker and J. van Wezel. Charge order from orbital-dependent coupling evidenced by 2H-$NbSe_2$. *Nature Communications*, 6:7034, 2015.

[GCF+16] C. Giannetti, M. Capone, D. Fausti, M. Fabrizio, and D. Parmigiani, F.and Mihailovic. Ultrafast optical spectroscopy of strongly correlated ma-

terials and high-temperature superconductors: a non-equilibrium approach. *Advances in Physics*, 65(2):58–238, 2016.

[GEKK13] C. Grosse, M. Etzkorn, S. Kuhnke, K.and Loth, and K. Kern. Quantitative mapping of fast voltage pulses in tunnel junctions by plasmonic luminescence. *Applied Physics Letters*, 103(18):183108–, 2013.

[GJC+88] B. Giambattista, A. Johnson, R. V. Coleman, B. Drake, and P. K. Hansma. Charge-density waves observed at 4.2 K by scanning-tunneling microscopy. *Physical Review B*, 37:2741–2744, 1988.

[GKP+00] V. Gerstner, A. Knoll, W. Pfeiffer, A. Thon, and G. Gerber. Femtosecond laser assisted scanning tunneling microscopy. *Journal of Applied Physics*, 88(8):4851–4859, 2000.

[GLH00] J. Gaudioso, L. J. Lauhon, and W. Ho. Vibrationally mediated negative differential resistance in a single molecule. *Physical Review Letters*, 85:1918–1921, 2000.

[Grü88] G. Grüner. The dynamics of charge-density waves. *Reviews of Modern Physics*, 60:1129–1181, 1988.

[Grü94] G. Grüner. *Density Waves In Solids*. Frontiers in Physics, 1994.

[Gra02] S. Grafström. Photoassisted scanning tunneling microscopy. *Journal of applied physics*, 91(4):1717–1753, 2002.

[Gru06] M. Grundmann. *The Physics of Semiconductors*. Springer-Verlag, 2006.

[GSV11] D. Gatteschi, R. Sessoli, and J. Villain. *Molecular Nanomagnets*. Mesoscopic Physics and Nanotechnology. OUP Oxford, 2011.

[GTP00] V. Gerstner, A. Thon, and W. Pfeiffer. Thermal effects in pulsed laser assisted scanning tunneling microscopy. *Journal of Applied Physics*, 87(5):2574–2580, 2000.

[HF11] M.C. Hoffmann and J.A. Fülöp. Intense ultrashort terahertz pulses: generation and applications. *Journal of Physics D: Applied Physics*, 44(8):083001, 2011.

[HGLE04] A.J. Heinrich, J.A. Gupta, C.P. Lutz, and D.M. Eigler. Single-atom spin-flip spectroscopy. *Science*, 306(5695):466–469, 2004.

[HLH00] J.R. Hahn, H.J. Lee, and W. Ho. Electronic resonance and symmetry in single-molecule inelastic electron tunneling. *Physical Review Letters*, 85:1914–1917, 2000.

[HLH06] Cyrus F. Hirjibehedin, Christopher P. Lutz, and Andreas J. Heinrich. Spin coupling in engineered atomic structures. *Science*, 312(5776):1021–1024, 2006.

[HLO+07] C.F. Hirjibehedin, C.-Y. Lin, A.F. Otte, M. Ternes, C.P. Lutz, B.A. Jones, and A.J. Heinrich. Large magnetic anisotropy of a single atomic spin embedded in a surface molecular network. *Science*, 317(5842):1199–1203, 2007.

[HRK+12] S. Hellmann, T. Rohwer, M. KallÃ¤ne, K. Hanff, C. Sohrt, A. Stange, A. Carr, M.M. Murnane, H.C. Kapteyn, L. Kipp, M. Bauer, and K. Rossnagel. Time-domain classification of charge-density-wave insulators. 3:1069–, 2012.

[HSA+04] J. Hebling, A.G. Stepanov, G. Almási, B. Bartal, and J. Kuhl. Tunable THz pulse generation by optical rectification of ultrashort laser pulses with tilted pulse fronts. *Applied Physics B*, 78(5):593–599, 2004.

[HvBY+16] R. He, J. van Baren, J.-A. Yan, X. Xi, Z. Ye, G. Ye, I.-H. Lu, S.M. Leong, and C.H. Lui. Interlayer breathing and shear modes in 2H-$NbSe_2$ atomic layers. *2D Materials*, 3(3):031008, 2016.

[HW05] N. Hodgson and H. Weber. *Laser Resonators and Beam Propagation: Fundamentals, Advanced Concepts, Applications*, volume 108. Springer, 2005.

[HYHN07] M.C. Hoffmann, K.-L. Yeh, J. Hebling, and K.A. Nelson. Efficient terahertz generation by optical rectification at 1035 nm. *Opt. Express*, 15(18):11706–11713, 2007.

[JIN+17] V. Jelic, K. Iwaszczuk, P.H. Nguyen, C. Rathje, G.J. Hornig, H.M. Sharum, J.R. Hoffman, M.R. Freeman, and F.A. Hegmann. Ultrafast terahertz control of extreme tunnel currents through single atoms on a silicon surface. *Nature Physics*, 13(6):591–598, 2017.

[JZG05] T.-I. Jeon, J. Zhang, and D. Grischkowsky. THz sommerfeld wave propagation on a single metal wire. *Applied Physics Letters*, 86(16):161904–, 2005.

[KBE+87] K. Kajimura, H. Bando, K. Endo, W. Mizutani, H. Murakami, M. Okano, S. Okayama, M. Ono, Y. Ono, H. Tokumoto, F. Sakai, K. Watanabe, and S. Wakiyama. Construction of an STM and observation of 2H-$NbSe_2$ atomic images. *Surface Science*, 181(1):165–173, 1987.

[Kit96] C. Kittel. *Introduction to Solid State Physics*. John wiley & Sons, Inc., seventh edition edition, 1996.

[KK04] G.-H. Kim and T.-S. Kim. Electronic transport in single-molecule magnets on metallic surfaces. *Physical Review Letters*, 92:137203, 2004.

[KSW07] U. Kaiser, A. Schwarz, and R. Wiesendanger. Magnetic exchange force microscopy with atomic resolution. *Nature*, 446:522–, 2007.

[KT16] A.V. Kolobov and J. Tominaga. *Two-Dimensional Transition-Metal Dichalcogenides*, volume 239. Springer, 2016.

[LBL+12] S. Loth, S. Baumann, C.P. Lutz, D.M. Eigler, and A.J. Heinrich. Bistability in atomic-scale antiferromagnets. *Science*, 335(6065):196–199, 2012.

[Lee09] Y.-S. Lee. *Principles of terahertz science and technology*, volume 170. Springer Science & Business Media, 2009.

[LEL+10] S. Loth, M. Etzkorn, C.P. Lutz, D.M. Eigler, and A.J. Heinrich. Measurement of fast electron spin relaxation times with atomic resolution. *Science*, 329(5999):1628–1630, 2010.

[LGMW70] H.N.S. Lee, M. Garcia, H. McKinzie, and A. Wold. The low-temperature electrical and magnetic properties of $TaSe_2$ and $NbSe_2$. *Journal of Solid State Chemistry*, 1(2):190–194, 1970.

[LGP+13] H.Y. Liu, I. Gierz, J.C. Petersen, S. Kaiser, A. Simoncig, A.L. Cavalieri, C. Cacho, I.C.E. Turcu, E. Springate, F. Frassetto, L. Poletto, S.S. Dhesi, Z.-A. Xu, T. Cuk, R. Merlin, and A. Cavalleri. Possible observation of parametrically amplified coherent phasons in $K_{0.3}MoO_3$ using time-resolved extreme-ultraviolet angle-resolved photoemission spectroscopy. *Physical Review B*, 88:045104, Jul 2013.

[LHT+12] M. Liu, H.Y. Hwang, H. Tao, A.C. Strikwerda, K. Fan, G.R. Keiser, A.J. Sternbach, K.G. West, Salinporn Kittiwatanakul, Jiwei Lu, S.A. Wolf, F.G. Omenetto, X. Zhang, K.A. Nelson, and R.D. Averitt. Terahertz-field-induced insulator-to-metal transition in vanadium dioxide metamaterial. *Nature*, 487(7407):345–348, 2012.

[LLH10] S. Loth, C.P. Lutz, and A.J. Heinrich. Spin-polarized spin excitation spectroscopy. *New Journal of Physics*, 12(12):125021, 2010.

[LMH+02] K. M. Lang, V. Madhavan, J. E. Hoffman, E. W. Hudson, H. Eisaki, S. Uchida, and J. C. Davis. Imaging the granular structure of high-Tc superconductivity in underdoped $Bi_2Sr_2CaCu_2O_{8+\delta}$. *Nature*, 415(6870):412–416, 2002.

[LN10] A. LeBlanc and A. Nader. Resistivity anisotropy and charge density wave in 2H-$NbSe_2$ and 2H-$TaSe_2$. *Solid State Communications*, 150(29):1346–1349, 2010.

[LRA74] P.A. Lee, T.M. Rice, and P.W. Anderson. Conductivity from charge or spin density waves. *Solid State Communications*, 14(8):703–709, 1974.

[LvBT+10] S. Loth, K. von Bergmann, M. Ternes, A.F. Otte, C.P. Lutz, and A.J. Heinrich. Controlling the state of quantum spins with electric currents. *Nature Physics*, 6(5):340–344, 2010.

[MAD75] D.E. Moncton, J.D. Axe, and F.J. DiSalvo. Study of superlattice formation in 2H-$NbSe_2$ and 2H-$TaSe_2$ by neutron scattering. *Physical Review Letters*, 34:734–737, 1975.

[MAD77] D.E. Moncton, J.D. Axe, and F.J. DiSalvo. Neutron scattering study of the charge-density wave transitions in 2H-$TaSe_2$ and 2H-$NbSe_2$. *Physical Review B*, 16:801–819, 1977.

[McM75] W.L. McMillan. Landau theory of charge-density waves in transition-metal dichalcogenides. *Physical Review B*, 12:1187–1196, 1975.

[McM17] G. McMurtrie. Transient and steady-state behavior of iron atoms. Master's thesis, University Hamburg, 2017.

[MCN+16] M. Mitrano, A. Cantaluppi, D. Nicoletti, S. Kaiser, A. Perucchi, S. Lupi, P. Di Pietro, D. Pontiroli, M. Riccó, S. R. Clark, D. Jaksch, and A. Cavalleri. Possible light-induced superconductivity in K_3C_{60} at high temperature. *Nature*, 530(7591):461–464, 2016.

[MGC+14] M.-A. Méasson, Y. Gallais, M. Cazayous, B. Clair, P. Rodière, L. Cario, and A. Sacuto. Amplitude Higgs mode in the 2H-$NbSe_2$ superconductor. *Physical Review B*, 89:060503, 2014.

[Mon12] P. Monceau. Electronic crystals: an experimental overview. *Advances in Physics*, 61(4):325–581, 2012.

[MRPY+] L. Malavolti, S. Rolf-Pissarczyk, S. Yan, J.A. J. Burgess, G. McMurtrie, and S. Loth. Towards non-perturbative spin sensing with scanning tunneling microscopy. (under preparation).

[NF93] G. Nunes and M.R. Freeman. Picosecond resolution in scanning tunneling microscopy. *Science*, 262(5136):1029–1032, 1993.

[NR09] W. Nolting and A. Ramakanth. *Quantum theory of magnetism*. Springer Science & Business Media, 2009.

[NR11] I. Naik and A.K. Rastogi. Charge density wave and superconductivity in 2H- and 4H-$NbSe_2$: A revisit. *Pramana*, 76(6):957–963, 2011.

[OATT02] K. Ono, D. G. Austing, Y. Tokura, and S. Tarucha. Current rectification by pauli exclusion in a weakly coupled double quantum dot system. *Science*, 297(5585):1313–1317, 2002.

[PFK+14] M.L. Perrin, R. Frisenda, M. Koole, J.S. Seldenthuis, G.A. Celis, H. Valkenier, J.C. Hummelen, N. Renaud, F.C. Grozema, J.M. Thijssen, D. Dulic, and H.S.J. van der Zant. Large negative differential conductance in single-molecule break junctions. *Nature Nanotechnology*, 9(10):830–834, 2014.

[PLCL+03] M. Pioro-Ladrière, M. Ciorga, J. Lapointe, P. Zawadzki, M. Korkusi nnski, P. Hawrylak, and A.S. Sachrajda. Spin-blockade spectroscopy of a two-level artificial molecule. *Physical Review Letters*, 91:026803, 2003.

[PLM+14] M. Porer, U. Leierseder, J.-M. Ménard, H. Dachraoui, L. Mouchliadis, I. E. Perakis, U. Heinzmann, J. Demsar, K. Rossnagel, and R. Huber. Non-thermal separation of electronic and structural orders in a persisting charge density wave. *Nature Materials*, 13(9):857–861, September 2014.

[Pou16] J.-P. Pouget. The Peierls instability and charge density wave in one-dimensional electronic conductors. *Comptes Rendus Physique*, 17(3):332–356, 2016.

[PP14] M. Perenzoni and D.J. Paul. *Physics and Applications of Terahertz Radiation*, volume 173. Springer, 2014.

[PYB+17] W. Paul, K. Yang, S. Baumann, N. Romming, T. Choi, C.P. Lutz, and A.J. Heinrich. Control of the millisecond spin lifetime of an electrically probed atom. *Nature Physics*, 13(4):403–407, 2017.

[RFT04] T.D. Rossing, N.H. Fletcher, and A. Tubis. Principles of vibration and sound. *The Journal of the Acoustical Society of America*, 116(5):2708–2708, 2004.

[RHK+12] D. J. Rahn, S. Hellmann, M. Kalläne, C. Sohrt, T. K. Kim, L. Kipp, and K. Rossnagel. Gaps and kinks in the electronic structure of the superconductor 2H-$NbSe_2$ from angle-resolved photoemission at 1 K. *Physical Review B*, 85:224532, 2012.

[RHW+11] T. Rohwer, S. Hellmann, M. Wiesenmayer, C. Sohrt, A. Stange, B. Slomski, A. Carr, Y. Liu, L.M. Avila, M. Kallane, S. Mathias, L. Kipp, K. Rossnagel, and M. Bauer. Collapse of long-range charge order tracked by time-resolved photoemission at high momenta. *Nature*, 471(7339):490–493, 2011.

[Ric75] T.M. Rice. Collective modes in charge density wave structures. *Solid State Communications*, 17(9):1055 – 1058, 1975.

[Rid93] B.K. Ridley. Negative differential resistance: A brief history and review. In *Negative Differential Resistance and Instabilities in 2-D Semiconductors*, pages 1–21. Springer, 1993.

[RMS+05] J. Repp, G. Meyer, S.M. Stojkovic, A. Gourdon, and C. Joachim. Molecules on insulating films: Scanning-tunneling microscopy imaging of individual molecular orbitals. *Physical Review Letters*, 94:026803, 2005.

[Ros11] K. Rossnagel. On the origin of charge-density waves in select layered transition-metal dichalcogenides. *Journal of Physics: Condensed Matter*, 23(21):213001, 2011.

[RPBYL16] S. Rolf-Pissarczyk, J.A.J. Burgess, S. Yan, and S. Loth. Closing the superconducting gap in small Pb nanoislands with high magnetic fields. *Physical Review B*, 94:224504, 2016.

[RPYM+17] S. Rolf-Pissarczyk, S. Yan, L. Malavolti, J.A.J. Burgess, G. McMurtrie, and S. Loth. Dynamical negative differential resistance in antiferromagnetically coupled few-atom spin chains. *Physical Review Letters*, 2017. (to be published).

[RSK+01] K. Rossnagel, O. Seifarth, L. Kipp, M. Skibowski, D. Voß, P. Krüger, A. Mazur, and J. Pollmann. Fermi surface of 2H-$NbSe_2$ and its implications on the charge-density-wave mechanism. *Physical Review B*, 64:235119, 2001.

[RTO+16] M. Rashidi, M. Taucer, I. Ozfidan, E. Lloyd, M. Koleini, H. Labidi, J.L. Pitters, J. Maciejko, and R.A. Wolkow. Time-resolved imaging of negative differential resistance on the atomic scale. *Physical Review Letters*, 117:276805, 2016.

[RXL04] Y. Ren, Z. Xu, and G. Lüpke. Ultrafast collective dynamics in the charge-density-wave conductor $K_{0.3}MoO_3$. *The Journal of Chemical Physics*, 120(10):4755–4758, 2004.

[Sae13] D. Saeedkia. *Handbook of terahertz technology for imaging, sensing and communications*. Elsevier, 2013.

[Sak94] J.J. Sakurai. *Modern quantum mechanics; rev. ed.* Addison-Wesley, Reading, MA, 1994.

[SBD+14] A. Spinelli, B. Bryant, F. Delgado, J. Fernández-Rossier, and A.F. Otte. Imaging of spin waves in atomically designed nanomagnets. *Nature Materials*, 13(8):782–785, 2014.

[SBPM13] C. Saunus, J.R. Bindel, M. Pratzer, and M. Morgenstern. Versatile scanning tunneling microscopy with 120 ps time resolution. *Applied Physics Letters*, 102(5):051601, 2013.

[SE91] J.A. Stroscio and D.M. Eigler. Atomic and molecular manipulation with the scanning tunneling microscope. *Science*, 254(5036):1319–1326, 1991.

[SEF98] G.M. Steeves, A.Y. Elezzabi, and M.R. Freeman. Nanometer-scale imaging with an ultrafast scanning tunneling microscope. *Applied Physics Letters*, 72(4):504–506, 1998.

[SHMS98] J.P. Sun, G.I. Haddad, P. Mazumder, and J. N. Schulman. Resonant tunneling diodes: models and properties. *Proceedings of the IEEE*, 86(4):641–660, 1998.

[SMJ+15] M. Schackert, T. Märkl, J. Jandke, M. Hölzer, S. Ostanin, E.K.U. Gross, A. Ernst, and W. Wulfhekel. Local measurement of the Eliashberg function of Pb islands: Enhancement of electron-phonon coupling by quantum well states. *Physical Review Letters*, 114:047002, 2015.

[SMSG92] M.P. Shaw, V.V. Mitin, E. Schöll, and H.L. Grubin. *Tunnel Diodes*, pages 147–177. Springer US, Boston, MA, 1992.

[SN86] H. Shiba and K. Nakanishi. *Structural Phase Transitions in Layered Transition Metal Compounds*, chapter Phenomenological Landau Theory of Charge Density Wave Phase Transitions in Layered Compounds, pages 175–266. Springer Netherlands, Dordrecht, 1986.

[SSSM13] P. Stephan, K. Schaber, K. Stephan, and F. Mayinger. *Thermodynamik: Grundlagen und technische Anwendungen Band 1: Einstoffsysteme*. Springer-Lehrbuch. Springer Berlin Heidelberg, 2013.

[STH06] S. Sugai, Y. Takayanagi, and N. Hayamizu. Phason and amplitudon in the charge-density-wave phase of one-dimensional charge stripes in $La_{2-x}Sr_xCuO_4$. *Physical Review Letters*, 96:137003, 2006.

[STH+16] R. Saito, Y. Tatsumi, S. Huang, X. Ling, and M.S. Dresselhaus. Raman spectroscopy of transition metal dichalcogenides. *Journal of Physics: Condensed Matter*, 28(35):353002, 2016.

[SYH+13] A. Soumyanarayanan, M.M. Yee, Y. He, J. van Wezel, D.J. Rahn, K. Rossnagel, E.W. Hudson, M.R. Norman, and J.E. Hoffman. Quantum phase transition from triangular to stripe charge order in $NbSe_2$. *Proceedings of the National Academy of Sciences*, 110(5):1623–1627, 2013.

[Tao06] N.J. Tao. Electron transport in molecular junctions. *Nature Nanotechnology*, 1(3):173–181, 2006.

[TBK+87] H. Tokumoto, H. Bando, K. Kajimura, W. Mizutani, H. Murakami, M. Okano, S. Okayama, M. Ono, Y. Ono, F. Sakai, S. Wakiyama, and K. Watanabe. Summary abstract: Observation of 2H-$NbSe_2$ surface by scanning tunneling microscopy. *Journal of Vacuum Science & Technology A: Vacuum, Surfaces, and Films*, 5(4):1090–1092, 1987.

[TBM+86] H. Tokumoto, H. Bando, W. Mizutani, M. Okano, M. Ono, H. Murakami, S. Okayama, K. Ono, Y.and Watanabe, S. Wakiyama, F. Sakai, K. Endo, and K. Kajimura. Observation of 2H-$NbSe_2$ surface by scanning tunneling microscopy. *Japanese Journal of Applied Physics*, 25(8A):L621–L623, 1986.

[TBT12] S. Tani, F. Blanchard, and K. Tanaka. Ultrafast carrier dynamics in graphene under a high electric field. *Physical Review Letters*, 109:166603, 2012.

[Ter15] M. Ternes. Spin excitations and correlations in scanning tunneling spectroscopy. *New Journal of Physics*, 17(6):063016, 2015.

[TMB+13] D.H. Torchinsky, F. Mahmood, A.T. Bollinger, I. Božovic, and N. Gedik. Fluctuating charge-density waves in a cuprate superconductor. *Nature Materials*, 12(5):387–391, 2013.

[TP01] E.Y. Tsymbal and D.G. Pettifor. Perspectives of giant magnetoresistance. *Solid State Physics*, 56:113–237, 2001.

[Trä12] F. Träger. *Springer handbook of lasers and optics*. Springer Science & Business Media, 2012.

[TSS76] J.C. Tsang, J.E. Smith, and M.W. Shafer. Raman spectroscopy of soft modes at the charge-density-wave phase transition in 2H-$NbSe_2$. *Physical Review Letters*, 37:1407–1410, 1976.

[TYTS10a] Y. Terada, S. Yoshida, O. Takeuchi, and H. Shigekawa. Laser-combined scanning tunnelling microscopy for probing ultrafast transient dynamics. *Journal of Physics: Condensed Matter*, 22(26):264008, 2010.

[TYTS10b] Y. Terada, S. Yoshida, O. Takeuchi, and H. Shigekawa. Real-space imaging of transient carrier dynamics by nanoscale pump-probe microscopy. *Nature Photonics*, 4(12):869–874, 2010.

[UBZ+16] M. M. Ugeda, A.J. Bradley, Y. Zhang, S. Onishi, Y. Chen, W. Ruan, C. Ojeda-Aristizabal, H. Ryu, M.T. Edmonds, H.-Z. Tsai, A. Riss, S.-K. Mo, D. Lee, A. Zettl, Z. Hussain, Z.-X. Shen, and M.F. Crommie. Characterization of collective ground states in single-layer $NbSe_2$. *Nature Physics*, 12(1):92–97, 2016.

[vEFG89] M. van Exter, Ch. Fattinger, and D. Grischkowsky. Terahertz time-domain spectroscopy of water vapor. *Optics Letters*, 14(20):1128–1130, 1989.

[Voi15] B. Voigtlaender. *Scanning Probe Microscopy: Atomic Force Microscopy and Scanning Tunneling Microscopy*. NanoScience and Technology. Springer Berlin Heidelberg, 2015.

[WBJJ89] R. Wilkins, E. Ben-Jacob, and R. C. Jaklevic. Scanning-tunneling-microscope observations of coulomb blockade and oxide polarization in small metal droplets. *Physical Review Letters*, 63:801–804, 1989.

[WBT+91] R. Wiesendanger, D. Bürgler, G. Tarrach, A. Wadas, D. Brodbeck, H.-J. Güntherodt, G. Güntherodt, R.J. Gambino, and R. Ruf. Vacuum tunneling of spin-polarized electrons detected by scanning tunneling microscopy. *Journal of Vacuum Science & Technology B: Microelectronics and Nanometer Structures Processing, Measurement, and Phenomena*, 9(2):519–524, 1991.

[WCL+05] M. Walther, G.S. Chambers, Z. Liu, M.R. Freeman, and F.A. Hegmann. Emission and detection of terahertz pulses from a metal-tip antenna. *Journal of the Optical Society of America B*, 22(11):2357–2365, 2005.

[WDSM74] J.A. Wilson, F.J. Di Salvo, and S. Mahajan. Charge-density waves in metallic, layered, transition-metal dichalcogenides. *Physical Review Letters*, 32:882–885, 1974.

[WEHP+15] B. Warner, F. El Hallak, H. Prüser, J. Sharp, M. Persson, A.J. Fisher, and C.F. Hirjibehedin. Tunable magnetoresistance in an asymmetrically coupled single-molecule junction. *Nature Nanotechnology*, 10(3):259–263, 2015.

[WGS+90] C. Wang, B. Giambattista, C.G. Slough, R. V. Coleman, and M.A. Subramanian. Energy gaps measured by scanning tunneling microscopy. *Physical Review B*, 42:8890–8906, 1990.

[WHK95] D. Weinmann, W. Häusler, and B. Kramer. Spin blockades in linear and nonlinear transport through quantum dots. *Physical Review Letters*, 74:984–987, 1995.

[WHS+14] L. Wimmer, G. Herink, D. R. Solli, S. V. Yalunin, K. E. Echternkamp, and C. Ropers. Terahertz control of nanotip photoemission. *Nature Physics*, 10(6):432–436, 2014.

[Wie09] R. Wiesendanger. Spin mapping at the nanoscale and atomic scale. *Reviews of Modern Physics*, 81:1495–1550, 2009.

[WOB+93] S. Weiss, D.F. Ogletree, D. Botkin, M. Salmeron, and D.S. Chemla. Ultrafast scanning probe microscopy. *Applied Physics Letters*, 63(18):2567–2569, 1993.

[WRC+11] F. Weber, S. Rosenkranz, J.-P. Castellan, R. Osborn, R. Hott, R. Heid, K.-P. Bohnen, T. Egami, A. H. Said, and D. Reznik. Extended phonon collapse and the origin of the charge-density wave in 2H-$NbSe_2$. *Physical Review Letters*, 107:107403, 2011.

[WY69] J.A. Wilson and A.D. Yoffe. The transition metal dichalcogenides discussion and interpretation of the observed optical, electrical and structural properties. *Advances in Physics*, 18(73):193–335, 1969.

[XD15] B. Xu and Y. Dubi. Negative differential conductance in molecular junctions: an overview of experiment and theory. *Journal of Physics: Condensed Matter*, 27(26):263202, 2015.

[XZW+15] X. Xi, L. Zhao, Z. Wang, H. Berger, L. Forró, J. Shan, and K.F. Mak. Strongly enhanced charge-density-wave order in monolayer 2H-$NbSe_2$. *Nature Nanotechnology*, 10(9):765–769, 2015.

[YAW+14] S. Yoshida, Y. Aizawa, Z.-h. Wang, R. Oshima, Y. Mera, E. Matsuyama, H. Oigawa, and H. Takeuchi, O.and Shigekawa. Probing ultrafast spin dynamics with optical pump-probe scanning tunnelling microscopy. *Nature Nanotechnology*, 9(8):588–593, August 2014.

[YCB+15a] S. Yan, D.-J. Choi, J.A.J. Burgess, S. Rolf-Pissarczyk, and S. Loth. Control of quantum magnets by atomic exchange bias. *Nature Nanotechnology*, 10(1):40–45, 2015.

[YCB+15b] S. Yan, D.-J. Choi, J.A.J. Burgess, S. Rolf-Pissarczyk, and S. Loth. Three-dimensional mapping of single-atom magnetic anisotropy. *Nano Letters*, 15(3):1938–1942, 2015.

[YKM+16] K. Yoshioka, I. Katayama, Y. Minami, M. Kitajima, S. Yoshida, H. Shigekawa, and J. Takeda. Real-space coherent manipulation of electrons in a single tunnel junction by single-cycle terahertz electric fields. *Nature Photonics*, 10(12):762–765, 2016.

[YMB+17] S. Yan, L. Malavolti, J.A.J. Burgess, A. Droghetti, A. Rubio, and S. Loth. Nonlocally sensing the magnetic states of nanoscale antiferromagnets with an atomic spin sensor. *Science Advances*, 3(5), 2017.

[YMK+10] R. Yusupov, T. Mertelj, V.V. Kabanov, S. Brazovskii, P. Kusar, J.-H. Chu, I.R. Fisher, and D. Mihailovic. Coherent dynamics of macroscopic electronic order through a symmetry breaking transition. *Nature Physics*, 6(9):681–684, 2010.

[YYT+13] Shoji Yoshida, Munenori Yokota, Osamu Takeuchi, Haruhiro Oigawa, and Yutaka and Mera. Single-atomic-level probe of transient carrier dynamics by laser-combined scanning tunneling microscopy. *Applied Physics Express*, 6(3):032401, 2013.

[ZA14] J. Zhang and R.D. Averitt. Dynamics and control in complex transition metal oxides. *Annual Review of Materials Research*, 44(1):19–43, 2014.

[ZCZ+15] X. Zhu, Y. Cao, J. Zhang, E.W. Plummer, and J. Guo. Classification of charge density waves based on their nature. *Proceedings of the National Academy of Sciences*, 112(8):2367–2371, 2015.

[Zew00] A.H. Zewail. Femtochemistry: Atomic-scale dynamics of the chemical bond. *Journal of Physical Chemistry A*, 104(24):5660–5694, June 2000.

[ZP06] J.-G. Zhu and C. Park. Magnetic tunnel junctions. *Materials Today*, 9(11):36 – 45, 2006.

Publication list

J.A.J. Burgess, L. Malavolti, V. Lanzilotto, M. Mannini, S. Yan, S. Ninova, F. Totti, **S. Rolf-Pissarczyk,** A. Cornia, R. Sessoli, and S. Loth. Magnetic fingerprint of individual Fe4 molecular magnets under compression by a scanning tunnelling microscope. *Nature Communications*, 6:8216–, 2015.

S. Yan, D.-J. Choi, J.A.J. Burgess, **S. Rolf-Pissarczyk**, and S. Loth. Three-dimensional mapping of single-atom magnetic anisotropy. *Nano Letters*, 15(3):1938–1942, 2015.

S. Yan, D.-J. Choi, J.A.J. Burgess, **S. Rolf-Pissarczyk**, and S. Loth. Control of quantum magnets by atomic exchange bias. *Nature Nanotechnology*, 10(1):40–45, 2015.

T. Iffländer, **S. Rolf-Pissarczyk**, L. Winking, R. G. Ulbrich, A. Al-Zubi, S. Blügel, and M. Wenderoth. Local density of states at metal-semiconductor interfaces: An atomic scale study. *Physical Review Letters*, 114:146804, 2015.

S. Rolf-Pissarczyk, J.A.J. Burgess, S. Yan, and S. Loth. Closing the superconducting gap in small Pb nanoislands with high magnetic fields. *Physical Review B*, 94:224504, 2016.

T. Choi, W. Paul, **S. Rolf-Pissarczyk**, A.J. Macdonald, F.D. Natterer, K. Yang, P. Willke, C.P. Lutz, and A.J. Heinrich. Atomic-scale sensing of the magnetic dipolar field from single atoms. *Nature Nanotechnology*, 12(5):420–424, 2017.

D.-J. Choi, R. Robles, S. Yan, J.A.J. Burgess, **S. Rolf-Pissarczyk**, J.-P. Gauyacq, N. Lorente, M. Ternes, and S. Loth. Building complex Kondo impurities by manipulating entangled spin chains. *Nano Letters*, 17(10):6203–6209, 2017.

S. Rolf-Pissarczyk, S. Yan, L. Malavolti, J.A.J. Burgess, G. McMurtrie, and S. Loth. Dynamical negative differential resistance in antiferromagnetically coupled few-atom spin chains. *Physical Review Letters*, 2017. (to be published)

Eidesstattliche Versicherung/ Declaration on oath

Hiermit versichere ich an Eides statt, die vorliegende Dissertationsschrift selbst verfasst und keine anderen als die angegebenen Hilfsmittel und Quellen benutzt zu haben. Die eingereichte schriftliche Fassung entspricht der auf dem elektronischen Speichermedium. Die Dissertation wurde in der vorgelegten oder einer ähnlichen Form nicht schon einmal in einem früheren Promotionsverfahren angenommen oder als ungenügend beurteilt.

Hamburg, den 08.08.2018

_____

Unterschrift des Doktoranden